

# **Materials Processing & System Design for Infrared Photonic Devices**

Katherine Stoll

B.S. Materials Science & Engineering and Physics

Massachusetts Institute of Technology, 2019

# **Materials Processing & System Design for Infrared Photonic Devices**

Katherine Stoll

B.S. Materials Science & Engineering and Physics

Massachusetts Institute of Technology, 2019

## **Abstract**

Infrared photonic devices are rapidly growing technologies with a wide variety of applications ranging from sensing and imaging to optical signal processing, computing, and communication. While traditional silicon photonic integrated circuits (PICs) have paved the way for many different devices, there is significant potential for new materials development and characterization to improve and expand upon this technology. Additionally, many chalcogenide materials containing sulfur, selenium, and tellurium demonstrate unique properties, particularly in the mid-infrared regime, that could enable further applications for nonlinear optics, infrared detection, and chemical sensing. This thesis discusses the processing, properties, and performance of various chalcogenide materials as thin films and their integration for use in specific infrared photonic devices.

This work presents the design and optimization of several infrared photonic sensors based on the principles of optical absorption spectroscopy. First, a ratiometric infrared photonic sensor is demonstrated with a fully-integrated lead telluride (PbTe) detector and dedicated electronic read out circuit tuned to the properties of the integrated detector. This novel design effectively eliminated all common mode effects and input laser power fluctuations to achieve a low overall device limit of detection for several analytes in a compact device. Additionally, to pave the way for simultaneous detection of many analytes in unknown mixtures, the first mid-infrared on-chip digital Fourier Transform (dFT) spectrometer was designed for urine analysis over a 500 nm broadband spectral range.

In addition to integrated sensors and detectors, we have demonstrated the first free space PbTe p-n junctions fabricated via physical vapor deposition (PVD) with promising photovoltaic response. These devices can be used for mid-infrared photothermal photovoltaic applications such as waste heat harvesting or as passive integrated detectors with no external bias requirements for PICs.

Finally, for advanced waveguiding applications, we have demonstrated the first integration of ZnTe thin films with conventional silicon and silicon nitride waveguides through CMOS-compatible back-end-of-line (BEOL) atomic layer deposition (ALD). The nonlinear properties including both the second-order Pockels and third-order Kerr coefficients were evaluated for ZnTe across the infrared regime, and these hybrid waveguides achieve efficient nonlinear self-phase modulation with minimal two-photon absorption (TPA) losses compared to many conventional nonlinear materials. Finally, germanium (Ge) waveguides were fabricated and characterized for several material platforms and exhibit strong potential for low-loss, integrated mid-infrared sensors for a wide variety of chemical and biological applications.

Each of these developments demonstrates the potential widespread impact of PICs across many different disciplines through the processing and development of new thin film chalcogenide materials in conjunction with dedicated device designs.

## Table of Contents

Abstract .....	2
Table of Contents .....	4
List of Figures .....	5
List of Tables .....	5
1 Ratiometric MIR Chemical Sensing .....	6
1.1 Introduction to Optical Absorption Spectroscopy .....	6
1.2 Free Space Methane Gas Detection .....	8
1.3 Chalcogenide Glass Waveguide Design & Fabrication.....	10
1.4 Ratiometric Sensor Design & Fabrication .....	13
1.5 6-Channel CMOS-Based Electronic Readout for Optical Absorption Spectroscopy... <td>15</td>	15
1.5.1 Architecture of the Sensing System.....	15
1.5.2 6-Channel CMOS Front-End ASIC .....	16
1.5.3 Ratiometric Readout System.....	17
1.5.4 Electrical Characterization.....	19
1.5.5 Detection of Acetone Sample .....	20
2. Design of Broadband MIR Chemical Sensors .....	22
2.1 Introduction to Broadband Optical Spectroscopy.....	22
2.2 Broadband MIR On-Chip Digital Fourier Transform Spectrometer ( $\lambda_c \sim 2.25 \text{ } \mu\text{m}$ )....	24
2.2.2 Multimode Interferometer Design .....	26
2.2.3 Adiabatic Coupler Design.....	29
2.2.4 Thermo-Optic Phase Shifter Design .....	35
2.2.5 Edge Coupling Designs for Mid-Infrared LEDs.....	40
2.2.5.1 NIR Waveguide Loss Characterization .....	41
2.2.5.2 Mid-IR Waveguide Loss Characterization .....	42
2.2.5.3 Edge Coupler Design & Characterization.....	43
2.2.6 Packaging via Photonic Wire Bonding .....	45
2.2.6.1 Principles of Photonic Wire Bonding Technology .....	45
2.2.6.2 Experimental Results in Mid-Infrared Regime.....	47
2.2.6.3 Future Work .....	49
3. Mid-Infrared PbTe P-N Junction Diode .....	49
3.1 Motivation & Applications for MIR p-n Junction Diodes.....	49
3.2 Material Characterization & Device Design.....	52
3.2.1 PbTe Material Characterization .....	52
3.2.2 PbTe p-n Junction Device Design & Fabrication .....	55

3.3	PbTe p-n Junction Characterization.....	56
3.3.1	Dark I-V Characterization.....	57
3.3.2	PICTS Characterization .....	60
3.3.3	Responsivity Measurements .....	64
3.3.4	SEM & AFM Characterization .....	65
3.4	Improved Carrier Concentration Control with n-type Pb <sub>(1-x)</sub> Bi <sub>(x)</sub> Te .....	66
3.4.1	Hall Effect Characterization .....	67
3.4.2	XRD Characterization.....	68
4	Nonlinear Properties of ZnTe Thin Films for PICs .....	70
4.1	Introduction.....	70
4.2	ZnTe Material Characterization.....	71
4.4	ZnTe $\chi(3)$ Characterization .....	76
4.4.1	Hybrid ZnTe-on-Si Waveguide $\chi(3)$ Characterization .....	77
4.4.2	Hybrid ZnTe-on-SiN Waveguide $\chi(3)$ Characterization .....	81
4.6	Theoretical Device Design for ZnTe Electro-Optic Modulators .....	86
4.6.1	Operating Principles of Electro-Optic Modulators .....	86
4.6.1.1	Pockels Effect .....	87
4.6.1.2	Kerr Effect .....	88
4.6.1.3	Combined Pockels and Kerr Effects .....	88
4.6.2	Types of Electro-Optic Modulators and Device Designs .....	88
4.6.2.1	Phase Modulators.....	89
4.6.2.2	Dynamic Wave Retarders – Polarization Modulator .....	93
4.6.2.3	Intensity Modulators (Phase Modulator Inside Interferometer) .....	96
4.6.2.4	Intensity Modulators (Retarder Between Cross Polarizers).....	98
4.6.3	Nonlinear Materials Evaluation for Photonic Integrated Circuits .....	101
4.6.4	Conclusion .....	108
5	Ge Waveguides for MIR PICs .....	109
5.1	Introduction.....	110
5.2	Sample Design and Experimental Setup.....	111
5.3	Results and Discussion .....	113
5.4	Conclusion .....	118
	References .....	120

## **List of Figures**

## **List of Tables**

# 1 Ratiometric MIR Chemical Sensing

## 1.1 Introduction to Optical Absorption Spectroscopy

In today's data-driven society with increasing technological advancements and automation, there is a growing demand for sensors in a wide variety of applications ranging from the detection of harmful chemicals and gases to protect workers and the general public to patient health assessment and industrial process control. While many potential technologies exist for these applications, the widespread implementation and adoption of these sensors will require devices with small size, low power consumption, simple electronic integration, and low maintenance or calibration requirements. Integrated photonic sensors satisfy each of these demands and are consequently well-suited solutions for many sensing applications.

Integrated photonic sensors consist of a light source, sensing element, and detector and rely on the interaction of light with target chemicals or biological analytes [1]. These sensing elements detect the presence of different substances through the use of refractometry or optical absorption spectroscopy. Refractometry measures a shift in optical resonance or a change in polarization to detect a change in the refractive index of the sensing waveguide, while optical absorption spectroscopy (OAS) measures the absorption of different wavelengths that correspond to the unique chemical fingerprint of the analyte [2]-[3]. Since the fundamental vibrational modes of many common bonds and molecules (O-H, C-H, N-O, etc.) exist within the infrared regime, this is an important spectral range for optical absorption spectroscopy that enables the detection of chemicals with very high specificity and selectivity [4]. Integrated infrared photonic sensors utilize waveguides with a large evanescent field to maximize the interaction between the propagating light signal and the analytes present in the surrounding environment. If the signal wavelength matches one of the absorption peaks of the species of interest, the light is absorbed with an attenuation that depends on the analyte concentration. By monitoring the optical power at the output with a photodetector, the presence of a target chemical can thus be detected in real-time. As such, optimizing the design of integrated infrared photonic devices with sensitized detectors will provide essential capabilities for chemical detection in a wide range of industries.

This work describes the design of integrated photonic sensors for methane gas detection, which can be used to monitor emissions for better industrial system and safety regulation control. To

improve the overall performance and limit of detection of these methane sensors, this thesis focuses on optimizing the waveguide material and fabrication process to reduce optical losses, optimizing the device design to reduce external noise contributions, and incorporating a high-performance photodetector with hybrid integration of electronics [5].

Previous work by Su et al. has demonstrated a monolithic on-chip mid-infrared methane gas sensor with waveguide-integrated detector [28]. This device utilized a silicon platform with spiral chalcogenide waveguide sensors and waveguide-integrated PbTe thin film detectors to achieve reduced noise that results from the decreased size and increased speed benefits of integrated detection [28]. The sensor design is shown below in Figure 1 and consists of a Ge<sub>23</sub>Sb<sub>7</sub>S<sub>70</sub> (GeSbS) chalcogenide glass spiral waveguide sensing element with a cross section of 2 μm wide by 1 μm tall that is optimized for single mode propagation at the 3.31 μm wavelength absorption peak of methane.

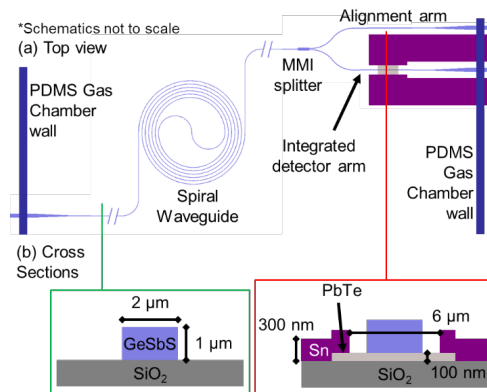


Figure 1. Schematic of the a) top view and b) cross-sectional views of the sensor with a sensing spiral chalcogenide waveguide and an integrated PbTe detector [28].

This initial design successfully demonstrated a fully integrated sensing element and on-chip detector for mid-infrared gas sensing at room temperature. While these results are very promising, further research to reduce optical losses and eliminate the remaining noise sources from the detector and light source with a new ratiometric device design will improve sensitivity and lower detection limits.

## 1.2 Free Space Methane Gas Detection

To accurately design and fabricate an optimized methane gas sensor with a low limit of detection (LOD), a free space measurement system was first designed to experimentally determine the peak absorption wavelength and absorption coefficient of the methane gas analyte. The free space system comprised of a 15 mm long anodized aluminum collimating tube sealed with a planar ZnSe filter at the input and a ZnSe aspheric lens (Edmund Optics 39-469) at the output to focus the optical signal through a CaF<sub>2</sub> lens and onto the detector as shown in Figure 2. An input and output tube were fixed to the top and bottom of the collimating tube to enable the flow of methane and nitrogen gas mixtures with precise concentrations regulated through the use of mass flow controllers. The measurements were performed using a tunable mid-infrared laser source (Firefly M Squared, wavelength tunable from 2.3 – 3.8 um with 5 nm linewidth) modulated with a mechanical chopper at 3.12 kHz. The optical signal was aligned through the gas flow chamber using a mid-IR camera with a cryogenically-cooled InSb focal plane array and then focused onto the free-space detector and isolated with an adjustable iris to reduce any noise contributions from the surrounding environment. The voltage across the free-space detector was passed to a lock-in amplifier (SR810, Stanford Research Systems) synchronized with the modulation frequency of the chopper and a time constant fixed at 100 milliseconds, corresponding to an effective noise bandwidth of 0.78 Hz.

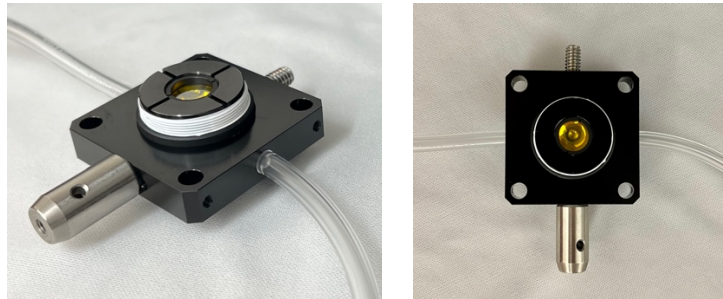


Figure 2. Free-space gas measurement system with a sealed gas flow chamber between two ZnSe lenses and compressive-fit connective tubing to enable precise gas flow control of varying concentrations in and out of the device.

To evaluate the methane absorption peak, the detector signal was monitored under a flow of pure nitrogen for 2 minutes as a baseline reference followed by 2-minute measurements under pure

methane flow at different wavelengths between 3300 to 3350 nm. The transmission ( $T$ ) at each wavelength was calculated by normalizing the signal under pure methane gas ( $V_{\text{CH}_4}$ ) to the signal under pure nitrogen ( $V_{\text{N}_2}$ ) as given by Equation 1. The experimental results are shown in Figure 3a and demonstrate a peak absorption wavelength of 3330nm where the transmission is approximately 27%.

$$T = \frac{V_{\text{CH}_4}}{V_{\text{N}_2}} = \exp(-\alpha \Gamma L C) \quad (1)$$

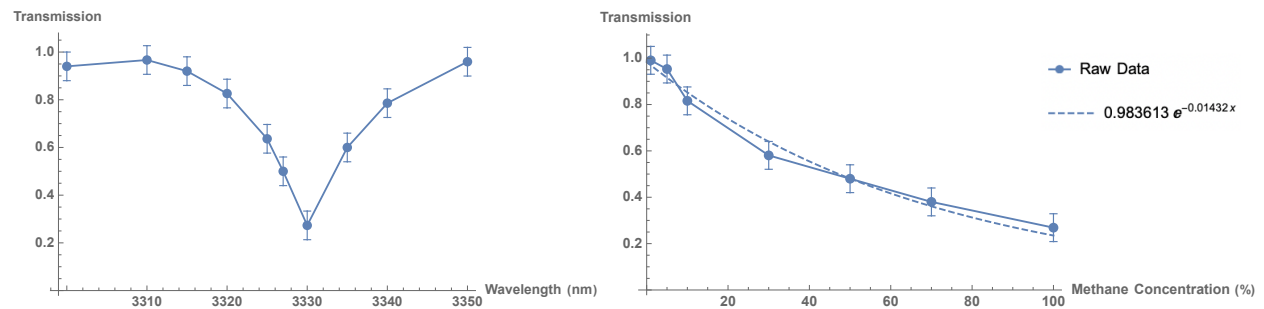


Figure 3. Experimental results for a) optical transmission under 100% methane gas flow as a function of wavelength demonstrating a strong absorption peak at 3300 nm. b) Optical transmission at 3330 nm wavelength as a function of methane gas concentration follows the Beer-Lambert Law with an exponential decay in transmission with increasing methane concentration.

After isolating the absorption peak wavelength, the optical transmission at 3330 nm was evaluated as a function of methane gas concentration from 100 down to 1 vol%, to determine the absorption coefficient ( $\alpha$ ) of the analyte. The experimental optical transmission closely followed an exponentially decaying behavior as a function of methane concentration as indicated by the Beer-Lambert Law given in Equation 1, where  $\Gamma$  is the confinement factor of the gas interacting with the analyte,  $L$  is the optical path interaction length, and  $C$  is the volumetric methane concentration. Assuming a confinement factor of  $\Gamma = 1$  and an optical path length of  $L = 6$  mm for these free space measurements, the absorption coefficient extracted from the exponential fit as shown in Figure 3b was determined to be  $\alpha_{\text{CH}_4} = 2.11 \text{ cm}^{-1}$ .

While this free space system was able to accurately detect down to 1% methane gas, an integrated system with a ratiometric readout strategy would help to reduce the noise contributions from the laser source and external environmental factors and consequently reduce the overall limit of detection (LOD).

### 1.3 Chalcogenide Glass Waveguide Design & Fabrication

Previous work by Su et al. demonstrated a monolithic on-chip mid-infrared methane gas sensor with waveguide-integrated PbTe detector [3]. This device utilized a silicon wafer platform with Ge<sub>23</sub>Sb<sub>7</sub>S<sub>70</sub> (GSS) chalcogenide glass spiral waveguides for the sensing element as this material is transparent across the MIR spectral range from approximately 1 to 20  $\mu\text{m}$  wavelength. These GSS waveguides were optimized for single mode propagation at the 3.33  $\mu\text{m}$  wavelength absorption peak of methane with the fundamental TE mode profile shown in Figure 4b for a waveguide cross section of 2  $\mu\text{m}$  wide by 1  $\mu\text{m}$  thick on a Si wafer with 3  $\mu\text{m}$  thermal oxide.

A double-layer liftoff technique was employed to successfully pattern these GSS waveguides as previous work has demonstrated lower sidewall roughness for chalcogenide glass waveguides fabricated via liftoff compared to etching [10]. The lift-off procedure began with spin-coating an approximately 1.8  $\mu\text{m}$  thick layer of PMGI-SF9 resist followed by a thinner 400 nm layer of electron-beam sensitive ZEP resist. The waveguides were then patterned using electron-beam-lithography (Elionix FS-125) and a precise development of first the ZEP resist layer in ZED developer and second the PMGI layer in AZ 726 MIF developer. This development sequence is critical to achieve a large undercut of the PMGI layer as shown in Figure 4a that will ensure successful mask transfer and high yield processing of the GSS waveguides with the desired dimensions. The 1  $\mu\text{m}$  thick GSS film was then deposited across the substrate using a physical vapor deposition (PVD) technique and finally patterned in NMP to liftoff the excess photoresist and obtain the desired waveguide pattern. SEM imaging of the fabricated GSS waveguide cross-sections confirms accurate thickness and widths with a sidewall angle of approximately 40 degrees from the vertical as shown in Figure 4c-d.

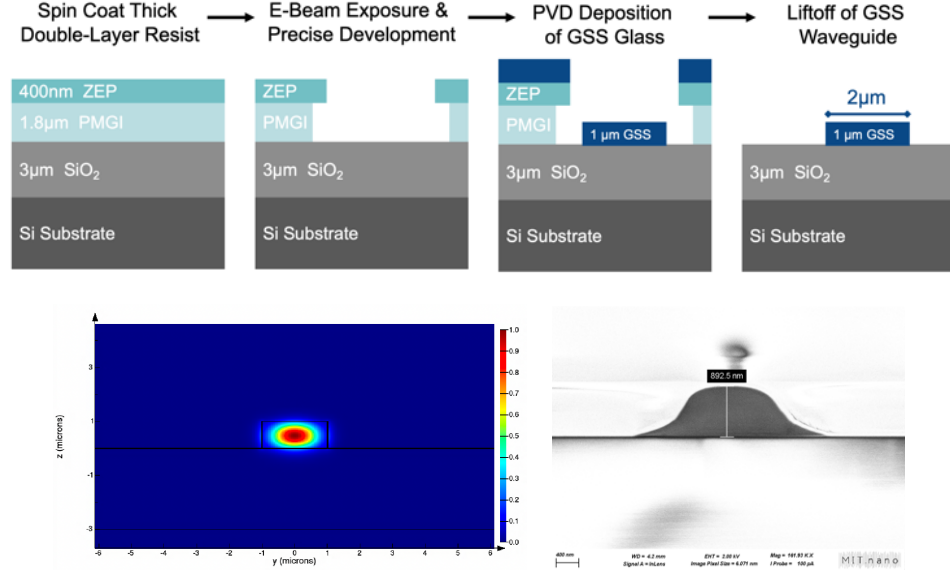


Figure 4. a) Step-by-step double-layer e-beam lithography liftoff process developed for precise fabrication of GSS waveguides on SiO<sub>2</sub> substrate. b) Simulated fundamental TE mode profile of the 1 um thick by 2 um wide GSS waveguide and c) corresponding SEM imaging of the fabricated waveguide cross section with accurate dimensions and a sidewall angle of 40 degrees.

Upon successful fabrication of these GSS waveguides, the propagation loss was evaluated to ensure high performance and low optical losses that would be necessary to achieve a high-performance integrated sensing device. The waveguide propagation loss was measured using the cutback method with four waveguide spirals of varying length fabricated on the same substrate. The overall power loss was then plotted as a function of the increasing relative waveguide length compared to that of the shortest spiral as shown in Figure 5a. The waveguide transmission loss was then extracted from the best fit line as indicated by the red dashed line in Figure 5a to determine a propagation loss of  $2.73 \pm 0.6$  dB/cm for these initial measurements at 2.361  $\mu$ m wavelength. These measurements were then repeated at several wavelengths across the MIR regime up to 3.3  $\mu$ m and demonstrate a consistent propagation loss of roughly 2.5 dB/cm within this wavelength range.

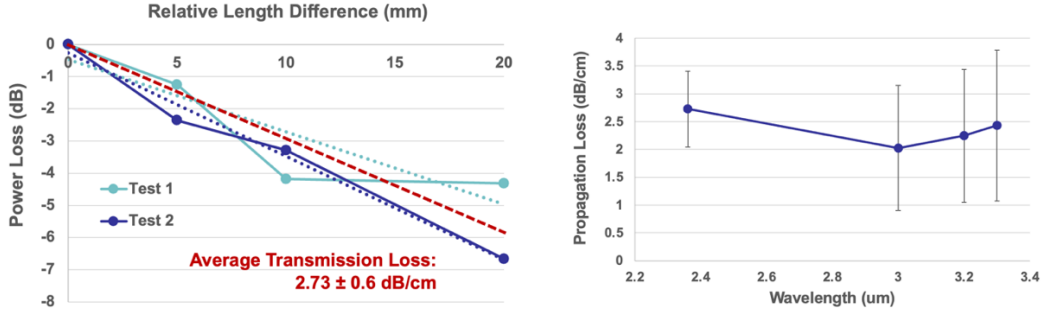


Figure 5. a) Optical power loss at 2.361  $\mu\text{m}$  wavelength as a function of relative waveguide length. The slope of the dashed, red best-fit line indicates the average transmission loss of 2.73 dB/cm. b) Propagation loss for GSS waveguides across the MIR regime demonstrates low optical losses between than 2.0 to 2.7 dB/cm.

While this propagation loss of 2.5 dB/cm improves upon previous demonstrations of chalcogenide glass waveguides in the MIR regime [11], other works have achieved propagation losses as low as 0.5 dB/cm in the NIR at 1550nm [12-14] for waveguides with comparable sidewall roughness. The higher propagation losses in the MIR regime could be attributed to increased substrate leakage to the underlying Si wafer. As such, these propagation loss measurements were repeated for GSS waveguides fabricated on a Si substrate with a thicker 5  $\mu\text{m}$  thermal oxide layer compared to the previously measured waveguides on 3  $\mu\text{m}$  BOX. Lumerical MODE simulations indicate that this increase in oxide thickness would reduce the electric field leakage to the Si substrate by nearly four orders of magnitude across the MIR regime and consequently reduce the propagation losses to approach the experimentally demonstrated 0.5 dB/cm loss in the NIR.

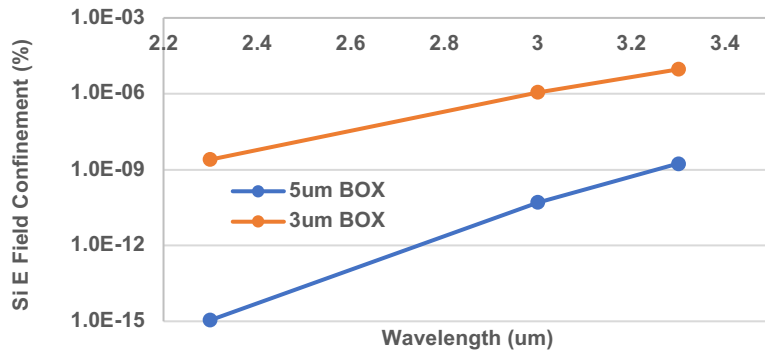


Figure 6. Simulated electric field confinement in the Si substrate as a function of wavelength for a 1  $\mu\text{m}$  thick  $\times$  2  $\mu\text{m}$  GSS waveguide with varying BOX thickness of 3 and 5  $\mu\text{m}$ . As the BOX

thickness increases, the Si substrate leakage is reduced by two orders of magnitude to minimize optical propagation losses.

#### 1.4 Ratiometric Sensor Design & Fabrication

After optimizing the waveguide fabrication process and experimentally demonstrating low optical losses, a photonic integrated circuit was designed for methane gas detection. Based on previous works that suffered from reduced sensitivity due to considerable noise contributions for laser power fluctuations and other external environmental variables, this work utilized a ratiometric sensing design that simultaneously measures the direct laser signal along with the sensor signal after exposure to the methane gas analyte. By computing the ratio of the reference and sensing detector signals, all the common mode effects can be rejected. The optimized sensor design is shown in Figure 7a where the incoming laser signal is edge-coupled into the GSS waveguides through a wide taper. The signal is then guided through a multimode interferometer (MMI) and equally split between a reference and sensing arm. The top reference arm is directly routed to a waveguide-integrated reference detector to monitor the laser power fluctuations and coupling instability. The remaining signal is directed through a sensing spiral with a long optical path length in the sensing chamber that contains the methane gas analyte before reaching the sensing detector.

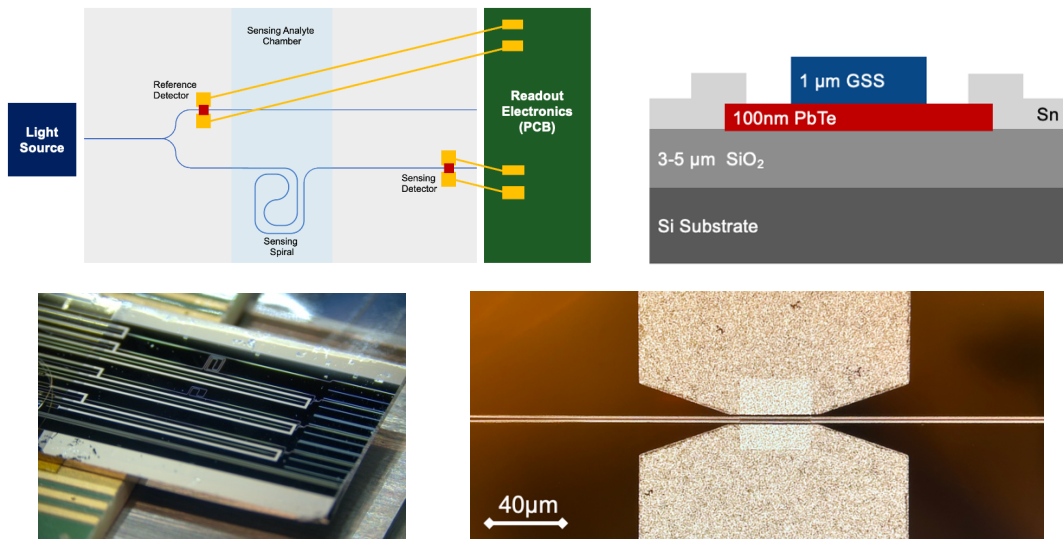


Figure 7. a) Top-view of an optimized ratiometric sending device with an off-chip light source edge-coupled to the GSS waveguides through a regular taper and then split through an MMI to a reference and sensing detector after propagating through the sensing spiral exposed to the analyte

of interest in the gas chamber. b) Cross-sectional view of the 100 nm thick PbTe detector underneath the GSS waveguide for efficient absorption and photocarrier generation. Optical microscope image of a c) fabricated ratiometric sensing chip with three waveguide channels and d) a top view of the GSS waveguide crossing over the square PbTe detector connected to the Sn contacts for electronic readout.

In addition to the improve sensitivity for the ratiometric design, these devices also benefit from reduced noise of the waveguide-integrated detectors due to their small size and increased speed [15-17]. PbTe was chosen as the integrated detector material as it has previously demonstrated high performance as a mid-IR detector that can be monolithically integrated with the GSS waveguides as shown in Figure 7b through thermal evaporation techniques.

These devices were fabricated by first depositing a 100 nm thick PbTe film for the detector components onto a silicon substrate with a thermally grown oxide (either 3 or 5 um thick) using a PVD technique. The PbTe was then patterned using photolithography and lift-off in an NMP solvent into 40 by 40 um square detectors that were designed to fully absorb the incoming optical signal from the GSS waveguides. The 300nm thick ohmic Sn contacts were then deposited through thermal evaporation and patterned on either side on the PbTe detectors with 6 um separation to ensure efficient collection of the photogenerated carriers. Ti-Au bond pads were then deposited at the ends of the Sn contacts through E-Beam evaporation to enable wire bonding from the photonic integrated circuit to an external printed circuit board (PCB) for electronic readout. Finally, the 1 um thick GSS waveguides were patterned using the double-layer liftoff method described in Section 1.3 and cleaved to create the input taper facets, resulting in a 1 by 1 cm fully-integrated sensor. Figure 7d illustrates a top view of one of the fabricated detectors with the incoming waveguide from the left side crossing over the PbTe detector that is connected to the trapezoidal Sn contacts designed to reduce any optical reflections of the incoming signal. The methane gas microfluidic chamber was fabricated by casting a polydimethylsiloxane (PDMS) elastomer into a mold with the desired dimensions and then plasma bonding to the photonic chip for testing. Since PDMS has a non-negligible extinction coefficient in the mid-infrared regime, the GSS waveguides were adiabatically tapered from 2 to 15 um wide when propagating under the chamber wall to minimize the evanescent field and reduce any optical absorption losses.

## 1.5 6-Channel CMOS-Based Electronic Readout for Optical Absorption Spectroscopy

(This section has been modified from published work in [18] to fit within this thesis)

Having successfully designed and fabricated an integrated infrared methane gas sensor, a multichannel portable instrument was designed for electronic readout. The compact size of the integrated photonic sensing systems allows integration of several waveguides on the same chip, to simultaneously detect multiple chemicals or monitor several absorption lines of a single analyte. This possibility translates into the need for a dedicated electronic readout instrument, capable of acquiring and processing multiple measurements. Similar systems exist for the visible and near-infrared spectral range [4], [5], but they lack for longer wavelengths. In this section, a novel multichannel electronic system is presented that is specifically designed for mid- infrared on-chip OAS measurements. A 6-channel CMOS lock-in front-end performs the amplification and demodulation of the signals from the integrated light detectors in parallel, while an FPGA is chosen for signal acquisition and analysis. A digital real-time ratiometric processing cancels out the effect of laser power fluctuations to achieve high sensitivity in monitoring the presence of the analytes, as demonstrated with the detection of an acetone sample. Compact size for portability, real-time parallel detection and flexible FPGA processing make this system suitable for environmental investigations on many different pollutants, both in the near- and mid-infrared wavelength range.

### 1.5.1 Architecture of the Sensing System

Figure 8 shows the scheme of the photonic chip fabricated to perform OAS. To increase the sensitivity of the device, the GSS waveguide was designed with a spiral shape, obtaining a long interaction length of 5 mm in a small chip area. In addition, the ratiometric structure was created to make the measurement insensitive to fluctuations of the optical power coupled to the chip that cause variations of the output signal indistinguishable from those related to the analytes. Three sensing structures were integrated on the same die for multichannel detection.

The integrated PbTe photodetectors demonstrated an ohmic behavior with resistance around 15 k $\Omega$ . The small bandgap of the PbTe material ( $E_g \sim 0.2$  eV) make it well suited to detect radiations up to 4.3  $\mu\text{m}$  [6]. Previous characterizations of the sensors demonstrated their good sensitivity in the mid-infrared range but also highlighted the presence of a bias-dependent 1/f noise [7]. The lock-in technique has thus been chosen as readout scheme in order not to degrade the system

performance, taking advantage of the shift in signal frequency that it requires. A pulsed laser with 150 kHz repetition rate was employed to directly generate a modulated signal at the chip input, without an external chopper.

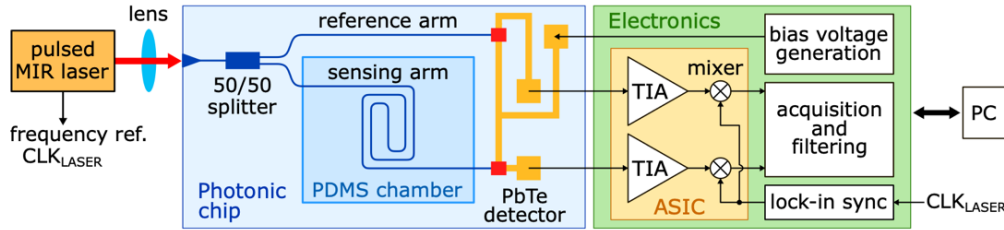


Figure 8. Schematic view of the on-chip optical absorption spectroscopy sensing system: a laser is coupled to the photonic chip and the resulting signals at the chip output are measured with integrated PbTe photodetectors and acquired with a custom electronic instrument.

The photonic chip is mounted on a compact PCB holder, shaped to facilitate the coupling of light and the wire-bonding of the integrated detectors. The holder is connected to a custom electronic readout system. The preamplification and lock-in demodulation are performed with a CMOS ASIC, pivotal in enabling multichannel operations in a very compact form factor. The other electronic functionalities are instead managed by discrete-component electronics mounted on a motherboard. An FPGA, on a commercial module, handles the digital signal processing and the communication with a personal computer.

### 1.5.2 6-Channel CMOS Front-End ASIC

Figure 9 shows the schematic of the front-end ASIC, fabricated in TSMC 180 nm CMOS technology. A current-sensing architecture based on a transimpedance amplifier (TIA) has been chosen to simultaneously bias the PbTe detectors and read their signal. The light-induced current variations are in the order of few nA, modulated at 150 kHz and superimposed to a large DC bias of around 100  $\mu$ A. In order not to limit the amplifier gain, an enhanced TIA has been designed [8]. An auxiliary DC handling loop has been added to steer the bias current away from the gain stage, allowing to correctly amplify the signal of interest without saturating the circuit.

The TIA has been designed with digitally selectable feed-back resistor and capacitor (15 k $\Omega$ , 45 k $\Omega$ , 135 k $\Omega$ , 405 k $\Omega$  and 2.7 pF, 900 fF, 300 fF, 100 fF respectively), always ensuring a bandwidth

of at least 4 MHz. A second amplifier, with a gain of 20, has been included at the TIA output to achieve a maximum overall amplification of 8 MΩ. The DC handling network has been made with a cascade of two integrators, that filter out the high-frequency oscillations of the TIA output and amplify its DC component, and a resistor RDC that generates the reaction current to compensate the detector bias. The value of RDC can be digitally selected (5 kΩ, 15 kΩ, 45 kΩ, 135 kΩ) to adapt to different bias conditions of the PbTe detectors, while the capacitor CZ stabilizes the loop. Since the signal of interest is modulated at 150 kHz, the DC handling network has been designed with a maximum closed-loop bandwidth of around 1kHz. The very large equivalent resistors needed to satisfy this requirement were obtained with two physical components of 1MΩ and a cascade of two active current reducers, each with a reduction factor of around 100 [9].

Each TIA is followed by two on-chip demodulators, based on a square-wave double-balanced passive architecture, to perform the lock-in processing and extract the in-phase and quadrature components of the sensor impedance. An analog demodulation is here preferred to simplify the design of the acquisition chains of the motherboard, while not degrading the detection accuracy. The noise of the PbTe detectors (30 pA/  $\sqrt{\text{Hz}}$  at 150 kHz) is in fact the dominant term.

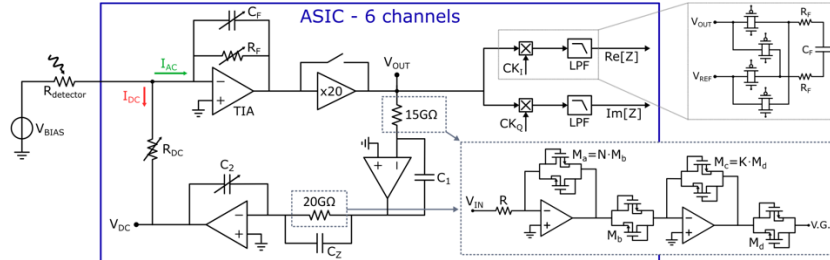


Figure 9. Schematic of the proposed CMOS lock-in front-end. An active network removes the DC current from the virtual ground of the transimpedance amplifier, allowing larger amplification of the useful modulated signal. A square-wave mixer performs the lock-in demodulation at the chip output.

### 1.5.3 Ratiometric Readout System

The ASIC is mounted on a printed circuit motherboard designed to: i) further amplify, filter and digitize the ASIC output; ii) provide the voltage bias to the PbTe detectors; iii) generate the

demodulation signals required for the lock- in processing; iv) communicate with a personal computer for visualization and storage of the measurement results. Fig. 3 shows the architecture of the board.

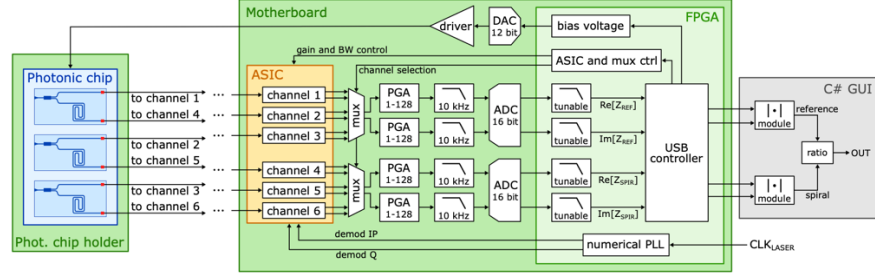


Figure 10. Schematic view of the complete electronic system, showing the motherboard, the digital signal processing in the FPGA and the ratio operation.

The outputs of the 6 ASIC channels are connected to two analog multiplexers, to select and read just one of the 3 sensors on the photonic chip at a time. Since the signals to be measured have a slow evolution with timescale of few seconds, the readout of the 3 structures can be time-multiplexed without penalties. Four acquisition chains are needed to acquire the real and imaginary parts of the spiral and reference detectors. The acquisition chains comprise a low-1/f noise programmable gain amplifier (PGA281, Texas Instruments), a third-order passive antialias filter with 10 kHz cut-off frequency and a 16- bit ADC (AD7903, Analog Devices), operated at 62.5kSps. The digitized signals are further low-pass filtered in the FPGA to define the lock-in readout bandwidth and then sent to a PC through a USB controller. A custom C# GUI computes the absolute value of the reference and spiral detectors impedance and then performs the ratio between the measurements. These operations were not performed in the FPGA because of the higher arithmetic precision of a 64-bit computer. The GUI also visualizes and stores the measurement results.

The voltage bias for the PbTe detectors is defined in the FPGA and then generated with a 12-bit DAC (AD5687R, Analog Devices) and buffered (AD8513, Analog Devices). The buffer allows to generate voltages between  $\pm 5$  V, enough to bias the detectors in different operating conditions if needed.

The motherboard also generates the demodulation signals for the lock-in processing in the ASIC. The laser clock is acquired by the FPGA and fed to a fully-digital phase-locked loop (PLL). The PLL is based on a 12-bit time-to-digital converter and a numerical oscillator implemented by extracting the most significant bit of a free-running counter. By changing the counter increment, the oscillation frequency can be arbitrarily tuned. The use of a 200 MHz clock and a counter width of 32 bits translates into a frequency resolution of 0.05 Hz. The PLL is used to generate a square wave at twice the laser clock frequency and its inverted version. By halving the frequency of these signals, the two in-phase and quadrature clocks needed for the lock-in demodulation are created.

#### 1.5.4 Electrical Characterization

Figure 11 shows the realized prototype, highlighting its size and building blocks. The system has an overall current consumption of 400 mA (200 mA for the FPGA, 150 mA for the PCB and 50 mA for the ASIC) with a supply of  $\pm 6.5$  V.

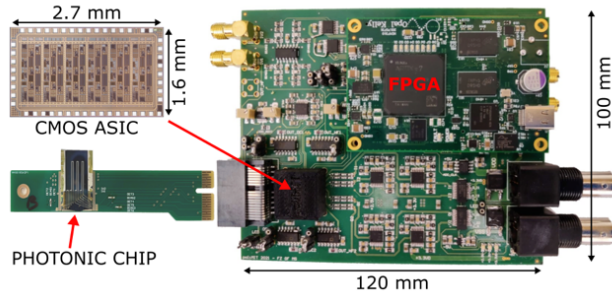


Figure 11. Photograph of the complete instrument, composed of the photonic chip holder plugged into the main motherboard that contains the CMOS ASIC, the readout electronics and the FPGA.

The transfer function of the TIA has been measured by applying a voltage signal to a  $15\text{ k}\Omega$  resistor, connected to the virtual ground to simulate the presence of a PbTe detector. A DC current of  $100\mu\text{A}$  has been injected into the chip by biasing the resistor at 1.5 V. The RDC of the TIA has been set to  $5\text{ k}\Omega$  to achieve the highest possible DC loop bandwidth and verify that, even in these conditions, the TIA can still process the signal of interest correctly. Figure 12 shows the measurement result. The TIA gain has been varied between the maximum and minimum values, while adapting the value of CF and C2 accordingly. In all conditions, the circuit correctly amplifies

the signals between 1 kHz and 1 MHz, perfectly satisfying the requirement of the application. As expected, the DC current is always rejected, certifying the correct operation of the chip.

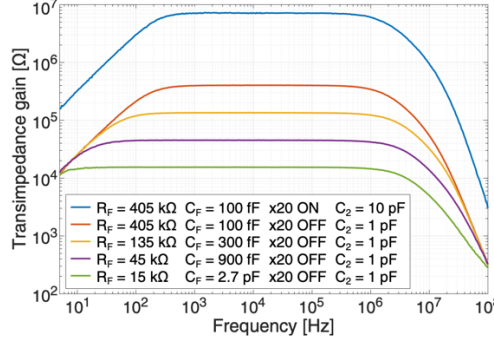


Figure 12. Transfer function of the integrated TIA, measured for different gain settings. The DC current is correctly rejected, while large amplification is maintained on a frequency range between 1 kHz and 1 MHz.

The digital PLL has also been tested, by connecting the laser reference signal at 150kHz to the FPGA to generate the demodulation signals. Figure 13 shows the obtained results. As expected, the PLL output square wave at twice the laser repetition rate is perfectly synchronized to the input clock. The demodulation square waves, aligned with the rising and falling edge of the PLL output, are in a precise phase quadrature relation and they can thus be used for the lock-in processing.

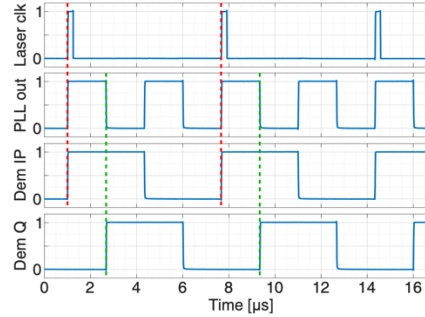


Figure 13. Measured normalized lock-in demodulation signals, correctly generated by the numerical PLL starting from the laser clock reference.

### 1.5.5 Detection of Acetone Sample

The electronic system has been validated in a real ratiometric spectroscopic measurement. Acetone has been chosen as the target analyte, because droplets of this chemical can be easily released on

the sensing spiral. The laser wavelength has been set to  $3.3\text{ }\mu\text{m}$ , where acetone has an absorption peak. The input power coupled to the chip was about  $1\text{mW}$ . The electronic platform has been used to simultaneously monitor the signals of the sensing and of the reference detectors on the photonic chip, with a lock-in bandwidth of  $1\text{ Hz}$ .

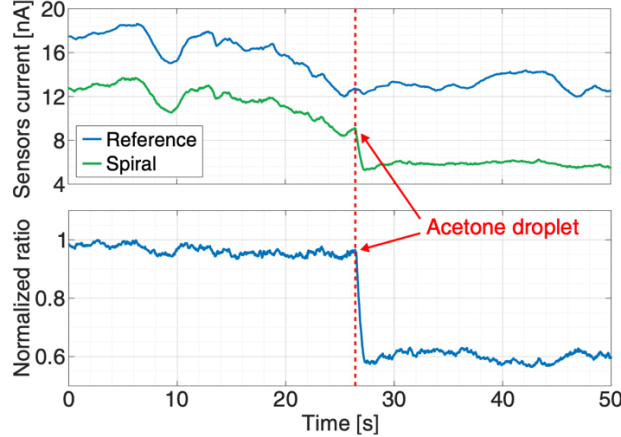


Figure 14. Detection of an acetone sample, performed at  $3.3\text{ }\mu\text{m}$  wavelength: after  $26\text{ s}$  a droplet is released on the sensor and correctly detected. The ratiometric measurement successfully cancels out the effect of input power fluctuations.

Figure 14 shows the magnitude of the modulated detectors currents during the experiment. Before the arrival of the acetone sample, the laser alignment has been voluntarily disturbed to cause small variations of the optical power coupled to the chip. These variations are correctly measured by both arms of the photonic chip, as highlighted by the similar evolution of the reference and spiral currents. The computation of the ratio between the two signals, shown in the figure, is therefore effective in canceling out these oscillations, demonstrating the validity of the ratiometric approach. After  $26$  seconds, an acetone droplet has been released on the spiral arm. The presence of the analyte attenuates the light reaching the corresponding photodetector, while the reference signal correctly stays constant. The computation of the ratio thus clearly reveals the moment of the acetone release.

The measurement certifies the correct design and operation of the whole detection system. The electronics, being independent of laser wavelength, optical chip technology and detector material,

can also adapt to other environmental monitoring applications, not necessarily limited to the near-infrared region.

## 2. Design of Broadband MIR Chemical Sensors

### 2.1 Introduction to Broadband Optical Spectroscopy

While the previous chapter demonstrated the use of OAS for chemical detection of a single analyte at a specific target wavelength of 3.33 um, there are many systems which require broadband optical spectroscopy to distinguish several signals at different frequencies. Broadband optical spectroscopy is an important analysis technique for several different applications ranging from optical network performance monitoring, hyperspectral imaging, radio-frequency spectrum analysis, and spectroscopic sensing of mixed analytes. However, conventional spectrometers are very large and bulky with many mechanical moving parts which increases the cost of this equipment and limits the versatility and implementation of these devices. On-chip spectrometers offer several size, weight, cost, and power advantages compared to these conventional benchtop instruments which could facilitate more widespread integration of these devices for many diverse applications.

Despite these promising advantages, previous on-chip spectrometers have demonstrated lower performance and less scalability than benchtop spectrometers. This is primarily due to the fact that most on-chip spectrometers rely on dispersive elements such as gratings [19], holograms [20], or microresonators [21] that distribute the input light signal over several spectral channels which results in a low signal-to-noise ratio (SNR) when designed for high spectral resolution [22]. Additionally, these devices demonstrate poor scalability as the device footprint, the number of individual photodetectors, and the overall complexity increase linearly with the number of spectral channels (N).

One alternative to these dispersive spectrometers is a Fourier transform infrared (FTIR) spectrometer that overcomes the trade-off between SNR and spectral resolution by using an interferometer with a tunable optical path length (OPL). While benchtop FTIR spectrometers employ moving mirrors to modify the OPL, on-chip FTIR devices use thermo-optic or electro-optic modulators to create a tunable waveguide OPL. However, these modulators only achieve

small changes in the refractive index that consequently require large device footprints and are still limited to a spectral resolution of several  $\text{cm}^{-1}$  that is only suitable for the reconstruction of sparse spectra. More recent work has demonstrated an on-chip digital Fourier transform (dFT) spectrometer that demonstrates high spectral resolution via time-domain reconfiguration of a reconfigurable Mach-Zehnder interferometer (MZI) with two orders of magnitude larger OPL variation per unit waveguide length compared to thermo-optic or electro-optic modulation as shown in Figure 15 [22].

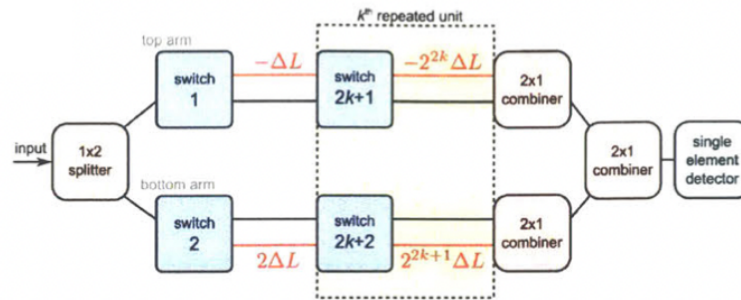


Figure 15. Schematic of the dFT spectrometer design with a cascade of optical switches in each arm of the reconfigurable MZI device [22].

Within this novel dFT spectrometer, each arm of the MZI contains a cascade of  $j/2$  optical switches that direct light to waveguides of different path lengths. The number of spectral channels ( $N = 2^j$ ) and the spectral resolution ( $\delta\lambda \approx \frac{1}{2^j} \frac{\lambda^2}{n_g \Delta L}$  given by the Rayleigh criterion) scale exponentially with the number of optical switches and consequently demonstrate superior performance capabilities compared to other on-chip spectrometers. Additionally, this dFT spectrometer only requires a single element photodetector rather than a linear array which also significantly reduces the system complexity and cost.

The first demonstration of an on-chip dFT spectrometer was design for operation at the C-band with a 20nm bandwidth between 1550nm to 1570nm. However, since most chemicals have strong absorption peaks in the mid-infrared spectral range, it would be beneficial to re-design this dFT spectrometer system for longer wavelengths in order to enable integration with optical sensing devices.

## 2.2 Broadband MIR On-Chip Digital Fourier Transform Spectrometer ( $\lambda_c \sim 2.25 \text{ }\mu\text{m}$ )

One of the most exciting applications for on-chip spectrometers is for biological specimen analysis as this technology can provide fast, high quality, quantitative results with the use of small samples and minimal equipment deployable in any environment. In particular, urine testing is commonly used for routine health monitoring as there are many important components in urine samples that are indicative of a variety of serious health conditions. For example, proteins in urine usually suggest kidney disease or kidney damage, glucose in urine is a sign of diabetes or high blood sugar, and the creatinine levels in urine can provide information about liver disease and muscle disease. While urinalysis is essential for many different routine tests, it typically requires complex clinical lab analysis to obtain detailed quantitative information and results. This lab analysis uses sophisticated equipment operated by lab experts and generally takes several days to complete, making it impractical for some applications. Alternatively, urine strips can be used for fast, portable analysis, but these test strips only provide rough analytic estimations and are not able to identify the actual substances within the sample or provide their accurate concentrations.

On-chip infrared spectroscopy offers an alternative urine test method that eliminates the need for bulky laboratory equipment while still providing quantitative results at a faster rate. Since the chemical and biological agents of interest, including proteins, creatinine, glucose, and urea, have signature absorption peaks in the infrared spectral regime, monitoring these strong absorptions can enable quantitative analysis of the concentration levels of each substance in the urine test samples. Figure 16 shows the differential spectra of urine samples in comparison with the reference analytes (figure from [23]), which demonstrates that strong absorption peaks can be found in urine samples in the spectral region from 2.0 to 2.5  $\mu\text{m}$ . These signature absorptions can thus be used to identify the chemicals in the urine samples. In addition to delivering fast, accurate, and sensitive measurements, on-chip infrared spectroscopy also benefits from the use of comparatively small sample sizes with no preparation and simultaneous measurement of several analyte levels. As such, the following chapter identifies and optimizes the key device components necessary to create a broadband, on-chip dFT spectrometer that covers the 2.0  $\mu\text{m}$  to 2.5  $\mu\text{m}$  spectral range with a high SNR and spectral resolution to realize a high-performance PIC urine test system.

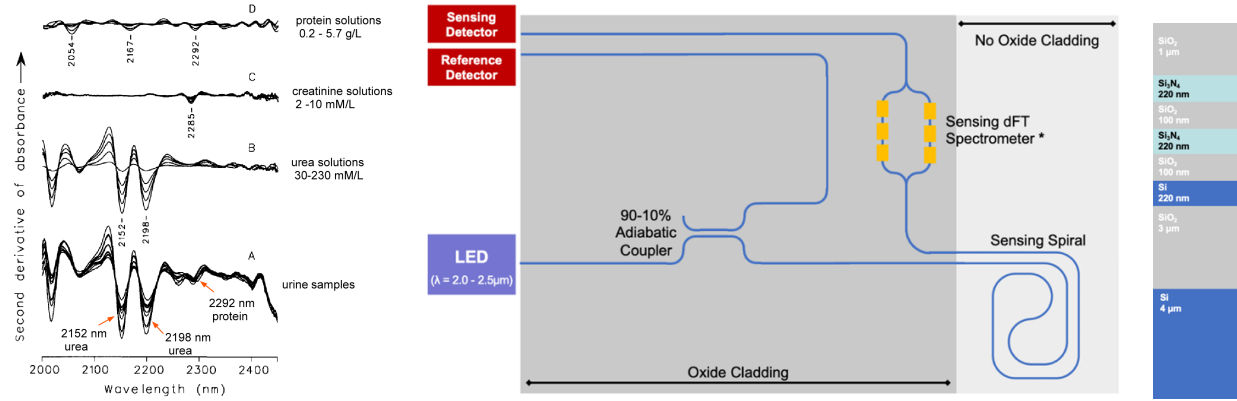


Figure 16. Differential spectra of a) urine samples in comparison with the reference analytes of b) urea solutions, c) creatinine solutions, and d) protein solutions [23]. Chemicals in the urine samples can be identified from the signature absorptions. e) The urine sensing system combines several components that have been labeled above as LED, edge coupler, adiabatic coupler, sensing spiral, dFT spectrometer, and detectors. f) The cross-sectional schematic indicates the thickness of each material layer within the device.

The proposed miniature urine test system consists of a broadband infrared LED light source, a waveguide sensing spiral, and a 1,024-channel on-chip dFT spectrometer for spectral analysis as shown in Figure 16e. This device was optimized for a silicon material platform as shown in Figure 16f. Silicon has been selected as an ideal sensing material due to its low bending losses and highly integrable manufacturability. This design is compliant with the capabilities of AIM foundry (SUNY Poly, Albany) to ensure high quality fabrication and device performance. The proposed photonic circuit design has been developed by modeling and optimizing each of the individual device components using high-throughput full-vectorial FDTD computations, performed using a GPU-accelerated workstation with the Lumerical DEVICE Suite. Following the optimization of these structures, the finalized individual passive design components were submitted for fabrication in the AIM Foundry (SUNY Poly, Albany) Passive MPW run. These structures were then fabricated and tested to characterize their performance and inform design improvements for future devices.

## 2.2.2 Multimode Interferometer Design

The first essential component within the dFT spectrometer is a 1x2 splitter at the MZI input to evenly split the initial optical signal between the two branches. A multimode interferometer (MMI) is a promising solution for this application that relies on the excitation of many higher-order symmetric modes within a multimode region as shown in Figure 17 [28]. The propagation of these higher-order modes with different propagation coefficients causes mode beating with N-fold images of the input mode being formed periodically at different locations along the length of the device. This mode beating pattern has been well-studied and understood such that the length of the MMI required to produce a certain number of output images is given by Equation 2 below, where  $\beta_0$  and  $\beta_1$  represent the propagation constants for the fundamental and second-order modes for the given polarization in the multimode region.

$$L_{MMI} = \frac{3\pi}{4N(\beta_0 - \beta_1)} \quad (2)$$

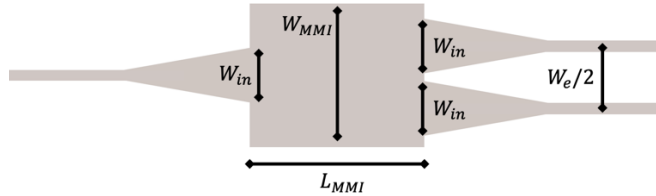


Figure 17. Schematic of the input 1x2 MMI labeled with the critical device dimensions.

One of the many benefits of using a 1x2 MMI for this application is that the power splitting between the two output waveguides is always inherently even due to the symmetry of the device. Some other important performance metrics for these MMIs include the bandwidth and total optical loss (or total power transmission). MMIs can achieve relatively broadband transmission if appropriately designed with a wider multimode region that supports the excitation of many high-order modes. However, this results in a larger device footprint which may not be possible or desirable for all applications. The optical loss of these devices can often be limited by gradually tapering the input waveguide to increase the modal overlap and thus minimize the insertion loss between the input waveguide and the wider multimode region. However, the optimal input waveguide width, output waveguide separation, and MMI length are all dependent on wavelength,

so maintaining low radiation and insertion losses can become more challenging for broadband designs.

Table 1. Calculated and simulation parameters for a 4 $\mu$ m wide 1x2 MMI at a central wavelength of 2.25 $\mu$ m.

MMI Parameter	Optimization Range	Analytical Value	MMI Parameter	Optimization Range	Analytical Value
$\lambda_0$	--	2.25 $\mu$ m	$W_{\text{MMI}}$	--	4.0 $\mu$ m
$n_{\text{slab}}$	--	3.4442	$W_{\text{in}}$	1.1 – 1.7 $\mu$ m	1.15731 $\mu$ m
$n_{\text{clad}}$	--	1.4337	$W_e$	--	4.09546 $\mu$ m
$n_{\text{eff},0}$	--	2.503918	$L_{\text{MMI}}$	8.5 – 9.5 $\mu$ m	9.04321 $\mu$ m
$n_{\text{eff},1}$	--	2.457267			

Since MMIs are fairly well-studied and well-understood devices so there are several governing equations that can be used to evaluate the optimized device dimensions such as the length ( $L_{\text{MMI}}$ ), input waveguide width ( $W_{\text{in}}$ ), and output waveguide separation ( $W_e/2$ ) as shown below in Equations 3-5. For a 1xN MMI, the multimode region width must be designed to support at least N+1 symmetric higher-order modes, and increasing this width can help to increase the bandwidth of the device. Therefore, in order to develop a broadband 1x2 MMI for the 2.0 to 2.5 $\mu$ m wavelength range, the initial simulation width was chosen to be 4 $\mu$ m, which supports several symmetric higher-order modes. For the central wavelength of 2.25 $\mu$ m, the intrinsic and calculated device parameters are shown in Table 1.

$$L_{\text{MMI}} = \frac{3\pi}{4N(\beta_0 - \beta_1)} \quad (3)$$

$$W_{\text{in}} = \frac{1}{\sqrt[4]{2N}} \sqrt{\lambda_0 W_e / n_{\text{slab}}} \quad (4)$$

$$W_e = W_{\text{MMI}} + \left( \frac{\lambda_0}{\pi} \right) \left( \frac{n_{\text{clad}}}{n_{\text{slab}}} \right)^{2\sigma} \left( \frac{1}{\sqrt{n_{\text{slab}}^2 - n_{\text{clad}}^2}} \right) \quad (5)$$

Based on these calculated analytical values, this initial MMI (MMI A) was simulated using Lumerical FDTD with the resulting electric field profiles for various wavelengths as well as the

overall transmission shown below in Figure 18. As evidenced by these results, the MMI demonstrated high transmission of greater than 85% up to approximately  $2.25\text{ }\mu\text{m}$ , but the transmission steadily decreases down to only 63% for longer wavelengths. By taking a closer look at the electric field profiles for this device, it is evident that there is some more significant radiation loss at the MMI output for the longer wavelengths as they begin to approach a third-order mode profile. Therefore, further fine optimization of the MMI dimensions, in particular the length of the MMI, could help to reduce these losses and improve the transmission across the entire bandwidth.

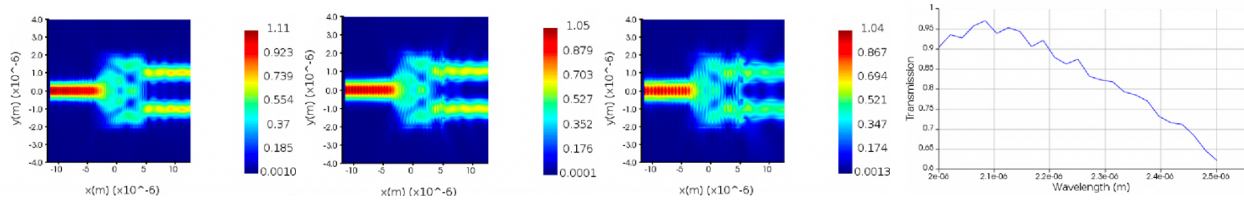


Figure 18. Electric field profile for wavelengths of  $2.0\text{ }\mu\text{m}$ ,  $2.25\text{ }\mu\text{m}$ , and  $2.50\text{ }\mu\text{m}$ .

To further optimize this device, a fine parameter sweep was performed for the MMI length over the range of  $8.5\text{ }\mu\text{m}$  to  $9.5\text{ }\mu\text{m}$  with a step size of  $0.1\text{ }\mu\text{m}$ . The results shown below in Figure 19 suggest that a slightly shorter MMI length of approximately  $8.9\text{ }\mu\text{m}$  demonstrates superior broadband capabilities and improves the transmission at longer wavelengths by over 5%. However, the electric field profile of this  $8.9\text{ }\mu\text{m}$  long device (MMI B) at a wavelength of  $2.5\text{ }\mu\text{m}$  still indicates evidence of radiation losses at the MMI output.

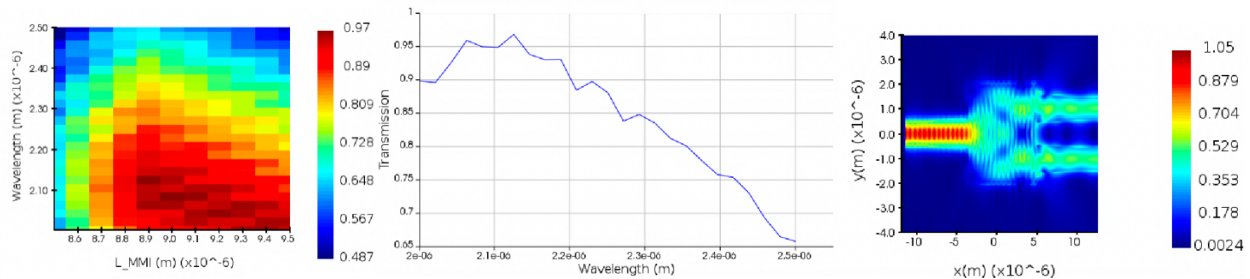


Figure 19. Fine parameter sweep optimization results for varying MMI length.

To further improve the power transmission at this wavelength, a second fine parameter sweep was performed for the output waveguide width in an effort to recollect more of this light that is distributed towards the center of the MMI. These results are shown below in Figure 20 for this

final design, MMI C, and demonstrate further improvement in the overall power transmission at longer wavelengths up to approximately 73%.

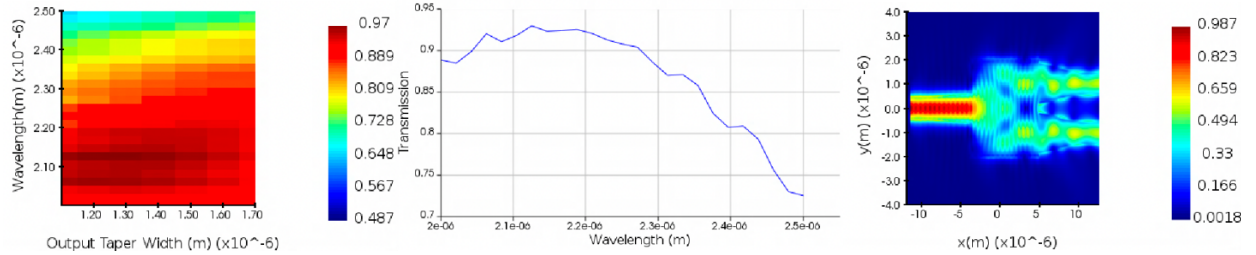


Figure 20. Fine parameter sweep optimization results for a) varying the output waveguide taper width and b) the final optimized device transmission spectrum and c) electric field profile (2.5 $\mu$ m wavelength) for an 8.9 $\mu$ m long MMI with 1.7 $\mu$ m wide output tapers.

Table 2 summarizes the relevant figures of merit for the input MMI component, including the average output power transmission and variation over the entire spectral range as well as the 1dB device bandwidth. As expected, the average output power transmission increased with each design iteration while the power transmission variation decreased by nearly 4%. Additionally, the 1 dB device bandwidth significantly increased from 0.32 $\square$ m to 0.43 $\square$ m from the initial to final design, covering approximately 86% percent of the desired bandwidth and demonstrating adequate performance for use in the dFT spectrometer system.

Table 2. Summary of MMI performance metrics including the average output power transmission and variation as well as the 1 dB bandwidth for several design iterations.

MMI Design	Average Output Power Transmission (%)	Power Transmission Variation (%)	1 dB Bandwidth ( $\square$ m)
A	83.6085	8.80521	2.32
B	84.7291	7.96124	2.36
C	86.8039	5.12187	2.43

### 2.2.3 Adiabatic Coupler Design

One of the most important devices within this dFT spectrometer system is a 2x2 coupler. The 2x2 coupler is an essential component within the optical switches in each arm or the reconfigurable

MZI and is responsible for even splitting and recombination of the optical input signal. Figure 21 below illustrates the design of a single switching stage within the spectrometer composed of two 2x2 couplers with a thermo-optic phase shifter placed in between to enable full optical switching.

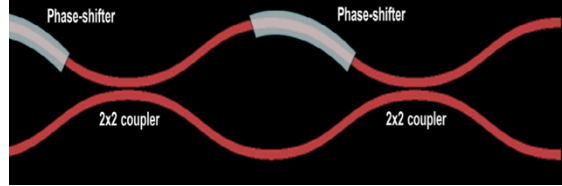


Figure 21. Single optical switch composed of two adiabatic couplers with a thermo-optic phase shifter in between.

While previous demonstrations of the dFT spectrometer have used directional couplers for these 2x2 switching components, these devices have a very narrow bandwidth since they rely on the mode interaction and beating between the even and odd supermodes in the coupling region. As a result, the optimized coupling length for a given power coupling ratio is given by Equation 6 below which has a strong dependence on the refractive index difference between the two supermodes and the central wavelength [24].

$$\kappa^2 = \frac{P_{\text{cross}}}{P_0} = \cos^2 \left( \frac{\pi |n_{\text{eff,even}} - n_{\text{eff,odd}}|}{\lambda_0} L \right) \quad (6)$$

While there are many benefits to these directional couplers given their relatively compact design and tunable coupling ratios, their narrow bandwidth would limit their efficiency in the proposed broadband, mid-infrared dFT spectrometer. Adiabatic couplers are a superior alternative for this application since they demonstrate broadband transmission due to the fact that they do not excite any higher order modes and thus do not rely on the mode interaction or beating between different modes to achieve optical coupling. As shown in Figure 22, adiabatic couplers instead ensure that only one fundamental mode is excited at all times within the coupler and gradually convert this mode from a single, tapered waveguide to either the even or odd mode of two identical waveguides separated by a small coupling gap. In addition to the broadband capabilities of adiabatic couplers,

they are also fairly robust and insensitive to fabrication imperfections since they do not require a precise coupling length.

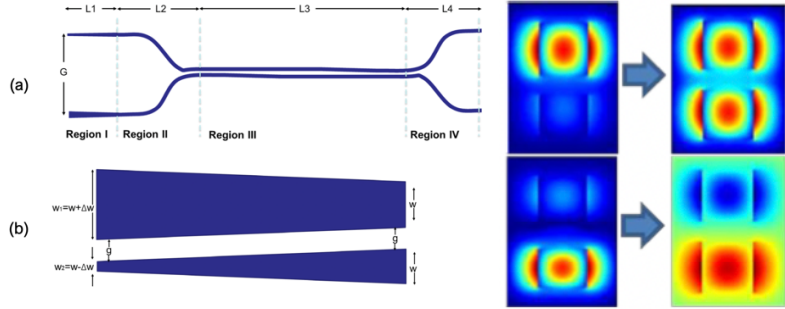


Figure 22. Adiabatic coupler geometry and the c) even and d) odd supermodes that can be realized based on which input waveguide is excited.

For this application within the dFT spectrometer, the key requirements include the adiabatic coupler device bandwidth, total transmission loss, and splitting ratio variation. The total transmission loss varies as a function of wavelength and results from the insertion loss and imperfect mode overlap or power coupling between the input waveguide mode and the output supermode as well as the linear waveguide propagation losses that can start to have an effect due to the long, gradual taper region within the adiabatic coupler. The power splitting ratio variation is a measure of the waveguide output power deviation from the expected value of 50%. Minimizing this FOM is essential to ensure approximately even power splitting between both outputs of the adiabatic coupler over the entire spectral range and consequently improve the overall dFT spectrometer device performance.

Once the initial input signal is evenly split between the two arms of the MZI, there is a cascade of full optical switches that redirect the incoming signal through waveguides of different lengths to achieve a tunable optical path length difference. For this broadband, mid-infrared dFT spectrometer, each optical switch is composed of a two  $2 \times 2$  3dB adiabatic couplers separated by a thermo-optic phase shifter. Since these adiabatic couplers utilize tapered waveguides with widths ranging between  $w_0 \pm \Delta w$ , it is essential to choose an initial waveguide width  $w_0$  that supports only a single fundamental mode over the entire desired wavelength spectrum while still maintaining relatively low loss. From simulations using Lumerical MODE, Figure 23 illustrates the evaluated propagation loss versus wavelength for various waveguide widths. For narrower

waveguide widths, the propagation loss increases significantly for longer wavelengths which would limit the overall transmission within this spectral. Therefore, an intermediate width of  $w_0 = 900\text{nm}$  was chosen as this geometry demonstrates lower losses across the entire spectrum while still limiting the excitation of any higher-order modes supported at shorter wavelengths that begin to emerge for widths greater than approximately 1000nm.

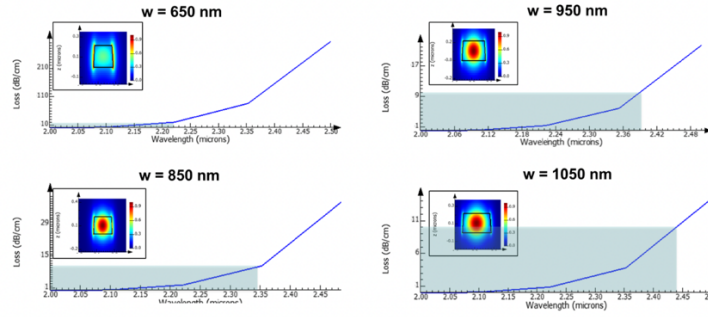


Figure 23. Evolution of loss rate within the spectral band between  $2.0 \mu\text{m}$  and  $2.5 \mu\text{m}$ ; for the fundamental TE mode of SOI buried waveguides with rectangular cross sections, 220 nm high and  $650\sim1050$  nm wide. Inset figures show mode transverse profiles for each waveguide design (all calculated for  $2.5 \mu\text{m}$  wavelength).

After identifying an appropriate value for the initial waveguide width  $w_0$ , the desired taper variation  $\delta w$  was evaluated by performing several mode overlap calculations in Lumerical mode. Since the broadband operation of an adiabatic coupler is based on the excitation of only one supermode of the system in region III, this indicates that for an input signal through the top, wide port, the optical power should mostly be coupled to the fundamental supermode of the two-waveguide system ( $\text{TE}_{00}$ ) while input signals through the bottom, narrow port should be coupled to the first higher-order supermode ( $\text{TE}_{01}$ ). Therefore, to determine the optimal  $\delta w$  to achieve this desired coupling behavior, a sweep of the  $\delta w$  parameter between  $0.0\mu\text{m}$  to  $0.3\mu\text{m}$  was performed while calculating the mode overlap between the modes of the single input waveguides and the supermodes of the two-waveguide system in region III. These results are shown below in Figure 24, which indicate that the optimal range for  $\delta w$  lies between  $\sim0.15\mu\text{m}$  to  $0.20\mu\text{m}$  as indicated by the dark gray shaded regions in each plot. Within this width variation, the desired optical coupling to the  $\text{TE}_{00}$  and  $\text{TE}_{01}$  supermodes for inputs from the top and bottom ports, respectively (shaded in

blue) is greater than 95% for all wavelengths. Additionally, there is minimal power coupling (less than  $\sim 1.5\%$ ) to the higher-order TE<sub>02</sub> supermode for both input ports.

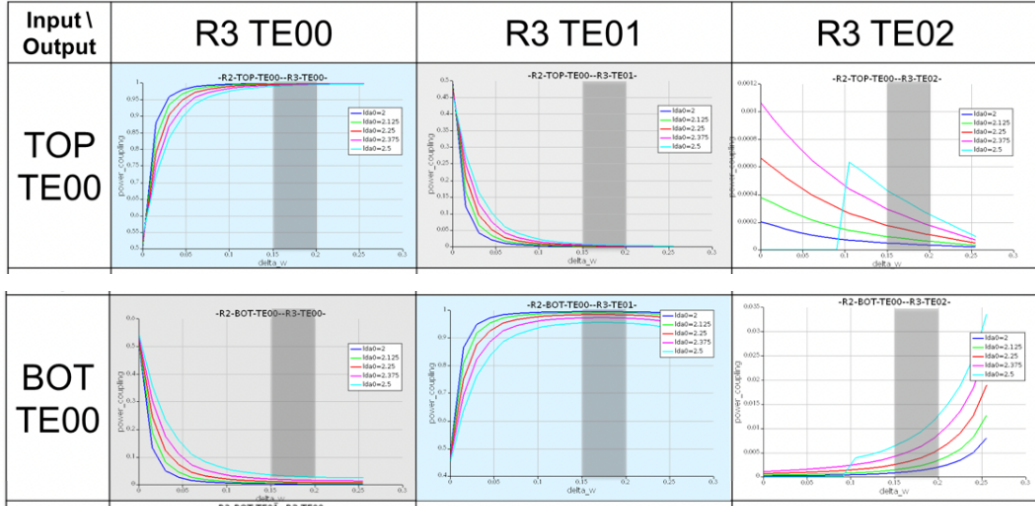


Figure 24. Mode overlap calculations between the fundamental modes of the input waveguides (with widths given by  $w_0 + \Delta w$  and  $w_0 + \Delta w$ ) and the first supermodes of the two-waveguide system in the coupling region III.

After identifying a suitable range of values for the taper width variation  $\Delta w$ , several FDTD simulations were performed to conduct a fine parameter sweep of  $\Delta w$  between 160nm to 190m with a fixed input waveguide width ( $w_0$ ) of 900nm, a coupling gap (g) of 110nm, and a coupling length (L) of 300 $\mu$ m. This coupling gap was chosen at a minimum value of 110nm to increase the mode overlap and thus reduce the coupling length while still satisfying common fabrication limitations of at least  $\sim 100$ nm gap between features. The coupling length for this parameter sweep was chosen to be 300 $\mu$ m assuming that this is long enough for an adiabatic transition between the two modes. Two of these transmission results are shown below in Figure 25 for  $\Delta w$  of 182nm and 190nm and confirm that the taper width variation of 182nm demonstrates the most even power splitting with minimal variation across the entire spectral range.

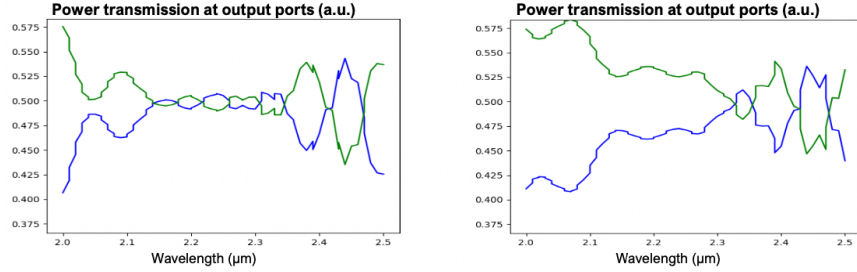


Figure 25. FDTD simulation results for two different  $\Delta w$  values of a) 182nm and b) 190nm.

The final round of optimization for this 2x2 adiabatic coupler involved a parameter sweep of the coupling length ( $L$ ) between 230 $\mu\text{m}$  to 330 $\mu\text{m}$ . While it was expected that longer coupling lengths could lead to better performance and produce more even power splitting, the results shown below in Figure 26 demonstrate superior performance and minimal power transmission variation for an intermediate coupling length of 270 $\mu\text{m}$ , which was selected for the final, optimized 2x2 adiabatic coupler.

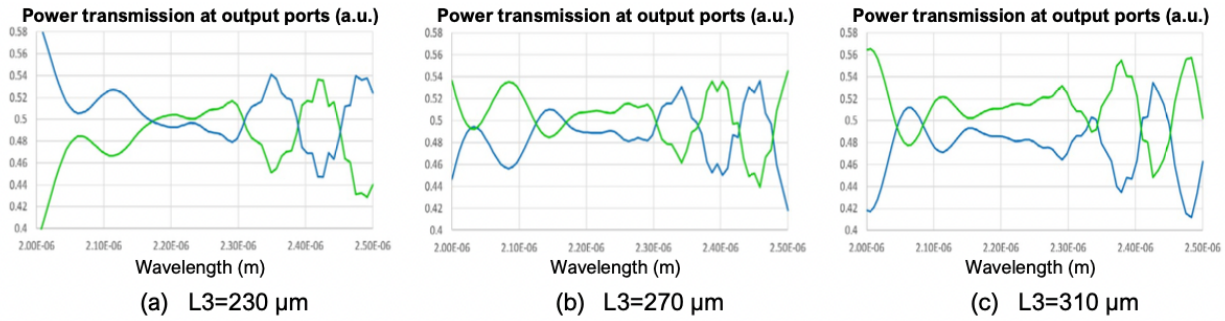


Figure 26. Adiabatic coupler power transmission at the top (blue) and bottom (green) output ports for varying coupling lengths of a) 230 $\mu\text{m}$ , b) 270 $\mu\text{m}$ , and c) 310 $\mu\text{m}$ .

The final transmission and output phase spectra for the optimized adiabatic coupler are shown below for inputs from both the wide, top port and narrow, bottom port. An S-parameter sweep was also performed in Lumerical FDTD for this fully optimized adiabatic coupler design to extract the S-parameter matrix and phase profile for this device and enable faster, simplified system-level calculations in the future.

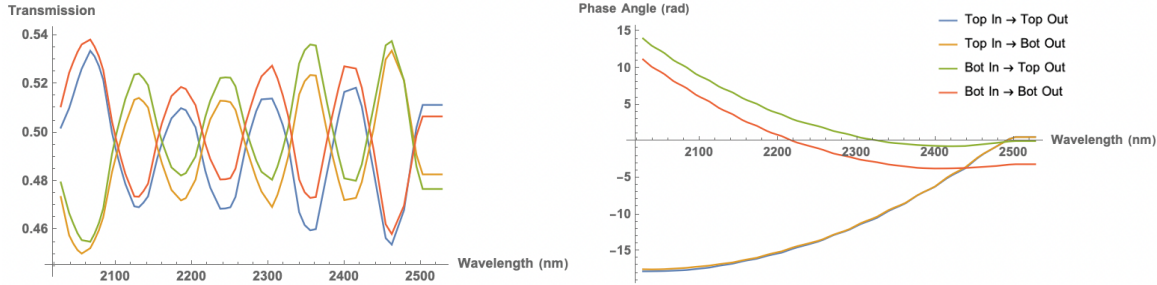


Figure 27. a) Transmission and b) output phase spectra for all input and output waveguide combinations of the optimized adiabatic coupler with  $w_0 = 900\text{nm}$ ,  $\Delta w = 182\text{nm}$ ,  $g = 110\text{nm}$ , and  $L = 270\text{ }\square\text{m}$ .

The overall performance of this optimized 2x2 adiabatic coupler is summarized below in Table 3. The first relevant figure of merit is the average output power transmission and variation for each output port over the entire spectral for inputs from both the wide, top waveguide and narrow, bottom waveguide. For this optimized design, the average output power transmission is extremely close to the desired 3dB splitting for each output with less than 2% variation across the entire spectrum. Additionally, the average loss for inputs from the top and bottom waveguides are only -0.0423dB and -0.0410dB, respectively, which indicates a very broadband device that covers the entirety of the desired bandwidth and demonstrates excellent performance for incorporation with the dFT spectrometer system.

Table 3. Summary of 2x2 adiabatic coupler performance metrics including the average output power transmission and variation as well as the average loss for all input/output combinations.

Input/Output	Average Output Power	Power Transmission	Average Loss (dB)
	Transmission (%)	Variation (%)	
Top → Top	49.4537	1.79401	$-0.0423 \pm 0.015$
Top → Bottom	49.0304	1.77520	
Bottom → Top	49.7699	1.91145	$-0.0410 \pm 0.026$
Bottom → Bottom	50.2479	1.76911	

## 2.2.4 Thermo-Optic Phase Shifter Design

Another important component within the dFT spectrometer system is the thermal phase shifter that is placed between two adiabatic couplers in each switch. The thermal phase shifter is composed of

a thin metal heater placed above the optical waveguide as shown in Figure 28. When a voltage is applied and current runs through the metal heater, the system dissipates heat as a result of resistive Joule heating. As the temperature of the waveguide material below begins to increase, the refractive index of the waveguide material also changes due to thermal expansion of the crystal lattice and a shift in the resonance or bandgap energy. The resulting thermo-optic coefficient ( $\frac{dn}{dT}$ ) consequently results in a change in the propagation coefficient and generates a phase shift for light propagating within the corresponding waveguide given by Equation 7 below where  $\Delta T$  is the change in temperature of the waveguide and  $L$  is the waveguide propagation length.

$$\Delta\phi = \frac{2\pi}{\lambda} \left( \frac{dn}{dT} \right) \Delta TL \quad (7)$$



Figure 28. Cross-sectional view of a thermal phase shifter with a metal or semimetal heater placed several microns above the Si waveguide.

There are several performance metrics for thermo-optic phase shifters that are applicable to this dFT spectrometer system. One key figure of merit includes the efficiency of the phase shifter, which refers to how effectively the temperature of the waveguide changes for a given applied power. The most standard metric for thermo-optic phase shifters is thus the  $P_\pi$ , which refers to the amount of input power required to induce a phase shift of  $\pi$  radians. Some variables that affect the thermal efficiency of these devices include the thermal conductivity ( $k = [\frac{W}{m \cdot K}]$ ) of all materials within the system as well as the spacing and geometry of the heater and waveguide. While it is often possible to improve the thermal efficiency by decreasing the separation between the waveguide and metal heater to maximize the thermal conductance, it is essential to compare this benefit with another key figure of merit which is the optical propagation loss. As the metal heater approaches the waveguide, the evanescent field starts to overlap and interact with the metal which

can lead to very high propagation losses as a result of metal absorption and interfacial scattering [25]. Therefore, it is important to consider the entire system when designing these thermo-optic phase shifters to maximize efficiency while also reducing the propagation losses below an acceptable limit for the desired system-level application.

In order to create a full optical switch that enables reconfiguration of the MZI with varying arm lengths, it is necessary to design a thermo-optic phase shifter to be placed between the two adiabatic couplers in each individual switch. The thermo-optic phase shifter must be capable of producing at least a  $\pi$  phase shift in order to achieve full switching, while also demonstrating high efficiency and low optical loss. As such, the first simulation involved modeling and optimizing the thermal stack geometry and particularly the separation between the waveguide and metal heater layers in the Lumerical MODE solver. For a fixed aluminum metal heater thickness and width defined by certain fabrication parameters, the linear optical propagation loss was simulated as a function of the separation between the waveguide and metal layers. As shown Figure 29a below, the optical propagation loss due to absorption and interface scattering from the metal layer exponentially decreases with increasing separation between the waveguide and metal layers. This is further illustrated by Figure 29b-c which shows the waveguide electric field profile at a  $2.25 \mu\text{m}$  wavelength on a logarithmic scale. As the metal layer shifts down towards the waveguide, there is greater interaction with the evanescent field that results in higher propagation losses. Therefore, the minimum separation between these two layers has been chosen to be  $\sim 1.25 \mu\text{m}$  such that the optical propagation loss is less than  $0.01 \text{ dB/cm}$ .

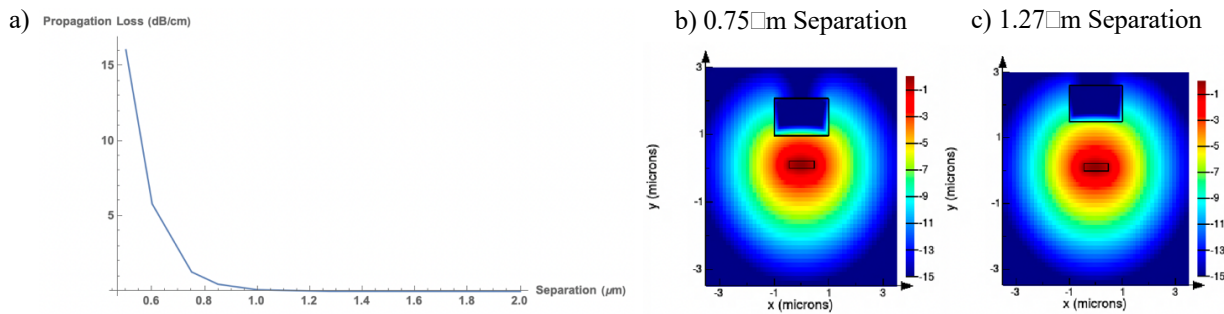


Figure 29. a) Linear waveguide propagation losses as a function of the separation distance between the waveguide and metal heater layers and the corresponding electric field profiles on a logarithmic scale for a separation of b)  $0.75 \mu\text{m}$  and c)  $1.27 \mu\text{m}$ .

After determining the desired thermal stack geometry to minimize optical loss, thermal modeling was performed using Lumerical HEAT to solve the steady state heat equation and determine the expected change in waveguide temperature for a given input power. In order to accurately develop this thermal phase shifter simulation, the thermal conductivities of each material were added to the model along with the appropriate Neumann and Dirichlet boundary conditions. These boundary conditions assume the derivative of the temperature gradient normal to the boundary to be zero and a constant substrate temperature (due to the high thermal conductivity of the Si handle wafer in contact with the room temperature surroundings), respectively. The thermal simulation results are shown below in Figure 30a-c and demonstrate the expected change in the waveguide temperature for different applied power ranging from 0.02W to 0.05W. Based on these results, the phase shift for various wavelengths can be calculated using Equation 7 with the appropriate thermo-optic coefficient for the silicon waveguide given by  $\frac{dn}{dT}(\lambda) \approx 1.94 * 10^{-4} - 8 * 10^{-9} * \lambda$  [26]. The resulting phase shift versus applied power is shown in Figure 30d below and demonstrates a  $P_\pi$  of approximately 57mW at the central wavelength of 2.25 $\mu$ m, which is comparable to other metal thermo-optic phase shifters [27].

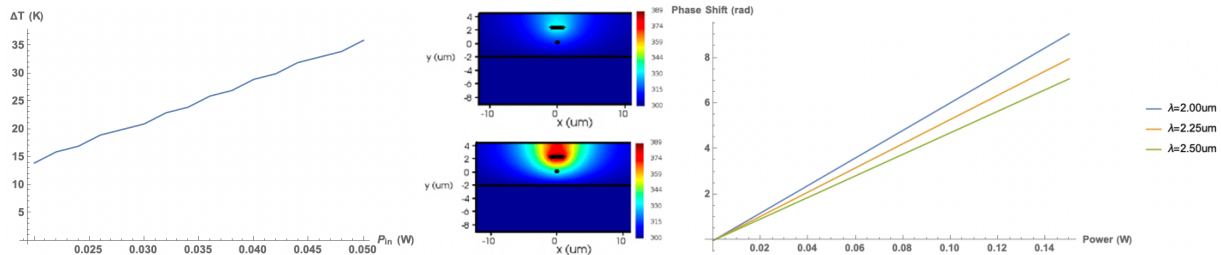


Figure 30. a) Change in waveguide temperature for varying input power ranging from 20mW to 50mW and the corresponding temperature profiles for applied powers of b) 20 mW and c) 50 mW. d) Resulting phase shift as a function of input power for a waveguide length of  $L=100\mu\text{m}$ .

After successfully demonstrating a  $\pi$  phase shift, this thermos-optic phase shifter can be placed between two adiabatic couplers to create a full optical switch. In order to simplify this simulation, the S-parameter matrix and phase output of the optimized directional coupler was utilized to calculate the expected transmission spectrum given by Equation 8 below where  $\phi_{\text{topTop}}$  corresponds to the output phase for light coupled from the top input to the top output, etc., AC1

corresponds to first adiabatic coupler propagation matrix, TPS corresponds to the thermal phase shifter, and AC2 corresponds to the second adiabatic coupler flipped over the vertical axis.

$$\begin{bmatrix} e^{i\phi_{topTop}} & e^{i\phi_{topBot}} \\ e^{i\phi_{botTop}} & e^{i\phi_{botBot}} \end{bmatrix}
 \begin{bmatrix} e^{i\phi_{addedTopTPS}} & 0 \\ 0 & e^{i\phi_{addedBotTPS}} \end{bmatrix}
 \begin{bmatrix} e^{i\phi_{topTop}} & e^{i\phi_{botTop}} \\ e^{i\phi_{topBot}} & e^{i\phi_{botBot}} \end{bmatrix}
 \begin{bmatrix} E_{in,top} \\ E_{in,bot} \end{bmatrix} = \begin{bmatrix} E_{out,top} \\ E_{out,bot} \end{bmatrix}$$

AC2                    TPS                    AC1

(8)

Therefore, for an added thermal phase shift of  $\phi_{addedTopTPS} = \pi$  and  $\phi_{addedBotTPS} = 0$ , the resulting power transmission for an input to the top port of the first adiabatic coupler is shown below in Figure 31a to demonstrate the cross state of the optical switch. Alternatively, for no added thermal phase shift ( $\phi_{addedTopTPS} = 0$  and  $\phi_{addedBotTPS} = 0$ ), the switch returns to the bar state as shown in Figure 31b.

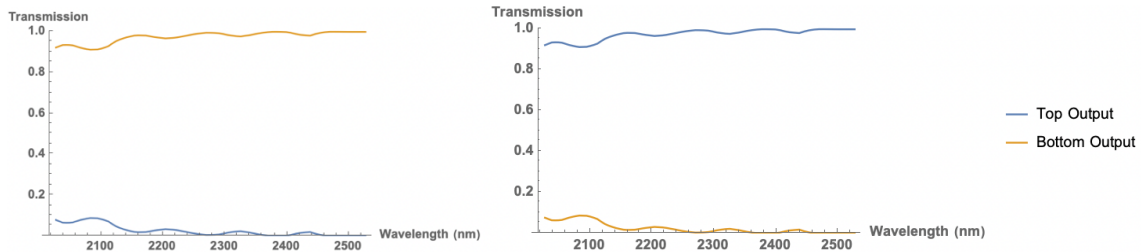


Figure 31. Calculated power transmission spectra of the resulting optical switch for the a) cross state with  $\phi_{addedTopTPS} = \pi$  and  $\phi_{addedBotTPS} = 0$  and b) bar state with  $\phi_{addedTopTPS} = \phi_{addedBotTPS} = 0$ .

Table 4 below summarizes the performance metrics for the resulting optical switch composed of the two adiabatic couplers with a thermos-optic phase shifter in between. This device demonstrates excellent switching capabilities with over 97% power transmitted to the desired output port with minimal variation of ~2% across the entire spectral range. Future work for this broadband, on-chip dFT spectrometer would involve evaluating the relevant performance metrics of the entire spectrometer, such as the bandwidth, loss, power consumption, and spectral resolution by combining all of the components described above.

Table 4. Summary of full optical switch performance metrics including the average output power transmission and variation for the bar and cross states with initial input to the top waveguide port.

Input/Output	Average Output Power Transmission (%)	Power Transmission Variation (%)
Top → Top Cross State	2.82171	2.25790
Top → Bottom Cross State	97.2005	2.25609
Top → Top Bar State	97.1783	2.25790
Top → Bottom Bar State	2.79945	2.25609

## 2.2.5 Edge Coupling Designs for Mid-Infrared LEDs

After optimizing all components of the on-chip dFT spectrometer, some passive waveguide components were fabricated and tested to evaluate the experimental optical losses that would inform the expected urine device sensitivity and to investigate different edge coupling techniques to maximize the coupling efficiency of the infrared light source. These devices were first evaluated at 1550 nm wavelength using a fiber-coupled Maple Leaf system shown below in Figure 32. Both the input fiber and output fiber detector were controlled with precise, piezo-electric stages to achieve optimal, sub-micron alignment with maximum coupling efficiency and performance of the test structures. We also adapted this system for use with a tunable, Chromacity OPO source and mid-IR chalcogenide glass fibers in order to perform additional testing at the target mid-infrared wavelengths between 2.0-2.5  $\mu\text{m}$ .



Figure 32. Fiber-coupled testing system with sub-micron alignment capabilities for the input fiber and output fiber detector coupled into the fabricated AIM device.

Figure 33a below illustrates some of the paperclip spirals and ring resonators of varying lengths, radii, and coupling gaps that were used to evaluate the waveguide propagation and bending losses.

These results were used to determine the expected loss of the overall device to evaluate the required power from the input LED source as well as the responsivity and noise level requirements of the detector to achieve maximum sensitivity. Figure 33b contains four different edge coupling designs with regular and inverse tapers. As detailed in previous reports, two of these designs also include additional SiN waveguide tapers above the Si waveguide layer in order to expand the coupling mode and consequently improve the overall coupling efficiency.

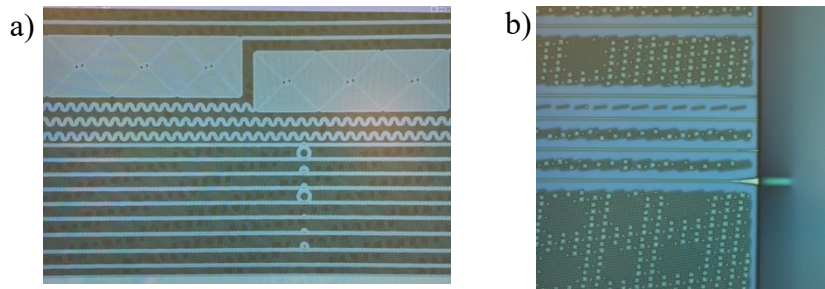


Figure 33. Microscope images of the fabricated devices including a) spirals, bends, and ring resonators utilized for loss characterization and b) three different edge coupling taper designs.

#### 2.2.5.1 NIR Waveguide Loss Characterization

To determine the waveguide propagation loss in the NIR, four long paperclip spirals with lengths of 1, 2, 3, and 4 cm were fabricated and tested. These paperclip spiral waveguides were characterized using a wavelength sweep between 1480nm to 1640nm and the results are plotted below in Figure 34b for four spirals of varying length from 1cm to 4cm. Further processing and analysis of these initial spectra enabled evaluation of the total insertion loss, propagation loss, and bending loss (for the 15  $\mu\text{m}$  radius spiral bends) as a function of wavelength as shown in Figure 34c-e. Based on these results, the total waveguide loss was calculated for each propagation length and compared to the expected waveguide loss spectrum. The expected waveguide propagation loss is between 1.8–2.6 dB/cm for Si waveguides with a 1 $\mu\text{m}$  oxide cladding, so the expected characterization of these structures should lead to a loss spectrum that falls within the bounds of the plot in Figure 34g. This comparison reveals that the experimentally measured waveguide loss closely matches that of the predicted values and falls well within the upper and lower bounds of the simulated propagation losses. These experimental results corroborate and confirm the accuracy of these simulations so that they can consequently be used for further design iterations and improvements. Additionally, these results were used to evaluate the expected loss of the overall

device to evaluate the required power from the input LED source as well as the responsivity and noise level requirements of the detector to achieve maximum sensitivity.

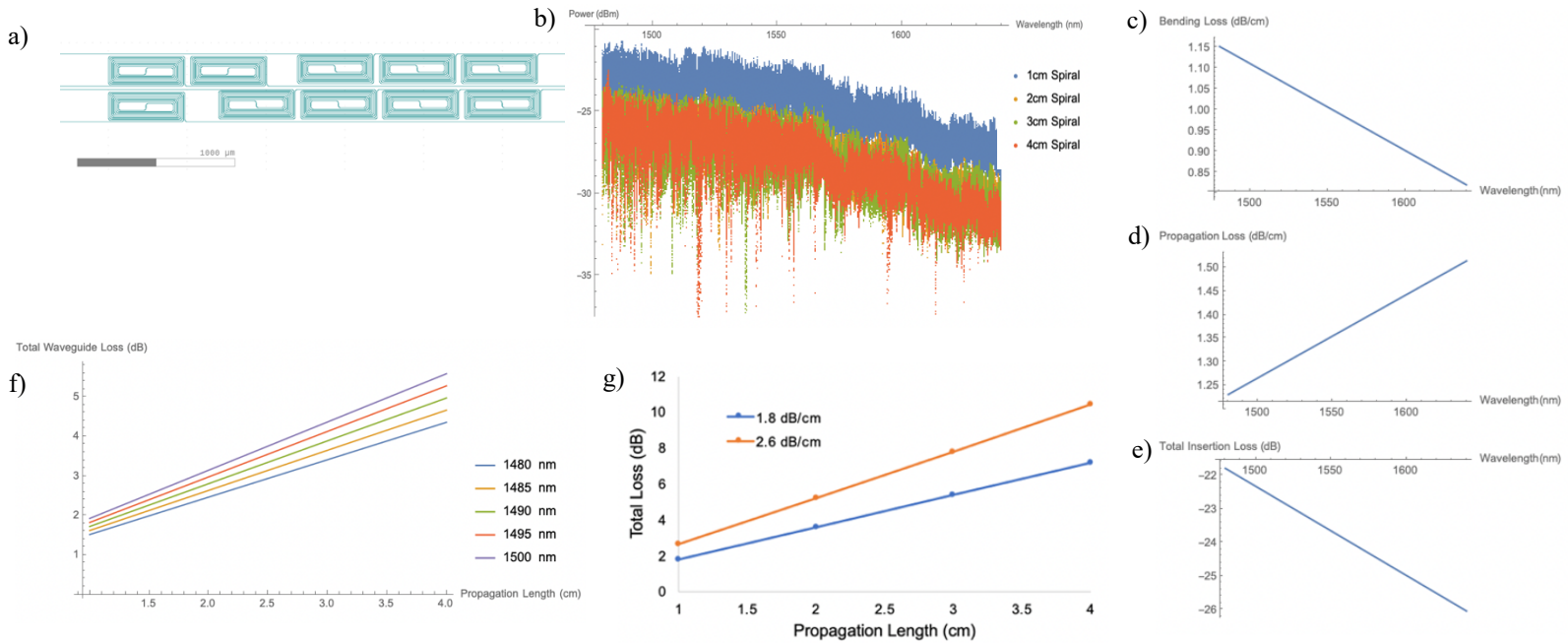


Figure 34. a) Paperclip spirals with propagation lengths of 1, 2, 3, and 4 cm to evaluate waveguide propagation loss. b) Measured power spectra for four paperclip spirals with varying propagation lengths. c) Calculated bending loss, d) propagation loss, e) and insertion loss as a function of wavelength. f) Experimental and g) simulated losses versus propagation length.

#### 2.2.5.2 Mid-IR Waveguide Loss Characterization

While the previous measurements are essential for confirming the validity of the simulation models and the experimental performance of the fabricated AIM chip devices, further measurements were required to experimentally determine the propagation losses at longer wavelengths that will be used within the urine sensing device for absorption spectroscopy. Therefore, we adapted the previously described fiber-coupled Maple Leaf system that is typically limited to wavelengths between 1480nm to 1640nm for use with a tunable, Chromacity OPO source. This new setup enabled additional testing up to wavelengths of 1825nm, which can be used to extrapolate and predict the expected losses at our target wavelength. Figure 35a below shows the transmission spectra for two different light pulses centered at 1645nm and 1745nm. The blue lines represent the

reference spectrum of the Chromacity OPO source, while the yellow lines represent the power transmission through the waveguide.

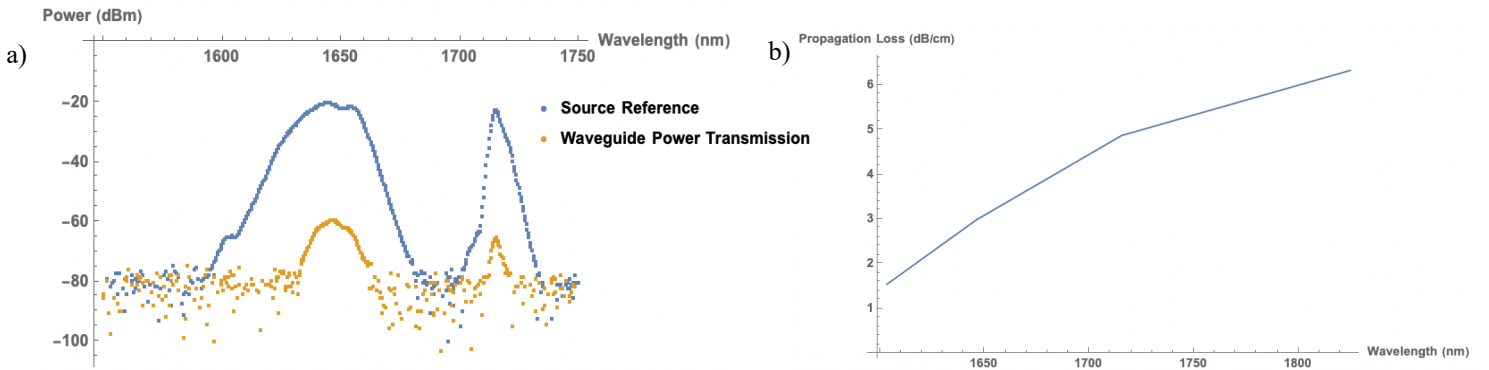


Figure 35. a) Power spectra collected from the Chromacity OPO laser source (blue) and the waveguide output (yellow) for two different peak wavelengths of 1645nm and 1745nm. b) Experimentally determined waveguide propagation losses up to 1825nm wavelength.

After collecting similar data for each wavelength, the transmission spectra were analyzed to determine the approximate propagation loss as a function of wavelength. These results are shown in Figure 35b which confirms that as expected, the propagation loss increases with longer wavelengths due to lower confinement and thus higher potential for absorption, scattering due to sidewall roughness, and more. These results were used to determine the expected overall losses of the device at our target 2.0-2.5  $\mu\text{m}$  wavelength and consequently aid the final simulations and design procedures to ensure high sensitivity within the spectrometer when exposed to the urine analyte.

#### 2.2.5.3 Edge Coupler Design & Characterization

To improve the coupling efficiency from the off-chip LED light source to the photonic integrated circuit (PIC), four different edge couplers were optimized and fabricated by AIM foundry. Figure 36 below illustrates all four edge coupling geometries, including a regular double layer SiN taper, an inverse double layer SiN taper, a straight Si waveguide, a standard inverse Si taper. Table 5 below details the optimized dimensions of each edge coupler design that are compatible with the fabrication capabilities of AIM foundry.

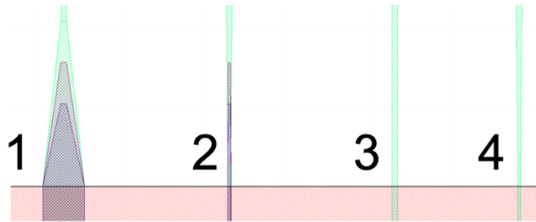


Figure 36. Four different edge coupling designs including, from left to right, a regular double layer SiN taper (1), an inverse double layer SiN taper (2), a straight Si waveguide (3), and a standard inverse Si taper (4). The light green layer represents the bottom Si waveguide layer, while the red and blue regions indicate the middle and upper SiN layers, respectively.

Table 5. Optimized dimensions of the four fabricated and experimentally tested edge coupling designs.

Edge Coupler Design	Layer	Edge Width (um)	End Width (um)	Length (um)
1: Regular Double Layer SiN Taper	Bottom Si	5	0.65	20
	Mid SiN 1	5	0.65	15
	Top SiN 2	5	0.65	10
2: Inverse Double Layer SiN Taper	Bottom Si	0.35	0.65	20
	Mid SiN 1	0.40	0.20	15
	Top SiN 2	0.40	0.20	10
3: Straight Si Waveguide	Bottom Si	0.65	0.65	--
4: Standard Inverse Si Taper	Bottom Si	0.35	0.65	20

The coupling efficiencies and alignment tolerance of these devices were tested for a spectral range between 1480 to 1640nm and the results are shown below in Figure 37. The x-tolerance was evaluated by laterally moving the input fiber from its optimized position in small 1 micron increments. As indicated by the relatively flat blue curve for Edge Coupling Design 1 (EC Design 1) in Figure 37a, the regular double layer SiN taper demonstrated the highest x-offset alignment tolerance which resulted in less than an 8dB coupling loss up to a 10 micron horizontal offset. For the vertical z-offset alignment tolerance measurements shown in Figure 37b, the regular double layer SiN taper (EC Design 1) once again demonstrated the highest vertical alignment tolerance, followed by the inverse double layer SiN taper (EC Design 2). These experimental results confirm the expected simulation results since the two double layer SiN edge coupling designs significantly out-perform the two single-layer Si edge couplers (EC Design 3 and EC Design 4) for positive vertical z-offset transmission. Since the double layer taper designs expand the optical mode in the

vertical direction, this enables high alignment tolerance in this dimension due to improved modal overlap between the fiber mode and the waveguide mode at the edge coupling facet. Based on these experimental results, the regular double layer SiN taper consistently demonstrated the highest alignment tolerance and will consequently be utilized in the final device design to improve coupling efficiency between the light source and PIC.

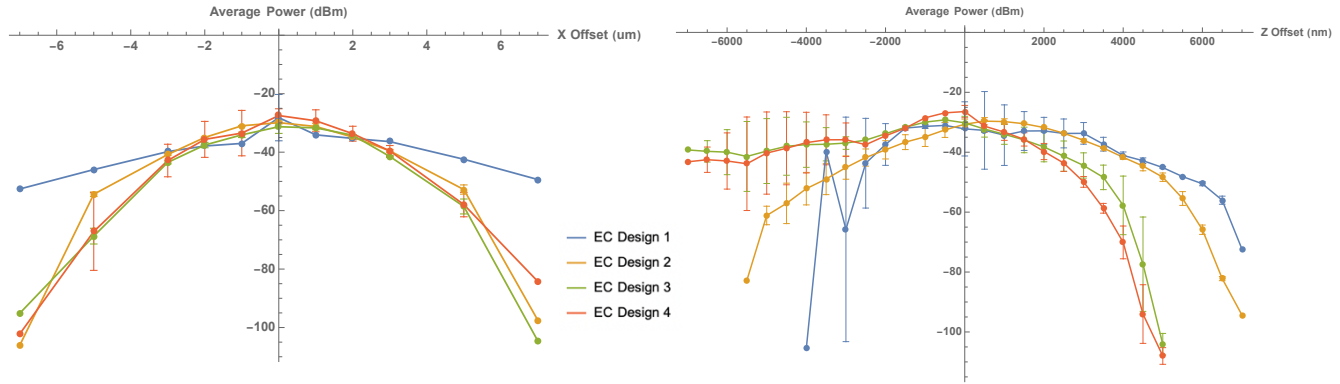


Figure 37. Experimental alignment tolerance transmission results for all four edge coupling designs in the a) lateral x-dimension and b) vertical z-dimension. For both dimensions, the regular double layer SiN taper design demonstrated the highest alignment tolerance (EC Design 1) as indicated by the blue curve that achieves low optical power loss for large misalignment.

## 2.2.6 Packaging via Photonic Wire Bonding

While the edge coupling designs described above successfully demonstrated high alignment tolerance of the input source, additional packaging techniques can be implemented to ensure stable, efficient, and reliable connections between the light source and PIC. Photonic wire bonding (PWB) is a novel, emerging technology that offers an innovative approach to creating high-quality optical connections. PWB has demonstrated high efficiency optical interconnects with low losses in the NIR without requiring precise active alignment. This work investigates the extension of PWB technology for longer, MIR wavelengths to enable high quality packaging solutions for infrared sensing systems.

### 2.2.6.1 Principles of Photonic Wire Bonding Technology

Photonic wire bonding (PWB) technology is inspired by the traditional wire bonding used in electronic circuits but adapted to the optical domain. It involves the use of polymer or glass wires to connect different photonic components, such as waveguides, on a chip. These optical wires can

be precisely positioned and bonded to the chip's surface using advanced fabrication techniques, such as direct laser writing or nanoimprint lithography.

The technology allows for the creation of three-dimensional (3D) optical interconnects, which can navigate around obstacles on the chip and connect components located at different heights. This flexibility is a significant advantage over traditional planar waveguides, which are limited to two-dimensional (2D) layouts and often require complex routing to avoid crosstalk and other interference.

Vanguard Automation, Inc. is currently one of the leaders in PWB technology and has been a key collaborator to advance our photonic integrated circuit (PIC) packaging. Their proprietary approach to PWB that utilizes direct-write 3D laser lithography is based on two-photon polymerization to create single-mode freeform waveguides that connect integrated optical chips to light sources such as fibers, lasers, or LEDs [29]. A schematic of this process is shown below in Figure 38a in which a high-numerical aperture (high-NA) femtosecond laser beam uses two-photon lithography to create the shape of a custom-designed PWB, which optimizes light coupling between two facets being connected. Once the unexposed resist material is removed during development, the final PWB structure is shown in Figure 38b to enable efficient coupling between the device components [29].

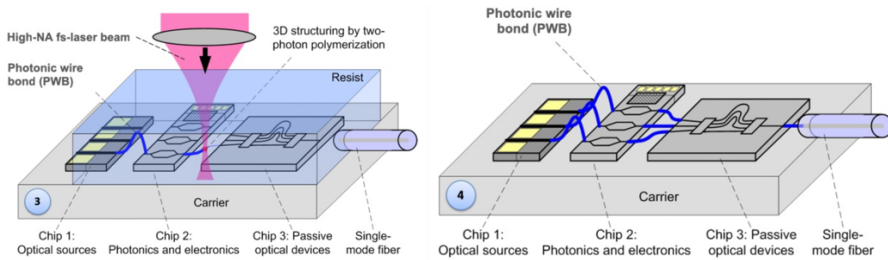


Figure 38. a) PWB waveguide is written using two-photon polymerization to obtain the desired design according to the facet geometries and alignment. b) Development step removes unexposed resist material to obtain a PWB with high optical coupling efficiency.

Photonic wire bonding demonstrates several key advantages for photonic packaging. First, PWB offers considerable design flexibility through its ability to create 3D interconnects that allow for more efficient use of chip space and simplify the routing of optical signals. PWB also achieves

high precision alignment due to the advanced fabrication techniques and consequently realize low optical coupling losses and improved PIC performance. This technology is also compatible with almost any material system, so it can be applied to connect a wide range of photonic components, including those made from different materials, thereby facilitating heterogeneous integration. Lastly, PWB is compatible with mass production techniques, making it suitable for large-scale manufacturing of photonic devices.

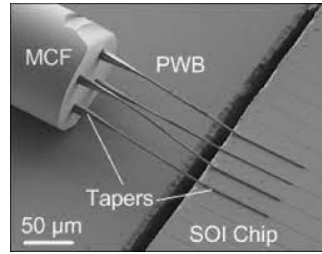


Figure 39. SEM image of a multi-core fiber with several PWB tapers connecting the source to an SOI chip [29].

#### 2.2.6.2 Experimental Results in Mid-Infrared Regime

This technology has currently demonstrated insertion losses between 1 dB to 2 dB in the wavelength range of 1200 nm to 1600 nm but has not yet been tested in the desired mid-infrared (MIR) wavelength range of 2.0 to 2.5  $\mu\text{m}$  required for the urine sensing device. Using some previously fabricated PWB samples with four different edge coupling geometries, we tested the device performance between 1300 nm to 15500 nm to calculate coupling losses. Figure 40 below demonstrates the total loss of the two PWBs at the input and output as well as any optical losses of the PIC in between. For the most optimized design of PWB1-8, the total loss is less than 4dB, which includes the insertion loss from the input and output PWBs as well as any waveguide propagation losses. This indicates that the loss per PWB is less than 2dB as previously demonstrated in other works. Even for less optimized PWB designs (ex: PWB2-7 and PWB4-5), the results below in Figure 40 confirmed the high performance and low coupling losses of the PWBs (less than 5dB per PWB) between 1300 nm to 1550 nm as previously reported in literature.

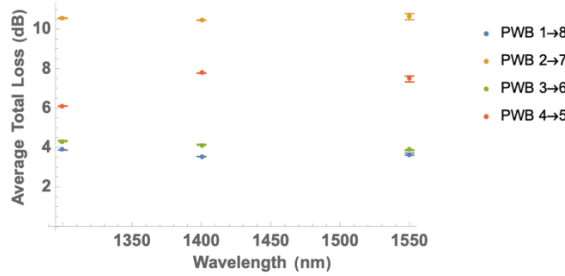


Figure 40. Total optical loss of four different fiber-coupled PWBs to a PIC sample measured for near infrared wavelengths.

After confirming the expected performance of these PWB samples optimized for 1550 nm wavelength, we tested the device performance at 2.1  $\mu\text{m}$  and 2.3  $\mu\text{m}$  to calculate the coupling losses and explore the possibility of applying this technology to the urine sensor. This longer wavelength testing was performed using (i) a Chromacity OPO laser source, (ii) fiber coupled to the PWB connection of the PIC, (iii) with a second PWB connection to an output fiber, and finally (iv) directed to an optical spectrum analyzer (OSA). Figures 41 b and c demonstrate the total loss of the PWB system at longer wavelengths, in a system that was previously optimized for a shorter wavelength of 1550 nm. Despite this 1550 nm wavelength optimization, the photonic wire bonds still demonstrate high coupling efficiency at the longer wavelengths of 2.1  $\mu\text{m}$  and 2.3  $\mu\text{m}$  wavelengths, showing less than 2.5 dB and 7.0 dB loss per facet, respectively.

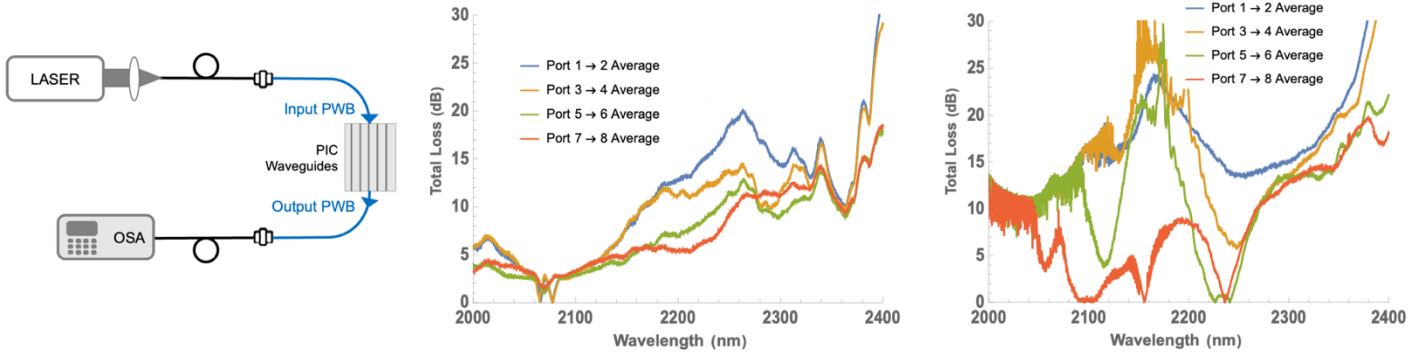


Figure 41. a) Experimental setup for testing PWB loss in the mid-infrared regime using a Chromacity OPO laser source fiber coupled to the PWB connection to the PIC and directed to an OSA for readout. Total optical loss of a fiber-coupled PWB to PIC sample measured around a central wavelength of b) 2.1  $\mu\text{m}$  and c) 2.3  $\mu\text{m}$ .

### 2.2.6.3 Future Work

While the results above demonstrate initial feasibility of PWB utility in the mid-IR wavelength regime, for creating a stand-alone sensing platform, further testing is required with multiple samples, at various wavelengths, to isolate the PWB coupling loss from waveguide propagation loss. For instance, since the Chromacity OPO laser source was rather unstable around the 2.3  $\mu\text{m}$  wavelength range, we are continuing this characterization of the PWB efficiency in the 2.0 to 2.5  $\mu\text{m}$  wavelength range using a pulsed, continuously tunable M-Squared Firefly laser diode source. Additionally, we continue to collaborate with Vanguard Automation, Inc. to optimize the PWB design and demonstrate efficient MIR coupling between our previously-fabricated urine-sensor PICs and ANFT's MIR LED source.

Photonic wire bonding technology represents a significant leap forward in the field of integrated photonics, offering a flexible, precise, and scalable method for connecting photonic components. Its development opens new possibilities for the design and fabrication of advanced photonic circuits, with wide-ranging applications across several industries. As the technology matures, it is poised to become a key enabler of the next generation of optical communication systems, quantum computers, and much more.

## 3. Mid-Infrared PbTe P-N Junction Diode

### 3.1 Motivation & Applications for MIR p-n Junction Diodes

While PbTe thin films have demonstrated high performance as integrated photoconductive detectors with many different applications as described in Chapters 1 and 2, these detectors require an external bias for efficient collection of the photogenerated carriers. Photoconductors are one type of optical detectors which consist of a uniform bulk semiconductor material, such as a lead salt, placed between two metal contacts as shown in Figures 42a-b. When these intrinsic photoconductor materials are illuminated, photons with sufficient energy excite electrons across the bandgap of the detector material, which generates an electron-hole pair as shown in Figure 42c. When an external bias is applied to the detector as shown in Figure 42d, there is a change in conductivity caused by the generation of new charge carriers [9]. As a result, monitoring this

response to either an external current or voltage bias can lead to detection of different signals based on illumination power until the bandedge wavelength [10].

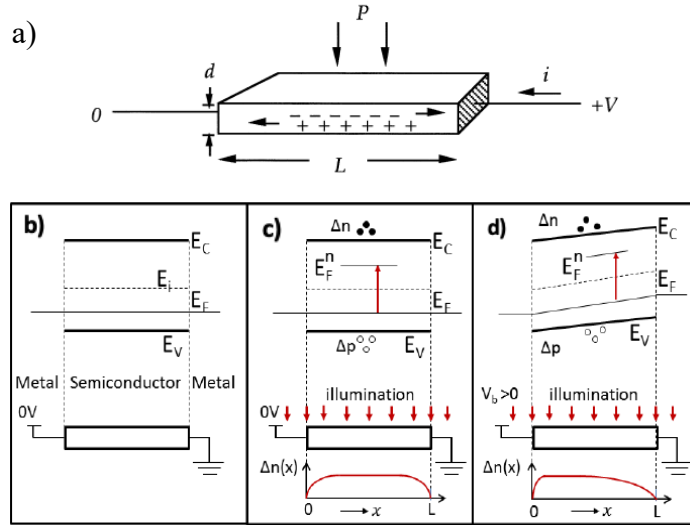


Figure 42. a) Schematic representation of a photoconductive detector and b) the corresponding band diagram. Photodetector response under illumination c) without and d) with a positive external applied bias [9].

Alternatively, p-n junction photodiodes consist of a p-type semiconductor with excess hole majority carriers in direct contact with an n-type semiconductor with excess electron majority carriers. When these two semiconductors with different majority carrier types are placed in contact, it causes a bend within the conduction and valence bands at the interface as shown in Figure 43 to align the Fermi Levels that are shifted towards valence and conduction bands of the p- and n-type regions, respectively. As a result, a built-in electric field is established within this band-bending region known as the depletion layer. When the p-n junction diode is then illuminated with light of sufficient energy to generate electron-hole pairs across the bandgap, the minority carriers generated within the depletion layer drift across the junction (electrons drift towards the n-type region while holes drift towards the p-type region) due to the built-in electric field and generate a photocurrent that can be collected through an external circuit. By creating a p-n junction with small-bandgap semiconductor materials, these p-n junction diodes could enable photovoltaic, zero-bias operation in the mid-infrared regime that could be beneficial for integrated photonic applications that require low energy consumption for widespread adaptation and implementation.

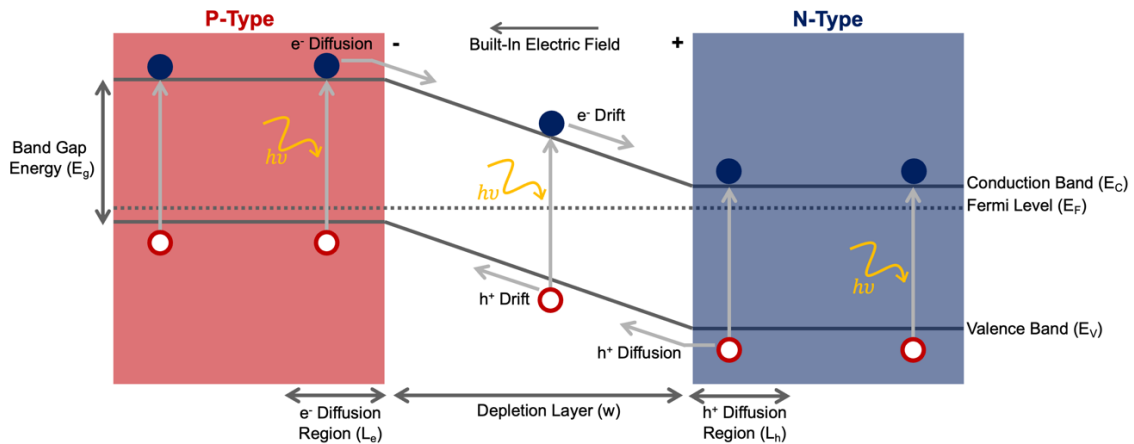


Figure 43. Schematic of a p-n junction device and the corresponding carrier diffusion and drift behavior through the built-in electric field across the depletion layer.

In addition to integrated photonic applications as passive optical detectors, mid-infrared p-n junction diodes are also promising devices for renewable energy generation as photothermal photovoltaic (PV) cells. Renewable energy generation is indispensable to reduce the emission of harmful greenhouse gases from current energy sources and to meet the sustainable development goals of the 21<sup>st</sup> century. As shown in Figure 44, earth continuously emits roughly  $10^{17}$  W of infrared thermal black body radiation (BBR) that is completely wasted and can even contribute to global warming effects if trapped within the atmosphere. Mid-infrared p-n junction diodes could be utilized to convert this infrared BBR energy into electricity and thus provide variable voltage electrical power. The following chapter details design, fabrication, and testing of the first polycrystalline PbTe p-n junctions optimized for high performance in the mid-infrared spectral regime.

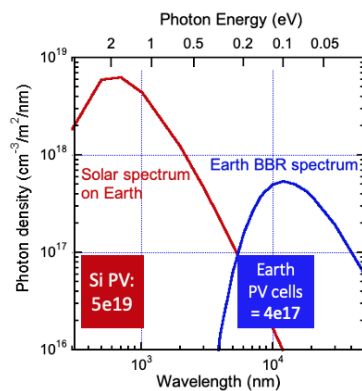


Figure 44. Comparison of the photon flux for the Earth BBR spectrum at 300 K and the solar spectrum on Earth.

## 3.2 Material Characterization & Device Design

### 3.2.1 PbTe Material Characterization

To successfully demonstrate a MIR p-n junction diode, this work builds upon the previous demonstration of PVD thin film PbTe photoconductive detectors. PbTe is an attractive material for mid-infrared diodes as its small bandgap ( $E_g \sim 0.26$  eV) enables efficient carrier generation up to a cutoff wavelength of approximately 4.7  $\mu\text{m}$ . Additionally, the PVD technique utilized for the photoconductive detectors offers a low-cost fabrication method that demonstrates high quality nanocrystalline films deposited onto any large area substrate at room temperature.

The most critical step towards developing a MIR PbTe p-n junction was to precisely control the carrier type and concentration to reliably deposit p- and n-type films with the desired properties to enable efficient diode behavior. To accurately measure the majority carrier type, concentration, and mobility of all films, hall effect measurements were performed at room temperature following the van der Pauw technique outlined by NIST eliminates any contact resistance contributions to the resulting measurements. The samples prepared for hall effect measurements consisted of PbTe thin films with varying thicknesses deposited onto 1  $\text{cm}^2$  substrates (either  $\text{BaF}_2$  or  $\text{SiO}_2$ ) with 350 nm thick triangular tin contacts thermally evaporated onto the corners of the film through a shadow mask as shown in Figure 45.

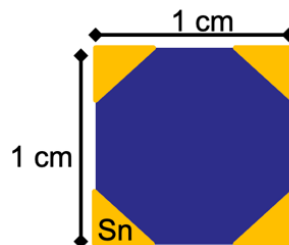


Figure 45. Hall effect contact design with four metal contacts deposited on each of the four corners to accurately measure the carrier concentration, type, mobility, and resistivity of the PbTe thin films.

All of the PbTe-based films were deposited onto room temperature substrates using PVD with the source material created by mixing precise concentrations of each crushed powder material into tantalum boats (SB-6 & SB-6A from R.D. Mathis). The base deposition pressure was between 2-3E-06 Torr for all depositions and increased to approximately 5-7E-05 Torr during the deposition.

The deposition rate was monitored using a quartz crystal monitor and the power applied to the source boat was adjusted accordingly to maintain a deposition rate between 8-10 Å/s. After the deposition rate stabilized and approximately 0.3 kÅ had been deposited onto the crystal monitor, the substrate shutter was opened to begin the film deposition onto the substrate. The substrate shutter was then closed after reaching the desired film thickness (in most cases around 400 nm thick).

As shown in Figure 46, the as-deposited PbTe thin films (99.999% purity Pb(II)Te source material, Thermo Fisher Scientific) demonstrated p-type behavior with fairly stable average carrier concentrations ( $p$ ) around  $5.5\text{E}+17 \text{ cm}^{-3}$  across several depositions with varying film thicknesses (with the exclusion of outlier Sample #4). This p-type nature is likely due to a slightly off-stoichiometric excess of Te in the source material that acts as an acceptor in the resulting PbTe films.

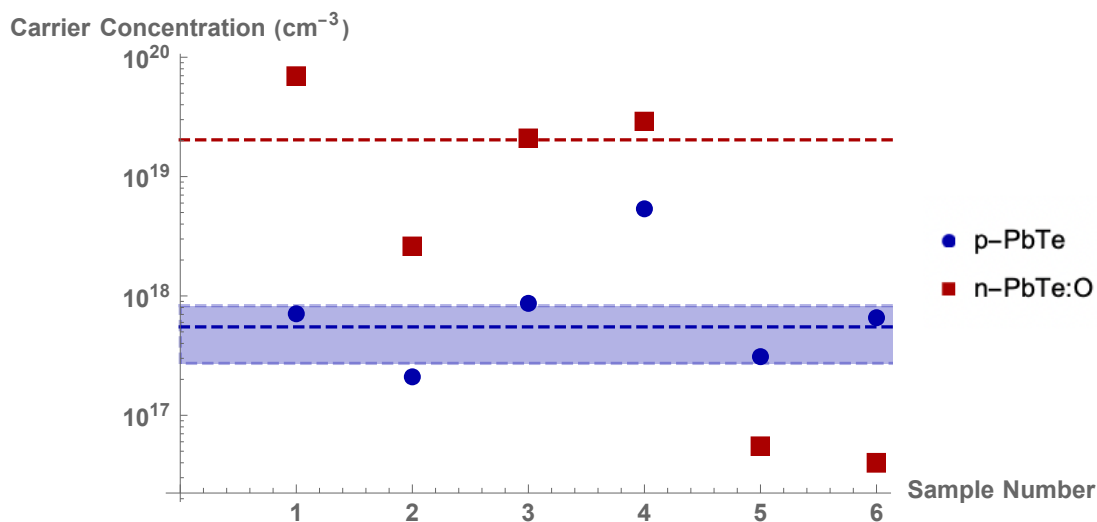


Figure 46. Carrier concentrations measured via Hall effect for six different p-PbTe (blue) and n-PbTe:O (red) samples. The p-PbTe samples demonstrate consistent carrier concentrations (with the exception of outlier Sample #4) with the average and standard deviation marked by the blue dashed line and shaded region, respectively. The n-PbTe:O samples demonstrate a more variable carrier concentration across several orders of magnitude with the average indicated by the red dashed line. The standard deviation for the n-PbTe:O samples is not shown as it is too large and covers the entire plot range.

In order to obtain n-type PbTe films required for the fabrication of p-n junctions, previous works demonstrated that adding varying concentrations of PbO to the PbTe source material during thermal evaporation can lead to n-type conversion above approximately 5% atomic PbO concentration [11]. This n-type conversion with increasing PbO concentration can be explained by the understanding that the PbO acts primarily as a source of additional Pb in the resulting films since the Pb and O dissociate during the thermal evaporation and the volatile nature of the O atoms prevents them from reaching the substrate. Since Pb acts as a donor in Pb chalcogenide materials, the addition of PbO to the PbTe source material consequently creates an n-type film due an off-stoichiometric excess of Pb. This n-type conversion was successfully reproduced with 7 atomic percent PbO added to the source material and demonstrated a high average carrier concentration ( $n$ ) of approximately  $3E+19 \text{ cm}^{-3}$  in the PbTe:O film as shown in Figure 46 for measurements across six different samples. Compared to the p-PbTe films, the n-PbTe:O films demonstrated much greater variability in the carrier concentration across several orders of magnitude for different depositions. This instability can be attributed to variations in the dissociation of the Pb and O from the source material and thus inconsistent oxygen incorporation in the resulting films. Previous works have also demonstrated a decrease in n-PbTe:O carrier concentration over time due to oxygen incorporation, which further explains this unstable behavior. As such, it is essential to measure the n-PbTe:O carrier concentration for each deposition to account for this variability when fabricating future p-n junction devices that are sensitive to changes in the carrier concentration of each layer.

The responsivity of both the p- and n-type PbTe films under a constant  $1 \text{ mA}$  current bias was measured at  $77\text{K}$  using a blackbody source with the photoresponse amplified by a lock-in amplifier. The p-PbTe responsivity spectrum demonstrates a peak around  $3.7 \text{ } \mu\text{m}$  with a much stronger photoresponse than that of the n-type PbTe:O film across the MIR spectral regime. The superior performance of the p-PbTe photoconductor compared to that of the n-PbTe:O material can mainly be attributed to the lower carrier concentration since the responsivity of a photoconductor under constant current bias is inversely proportional to the majority carrier concentration [11].

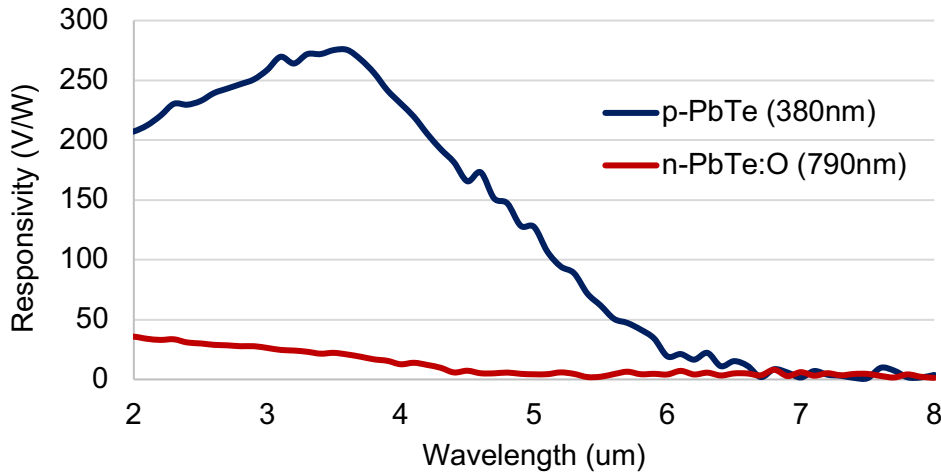


Figure 47. Responsivity spectra for p-PbTe (blue) and n-PbTe:O (red) films demonstrate a cut-off wavelength of approximately 6  $\mu\text{m}$  corresponding to the band-edge. The p-PbTe spectrum has a higher photoconductive response compared to the n-PbTe:O due to its lower carrier concentration by nearly two orders of magnitude.

### 3.2.2 PbTe p-n Junction Device Design & Fabrication

This initial characterization of the optical and electrical properties of the p- and n-type PbTe films was essential to aid in the design optimization of the p-n junction diodes. Since the p-type films demonstrate significantly higher responsivity, the p-type layer was deposited as the top layer to ensure efficient optical absorption and photocarrier generation within the diodes. The initial diodes were designed with a horizontal geometry as shown in Figure 48. The Sn contacts were made directly to the p- and n-type films on either side of the central, overlapping junction. The junction length was kept constant at 2 mm with the Sn contacts placed 3 mm apart (approximately 1 mm from the edge of the junction) while the overlapping junction width was varied between 200 to 1000  $\mu\text{m}$ .

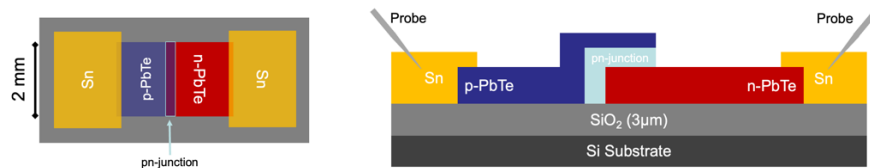


Figure 48. a) Top and b) cross-sectional views of the horizontal device design for the PbTe p-n junction diodes with a 2 mm length and variable overlapping junction width.

For the initial demonstration of these PbTe p-n junction diodes, shadow masks were used to pattern each of the semiconductor and Sn layers within the device. A custom sample holder was designed to ensure accurate fabrication of the PbTe diodes with precise alignment of each shadow mask and resulting device layer as shown in Figure 49. The PbTe layers were deposited following the same procedure outlined in Section 3.2.1 to obtain high quality nanocrystalline films with thicknesses varying between 150 to 700 nm for different device iterations.

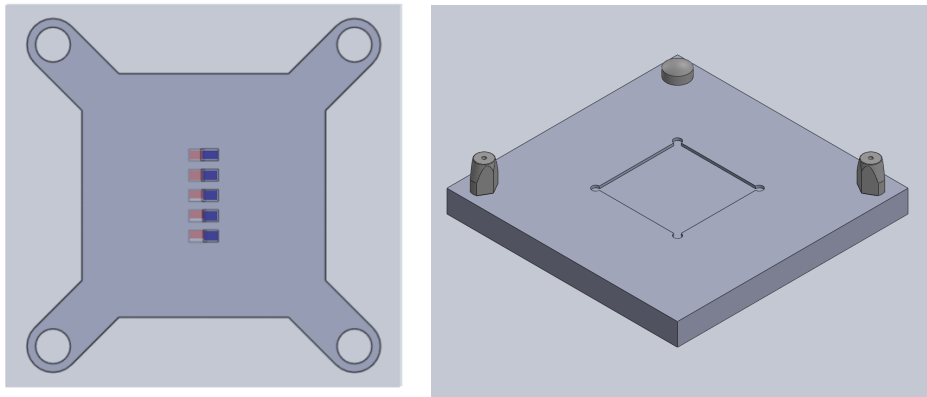


Figure 49. Customized a) shadow mask and b) sample holder designed to achieve consistent and precise alignment of each of the PbTe diode device layers.

### 3.3 PbTe p-n Junction Characterization

Three different device series were fabricated and tested with varying p- and n-type layer thicknesses and carrier concentrations as shown in Table 6. Five diodes with different junction widths ( $D_1 = 200$ ,  $D_2 = 400$ ,  $D_3 = 600$ ,  $D_4 = 800$ , and  $D_5 = 1000 \mu\text{m}$ ) were fabricated within each series and a representative sample is shown in Figure 50. To evaluate the diode behavior of each series, the devices were characterized with dark I-V, photo-induced current transient spectroscopy (PICTS), and responsivity measurements. Based on these results and corresponding simulations, future device designs have been proposed to further improve the PbTe film properties and resulting diode behavior.



Figure 50. Optical microscope image of sample S1D4 with large Sn contacts deposited on top of the p-PbTe and n-PbTe:O thin films on each side of the overlapping junction.

Table 6. Sample descriptions and material parameters (layer thicknesses and carrier concentrations) for the three PbTe diode series characterized in the following section.

Sample Series	Substrate	P-PbTe Layer Thicknesses (nm)	N-PbTe:O Layer Thicknesses (nm)	P-Type Carrier Concentration ( $\text{cm}^{-3}$ )	N-Type Carrier Concentration ( $\text{cm}^{-3}$ )
S1	Oxide on Si	636	415	5E+17	2E+19
S2	Oxide on Si	495	470	5.37E+18	2.89E+19
S6	Fused Silica	663	394	5E+17	5.50E+16

### 3.3.1 Dark I-V Characterization

In a photodiode, current has an exponential dependence on voltage, such that applying a forward bias leads to an increase in current flow while applying a reverse bias reduces and inhibits any current flow. Assuming no illumination of the photodiode, the remaining current in reverse bias is known as the dark current or leakage current as given by Equation 9 where  $n_i$  represents the intrinsic carrier concentration,  $\tau$  represents the minority carrier lifetime, and  $\mu$  represents the minority carrier mobility. The resulting dark I-V curve depends on this saturation current as indicated by Equation 10. Dark I-V measurements were performed for each of the PbTe photodiode series at varying temperatures between 45K to 300K to evaluate this rectifying behavior and confirm the presence of a p-n junction.

$$J_0(T) = n_i^2 \sqrt{\frac{qkT\mu}{\tau}} \left( \frac{1}{n} + \frac{1}{p} \right) \quad (9)$$

$$J(V, T) = J_0 \left( e^{\frac{qV}{kT}} - 1 \right) \quad (10)$$

The experimental dark I-V results for Series 1 Diode 3 (S1D3 with 600  $\mu\text{m}$  junction width) are shown in Figure 51a for a voltage bias swept from negative to positive 3 V. At the highest measurement temperature of 200K, there is no significant rectifying behavior and the I-V curve demonstrates an ohmic, linear response. Since PbTe has a very small bandgap suited for absorption of mid-infrared wavelengths, there is significant thermal generation of carriers near room temperature that obscure the diode response. As the temperature decreases below 150K and the

generation of thermal carriers is reduced, the diode response becomes more clear as evidenced by the asymmetric I-V curves with lower current in reverse bias. This rectifying behavior is even more apparent when considering the resistance (calculated from  $R = dV/dI$ ) as a function of applied voltage in Figure 51b which demonstrates a clear decrease in resistance in forward bias.

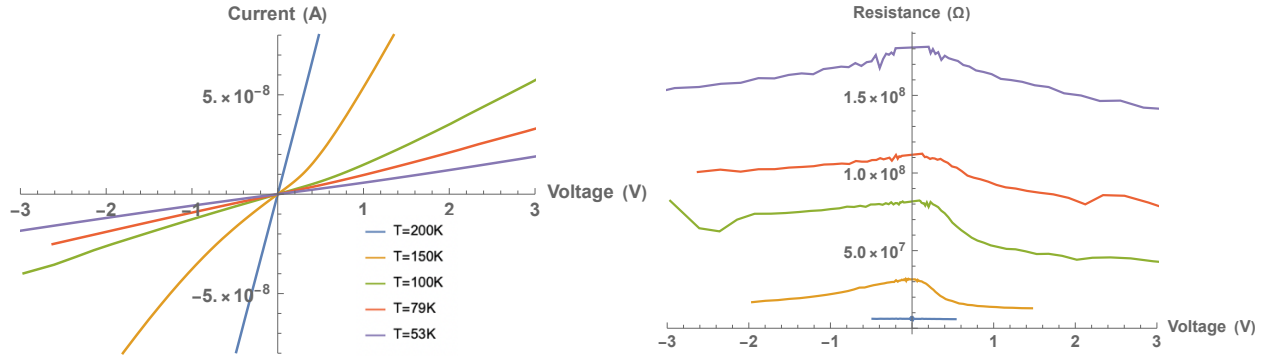


Figure 51. a) Dark I-V and b) R-V curves of sample S1D3 measured at various temperatures between 200 K to 53 K. At low temperatures (green = 100 K, red = 79 K, purple = 53 K), a rectifying diode response is observed as clearly shown by the higher resistance in reverse bias compared to forward bias.

The high resistance for these measurements results from the added series resistance of the p- and n-type film regions on either side of the junction. The device resistance also increases with decreasing temperature since the thin film resistance increases exponentially as indicated by Equation 11 where  $\Delta E_A$  is the activation energy [30-31]. The individual p- and n-type resistance was measured as a function of temperature to extract the activation energy from the linear slope as shown in Figure 52. The sharp change in slope has previously been reported in PbTe thin films and suggests that more than one conduction mechanism is involved. The lower activation energy of approximately 0.03 eV at low temperatures likely results from ionized Pb vacancy acceptor defects, while the larger activation energy of 0.1 eV at higher temperatures can be attributed to Te interstitials [30]. Similar measurements were performed for n-PbTe:O thin films to extract an activation energy between 0.5 to 0.1 eV depending on the film thickness and temperature range.

$$\rho(T) = \rho_0 \exp\left(-\frac{\Delta E_A}{kT}\right) \quad (11)$$

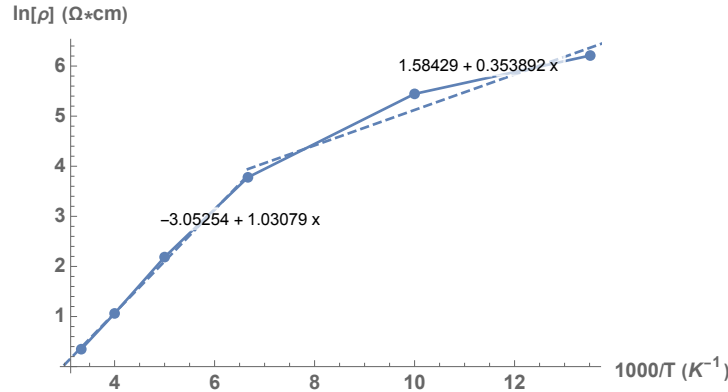


Figure 52. Resistivity as a function of temperature for a 636 nm p-PbTe thin film on  $\text{SiO}_2$  substrate. The linear slope of the Arrhenius-type plot corresponds to the activation energy for conduction, and the distinct break in the linear slope indicates the presence of two different conduction mechanisms.

The experimental activation energies for p- and n-type resistivity were applied to theoretical simulations to confirm the diode behavior in series with two resistors as shown in Figure 53. The theoretical simulations represented by the dashed lines closely match the experimental results for S1D3 as well as S1D2 (small junction width = 400  $\mu\text{m}$ ). These experimental results comparing S1D3 and S1D2 also confirm the expected increase in forward bias current with larger diode area at a fixed temperature as demonstrated by the increasing signal from i) S1D2 75K (red) to S1D3 79K (yellow) and ii) S1D2 40K (purple) to S1D3 53K (green). All of these trends confirm the presence of a PbTe p-n junction with the expected behavior that follows the governing equations for dark I-V measurements of a diode.

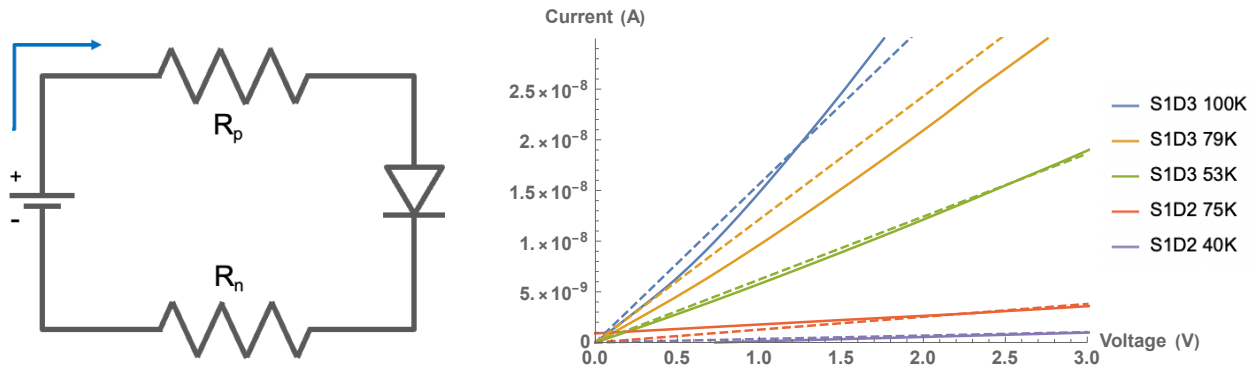


Figure 53. a) Representative circuit of the p-n junction diodes in series with p- and n-type resistors ( $R_p$  and  $R_n$ ). b) Theoretical I-V curves (dashed lines) for the circuit model in (a) closely

match the experimental results for the diode I-V curves (solid lines) at various temperatures closely match the by accounting for the temperature-dependence of  $R_p$ ,  $R_n$ , and the p-n junction.

### 3.3.2 PICTS Characterization

Photo-induced current transient spectroscopy measurements (PICTS) were performed to further evaluate the PbTe p-n junctions and investigate any potential mid-gap carrier traps within the diodes. PICTS offers several advantages for defect characterization compared to other conventional capacitance-based defect measurement techniques such as deep-level transient spectroscopy (DLTS) and thermal admittance spectroscopy (TAS). In particular, PICTS is well-suited for studying defects in low-mobility semiconductor materials like PbTe. Unlike capacitance-based methods, PICTS is less affected by mobile ions and slow traps, providing more accurate defect characterization. Additionally, PICTS can detect both majority and minority carrier traps, offering a comprehensive view of defect landscapes. The technique also allows for the determination of defect activation energies and capture cross-sections, providing valuable insights into the nature and behavior of traps in these materials [32].

PICTS was specifically chosen for characterizing these PbTe p-n junction diodes since PbTe is a narrow-bandgap semiconductor with relatively low mobility, making it challenging to analyze using conventional techniques. Furthermore, as a p-n junction diode, the device structure may introduce complexities that could interfere with capacitance-based measurements. PICTS' reduced sensitivity to these factors would allow for more accurate defect characterization of both majority and minority carrier traps, which would be particularly useful in a p-n junction device. Lastly, the detailed information on defect activation energies and capture cross-sections provided by PICTS could offer valuable insights into the performance and limitations of the PbTe p-n junction diode, potentially guiding improvements in device design and fabrication.

PICTS measurements were performed for several diodes by measuring the photocurrent transients under a fixed voltage bias (typically 0 V) and pulsed illumination. Upon illumination from a narrow-band light-emitting diode (LED) source with photon energy greater than that of PbTe ( $\frac{hc}{\lambda_{LED}} > E_g_{PbTe}$ ), photocarriers were generated within the diode with some fraction captured in defect states. After a sufficient illumination pulse duration, the diode reached a steady state with a

constant photocurrent and density of charge carriers within each available energy or defect level. Once the light source was removed, the free charge carriers quickly recombined or drifted out of the device leading to a sharp decrease in the signal. On the other hand, charge carriers within the mid-gap defect levels were thermally re-emitted on a much longer timescale. The decay rate of the current transient resulting from carrier emission from a defect state is given by Equation 12 where K is a constant derived from the material and device parameters and  $e_i$  is the emission rate of the given defect level. The emission rate is determined by the energy depth of the defect state as shown by Equation 13 where  $v_{th}$  is the carrier thermal velocity,  $N_{eff}$  is the effective density of states, T is the absolute temperature, and  $\sigma_i$  and  $E_i$  represent the capture cross section and energy depth of the defect state, respectively.

$$I(t) = Ke_i \exp(-e_i t) \quad (12)$$

$$e_i = \frac{\ln(t_1/t_2)}{t_1 - t_2} = \sigma_i v_{th} N_{eff} \exp\left(-\frac{E_i}{k_B T}\right) \quad (13)$$

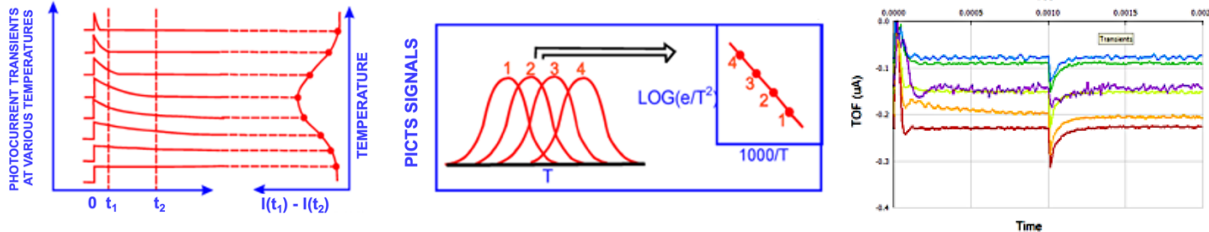


Figure 54. a) Theoretical PICTS measurement results that b) demonstrate a peak position shift with temperature for different rate windows (e) and can be used to extract the defect energy level from the resulting Arrhenius plot. c) Experimental demonstration of the photoinduced current transients for a PbTe p-n junction diode.

Since the carrier emission from defect states is a thermally activated process, the current transients were measured as a function of temperature from approximately 300K down to 20K to determine the energy depths ( $E_i$ ) of any defect states. The PICTS spectra for diode S1D2 are shown in Figures 55a-b for varying illumination wavelengths and voltage bias. Both spectra demonstrate two peaks, one at a high temperature around 250K and one at a low temperature around 45K. Based on these results, the temperature of the photo-induced current peak was extracted for each emission rate window. This data was then analyzed in accordance with Equation 13 to obtain an Arrhenius plot of the quantity  $\ln(T^2/e_i(T))$  as a function of inverse temperature. The  $T^2$  pre-factor accounts for

the temperature dependence of  $v_{\text{th}}$  and  $N_{\text{eff}}$  in Equation 13. The resulting linear relationship confirms that the photoinduced current transients result from thermally activated defect-level emptying. Additionally, the energy depths ( $E_i$ ) and carrier capture cross-sections ( $\sigma_i$ ) for each peak can be extracted from the linear best-fit slope and intercept, respectively. The  $v_{\text{th}}$  and  $N_{\text{eff}}$  were calculated according to Equations 14-15 where  $m_c$  and  $m_d$  represent the conductivity effective mass and the density-of-states effective mass for the relevant band. These parameters were extracted for different temperatures from previous works as presented in Table 7 where  $m_e$  is the free electron effective mass [33].

$$v_{\text{th}} = \sqrt{3k_B T / m_c} \quad (14)$$

$$N_{\text{eff}} = 2 \left( \frac{2\pi m_d k_B T}{h^2} \right)^{3/2} \quad (15)$$

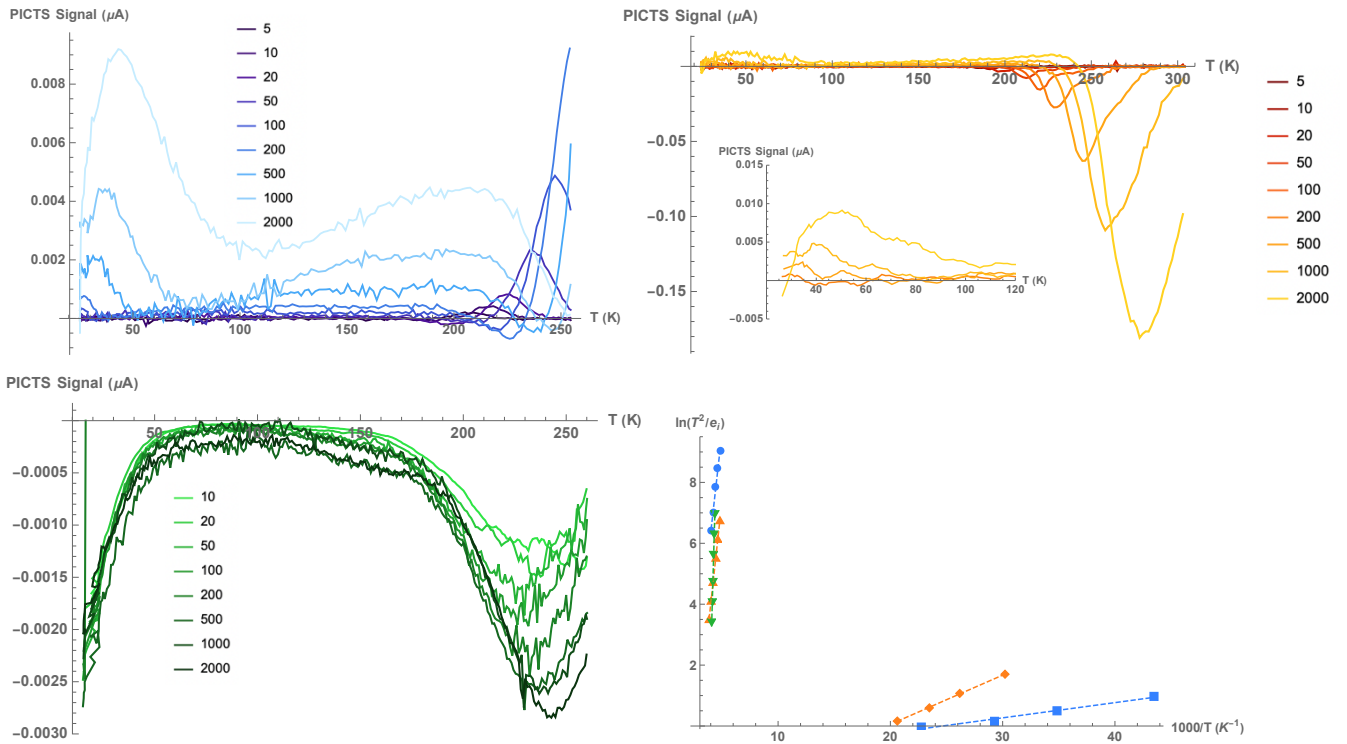


Figure 55. PICTS spectrum of a) S1D2 at 0 V bias, b) S1D2 at -5 V bias, and c) S6D5 at 0 V bias for emission rate windows between 5 to 2000 Hz. d) Arrhenius plot of the emission rate peaks extracted from the PICTS spectra where the blue and orange lines correspond to the

measurements of S1D2 at 0 and -5 V bias, respectively, and the green line corresponds to the peak of S6D5 in (c).

Table 7. Calculation parameters for the p- and n-type conductivity effective mass ( $m_c$ ) and the density-of-states effective ( $m_d$ ) for both low and high temperature PICTS peaks.

Effective Mass Parameter	45 K	250K
$m_{c,n}/m_e$	0.05	0.1
$m_{d,n}/m_e$	0.2	0.35
$m_{c,p}/m_e$	0.045	0.01
$m_{d,p}/m_e$	0.15	0.27

The resulting defect parameters are presented in Table 8 for all samples. The small capture cross sections (less than  $10^{-17} \text{ cm}^2$ ) for all of the defect states in S1D2 suggest a coulombically repulsive character of these defects. Additionally, since the capture carrier cross sections are approximately equal magnitude for both majority and minority carriers, this indicates that these defect levels correspond to recombination centers. Alternatively, if the capture cross section varied significantly for each carrier type, this would suggest the presence of a majority or minority carrier trap for defects with larger majority or minority carrier cross sections, respectively. Finally, since the energy levels are very shallow and located close to the conduction and valence bands, these defects likely correspond to dopant-like impurities rather than more complex defects or impurities.

Table 8. Defect parameters, including the defect energy levels ( $E_i$ ) and capture cross sections ( $\sigma_{c,i,n}$  and  $\sigma_{c,i,p}$ ), extracted from the Arrhenius-type plot in Figure 55d.

Sample	$E_i$	$\sigma_{c,i,n} [\text{cm}^2]$	$\sigma_{c,i,p} [\text{cm}^2]$
S1D2 @ 0V	0.282651	$4.116 * 10^{-19}$	$1.921 * 10^{-19}$
	0.004304	$2.632 * 10^{-21}$	$3.845 * 10^{-21}$
S1D2 @ -5V	0.291484	$1.125 * 10^{-20}$	$5.250 * 10^{-21}$
	0.013920	$1.061 * 10^{-17}$	$1.549 * 10^{-17}$
S6D5	1.110210	1.19873	0.559471

While the PICTS spectrum from S6D5 in Figure 55c exhibited a strong peak around 250 K that demonstrated a thermally-activated behavior as indicated by the strong linear fit in Figure 55d, the interpretation of this data proved more difficult. The resulting analysis led to a large energy level around 1.11 eV and a capture carrier cross section on the order of  $1 \text{ cm}^2$ , which is unphysically

large. This inaccuracy likely results from a distortion of the PICTS spectra due to temperature variations of the mobility-lifetime product [32]. As such, this measurement and the extracted defect values are not reliable, and the observed defect level may result from a lifetime and/or temperature-dependent effect.

### 3.3.3 Responsivity Measurements

In order to evaluate the photoresponse of the PbTe photodiodes, responsivity measurements were performed as described in Section 3.2.1 at 77K for a spectral range from 2 to 7  $\mu\text{m}$ . Figure 56a illustrates the photovoltaic response (with no external applied bias) of the S1D1 diode for the blue and yellow spectra. As the illumination increased by increasing the slit size from 1.0 mm (blue) to 1.5 mm (yellow), the photovoltaic sensitivity signal improved as expected from approximately 14 to 22 V/W at a peak wavelength of  $\sim 3.7 \mu\text{m}$ . To further confirm the diode response, a small forward bias of +100 nA was applied and demonstrated no significant change in the resulting spectrum (as demonstrated by comparing the yellow to green spectra; the small increase at shorter wavelengths can be disregarded as this is likely due to thermionic emission from the Sn contact). Alternatively, when a small reverse bias of -100 nA was applied and achieved a significant increase in the signal by a factor of two, demonstrating a strong sensitivity of approximately 42 V/W at 3.7  $\mu\text{m}$  wavelength. This nonlinear response to a small forward and reverse bias and drop in sensitivity near the expected bandedge wavelength further confirm the presence of a mid-infrared PbTe p-n junction in these devices.

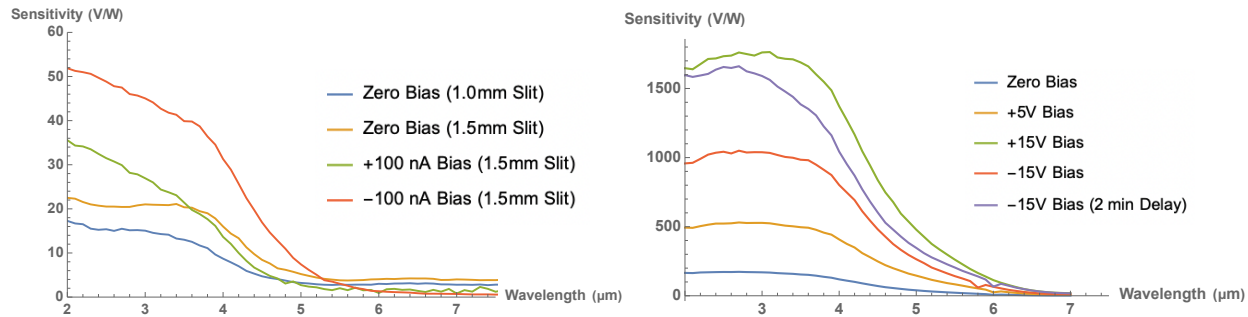


Figure 56. a) Responsivity spectra for sample S1D1 under varying bias and illumination (slit size). The strong photovoltaic signal under zero bias (blue and yellow) confirms the photovoltaic behavior of the PbTe diodes with the expected nonlinear, rectifying behavior that demonstrates an amplified response in reverse (red) compared to forward (green) bias. b) S6D4 Responsivity.

### 3.3.4 SEM & AFM Characterization

As described in Section 3.3.1, all of the initial PbTe diodes with the horizontal design demonstrated very high series resistance due to the large p- and n-type film regions on either side of the junction. In order to eliminate these series resistance contributions and isolate the diode behavior with lower dark current in future devices, a traditional vertical circular diode structure was proposed as shown in Figure 57. These devices utilize an underlying Sn contact to the n-type layer and a top Sn contact to the p-type layer. The diode radius was varied between 0.5 to 5 mm with the top Sn contact radius 100  $\mu\text{m}$  smaller than that of the diode. These devices were fabricated using the same PVD and shadow mask techniques for the patterning the PbTe films with thicknesses varying from approximately 100 to 700 nm for different samples.

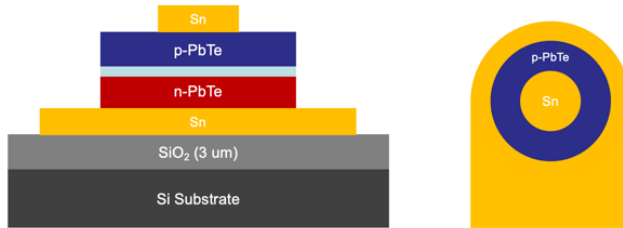


Figure 57. a) Cross-sectional and b) top view of a vertical stacked circular diode design that would reduce the parasitic series resistance compared to the horizontal diode design.

Unfortunately, the dark I-V measurements for all of these vertical stacked diodes demonstrated shunting through the semiconductor layers with no observable rectifying behavior or photoresponse. Further investigation through scanning electron microscopy (SEM) revealed that both p-PbTe and n-PbTe:O thin films suffer from considerable cracking across the entire surface area. The dimensions of these defects are approximately constant for both p- and n-type films and independent of the film thickness (measured for 660 nm and 300 nm thick films). The crack dimensions are approximately 10 nm wide and 200 to 400 nm long with a density of roughly 0.3 cracks per  $\mu\text{m}^2$ . It is likely that these cracks within the PbTe thin films provided short-circuit leakage pathways through the diode enabling direct contact of the two Sn layers on either side of the junction.

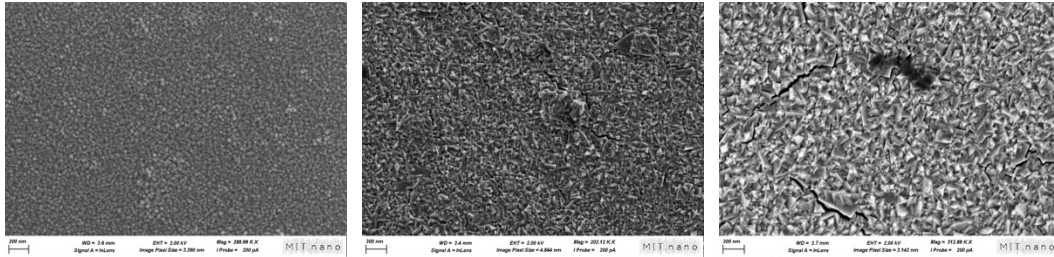


Figure 58. SEM images of a) a 400nm n-PbTe:O on  $\text{SiO}_2$  substrate, b) a 660nm p-PbTe on  $\text{SiO}_2$  substrate, and c) a 660nm p-PbTe on  $\text{BaF}_2$  substrate that all demonstrate cracks in various locations across the film.

This cracking behavior was suspected to result from thin film stress as there is a considerable thermal expansion coefficient mismatch between the PbTe material ( $\alpha_{\text{PbTe}} = 20 * 10^{-6} \text{ K}^{-1}$ ;  $\alpha_{\text{SiO}_2} = 0.5 * 10^{-6} \text{ K}^{-1}$ ). In an attempt to reduce any potential thin film stress and thus eliminate any crack propagation, PbTe films were deposited onto a  $\text{BaF}_2$  substrate that was chosen due to its comparable thermal expansion coefficient ( $\alpha_{\text{BaF}_2} = 18 * 10^{-6} \text{ K}^{-1}$ ) and lattice parameter to PbTe ( $a_{\text{PbTe}} = 6.460 \text{ \AA}$ ;  $a_{\text{BaF}_2} = 6.196 \text{ \AA}$ ). SEM imaging revealed the same cracking behavior for PbTe films on the  $\text{BaF}_2$  substrate and suggests that these defects do not result from any substrate-induced film stress.

### 3.4 Improved Carrier Concentration Control with n-type $\text{Pb}_{(1-x)}\text{Bi}_x\text{Te}$

While the PbTe thin film morphology currently inhibits the fabrication of stacked, vertical diodes with low series resistance, the overall device resistance and dark current could also be reduced by increasing the PbTe carrier concentration as indicated by Equation 9. Since the PbTe responsivity is inversely related to the carrier concentration, this work focused on increasing the n-type carrier concentration while maintaining a lower p-type carrier concentration to maintain high absorption and efficient photocarrier generation in the top layer of the device. Additionally, while the as-deposited PbTe demonstrated consistent carrier concentrations across all depositions with no variation over time, the n-type carrier concentration of the PbTe:O films was more variable between depositions and slowly decayed over time towards an intrinsic behavior. This inconsistent composition and time-dependent behavior is attributed to the variable incorporation of oxygen both during the deposition and after fabrication that is difficult to control due to its high volatility

and inevitable atmospheric exposure. As such,  $\text{Bi}_2\text{Te}_3$  was investigated as an alternative n-type dopant to achieve higher carrier concentrations with more consistency and stability.

The  $\text{Pb}_{(1-x)}\text{Bi}_{(x)}\text{Te}$  thin films were deposited using the same PVD technique and deposition parameters described in Section 3.2.1. Four different samples were fabricated and tested with varying concentrations between 2 to 10 atomic percent Bi incorporated by adding the appropriate quantity of  $\text{Bi}_2\text{Te}_3$  to the PbTe source material. All of the films were deposited onto  $\text{BaF}_2$  substrates with thicknesses around 400 nm. The electrical, structural, and optical material properties were analyzed using Hall Effect, X-ray diffraction (XRD), and responsivity measurements, respectively, as described in the following sections.

### 3.4.1 Hall Effect Characterization

Figure 59 plots the n-type majority carrier concentration and resistivity of all four  $\text{Pb}_{(1-x)}\text{Bi}_{(x)}\text{Te}$  samples as a function of Bi concentration. The carrier concentration increases linearly with Bi concentration and thus confirms that Bi functions as a donor in PbTe due to its extra valence electron compared to Pb ( $n \propto N_{D,\text{Bi}}$ ). All of the  $\text{Pb}_{(1-x)}\text{Bi}_{(x)}\text{Te}$  demonstrates strong n-type behavior with a high carrier concentration of approximately  $1.4\text{E}+20 \text{ cm}^{-3}$  for the 10% Bi sample. This significant increase in n-type carrier concentration by an order of magnitude compared to that of the PbTe:O films also leads to a reduction in resistivity that will help to reduce the PbTe diode dark current and improve the device performance. In addition to improved carrier concentration and resistivity, the  $\text{Pb}_{(1-x)}\text{Bi}_{(x)}\text{Te}$  films also demonstrated more consistent properties between different depositions with stable carrier concentrations when re-measured after two days in atmosphere. All of these improvements of the n-type  $\text{Pb}_{(1-x)}\text{Bi}_{(x)}\text{Te}$  films compared to the PbTe:O films will enable the design and fabrication of PbTe diodes with precisely controlled carrier properties and minimal series resistance contributions.

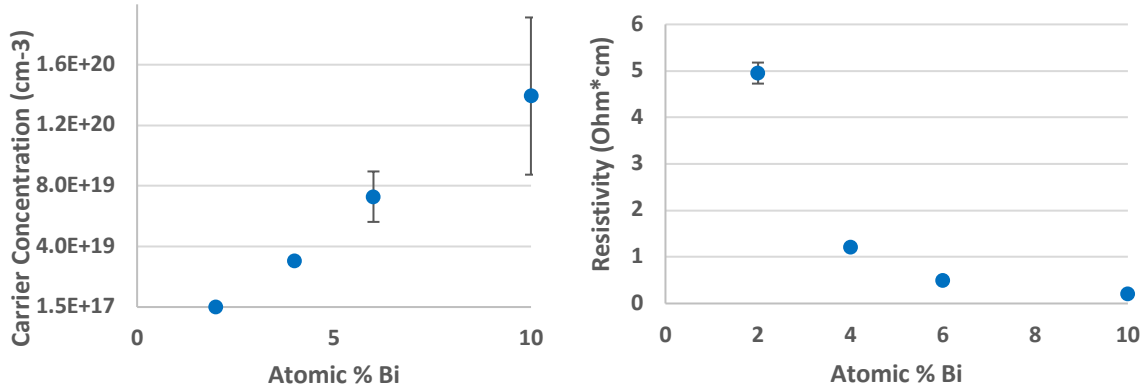


Figure 59. Measured a) majority carrier concentrations and b) mobility in n-type  $\text{Pb}_{(1-x)}\text{Bi}_{(x)}\text{Te}$  films as a function of Bi concentration.

### 3.4.2 XRD Characterization

In addition to the electrical properties of the  $\text{Pb}_{(1-x)}\text{Bi}_{(x)}\text{Te}$  films, the material quality and composition was analyzed through XRD, SEM, and AFM. The linear XRD plots are shown in Figures \_\_ and all of the peaks for each of the four samples match those of a  $\text{Pb}_{(1-x)}\text{Bi}_{(x)}\text{Te}$  alloy, confirming that the polycrystalline thin films are composed of a single phase of  $\text{Pb}_{(1-x)}\text{Bi}_{(x)}\text{Te}$ . All four samples demonstrate a preferred (200) orientation as indicated by the high intensity peak around  $26\text{}\square20$ . Further analysis of the XRD spectra confirm that the lattice parameter ( $a$ ) of the  $\text{Pb}_{(1-x)}\text{Bi}_{(x)}\text{Te}$  alloys follows Vegard's law as shown in Equation 16. This analysis confirms the correct stoichiometry of the resulting  $\text{Pb}_{(1-x)}\text{Bi}_{(x)}\text{Te}$  thin films that matches the composition of the mixed source material.

$$a_{\text{Pb}_{(1-x)}\text{Bi}_{(x)}\text{Te}} = (1 - x)a_{\text{PbTe}} + x a_{\text{Bi}_2\text{Te}_3} \quad (16)$$

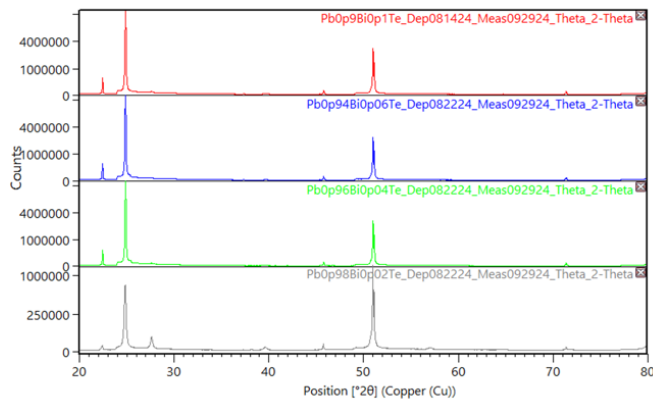


Figure 60. XRD spectra for four different concentrations of n-type  $\text{Pb}_{(1-x)}\text{Bi}_{(x)}\text{Te}$  films demonstrate high crystallinity with a preferred (200) crystallographic growth direction.

Table 9. Expected lattice parameters calculated from Vegard's law for varying  $\text{Pb}_{(1-x)}\text{Bi}_{(x)}\text{Te}$  film compositions compared to the experimentally-measured lattice parameters from XRD analysis.

Expected At% Bi	Expected Lattice Parameter (A)	Measured Lattice Parameter from XRD (A)
2	6.4184	
4	6.3768	
6	6.3352	
10	6.252	

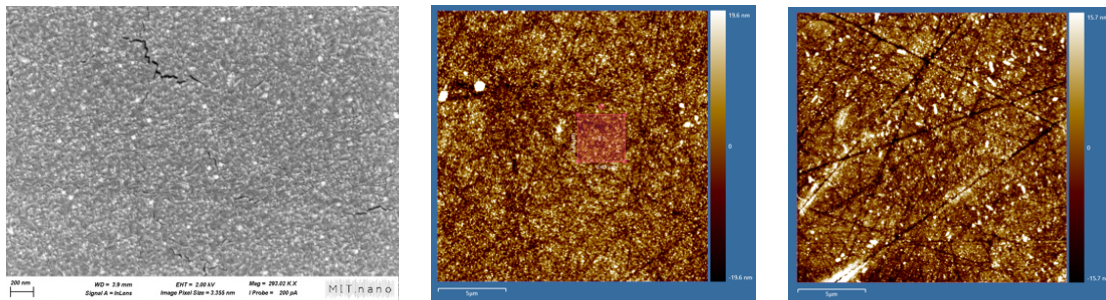


Figure 61. a) SEM image of  $\text{Pb}_{0.9}\text{Bi}_{0.1}\text{Te}$  on  $\text{BaF}_2$  substrate. b) AFM scan results for a  $\text{Pb}_{0.98}\text{Bi}_{0.02}\text{Te}$  film on  $\text{BaF}_2$  substrate with average roughness =  $7.39 \pm 9.82\text{nm}$ . c) AFM scan results for a  $\text{Pb}_{0.9}\text{Bi}_{0.1}\text{Te}$  film on  $\text{BaF}_2$  substrate with Average Roughness =  $5.80 \pm 7.84\text{nm}$ .

### 3.4.3 Photoconductivity Measurements

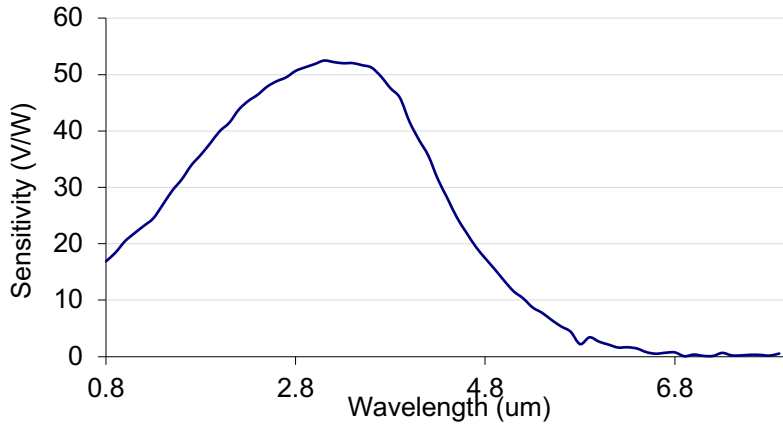


Figure 62. Responsivity spectrum under 1 mA constant current bias for a 200 nm thick  $\text{Pb}_{0.98}\text{Bi}_{0.02}\text{Te}$  film on  $\text{BaF}_2$  substrate with a carrier concentration of  $n = 2.7\text{E}+17 \text{ cm}^{-3}$ .

## 4 Nonlinear Properties of ZnTe Thin Films for PICs

### 4.1 Introduction

As optical communication technologies continue to advance and progress, the demand for optical signal-processing devices continues to increase. Nonlinear materials have attracted significant interest as they are essential to the development of these all-optical systems. More specifically, nonlinear materials enable on-chip many different optical manipulation functions such as modifying the phase, polarization state, and intensity of incoming signals as well as generating new frequencies and more.

Several different materials have been investigated as nonlinear materials for C-Band applications, most notably Si,  $\text{LiNbO}_3$ , and III-V materials such as GaAs and InP. Si has been widely studied for nonlinear applications due to its CMOS compatibility and thus simple fabrication and integration with existing photonic integrated circuit technologies. However, the nonlinear switching operations in Si occur due to dominant free carrier nonlinearities excited via two-photon absorption (TPA), which limits the response time to the free carrier lifetime (on the order of nanoseconds) and increases the optical losses. Alternatively,  $\text{LiNbO}_3$  has a much faster response time on the order of femtoseconds to picoseconds as the nonlinearities in this material occur due

to electronic polarization and ionic displacement effects [34]. LiNbO<sub>3</sub> also demonstrates high temperature, chemical, and mechanical stability that would enable device operation in many different environments. Unfortunately, LiNbO<sub>3</sub> suffers from significant fabrication and integration challenges as it requires a wafer bonding process that is slow and expensive and limits the scalability of this technology to larger 200 mm wafers. Finally, III-V materials have generated interest as nonlinear materials as they possess high linear refractive indices in addition to large nonlinear coefficients that consequently achieve high optical confinement and smaller device footprints. Similar to LiNbO<sub>3</sub>, these materials are very brittle and fragile and require complex wafer bonding processes for integration due to their large lattice mismatch with traditional Si substrates. While each of these materials has certain advantages, there are still limitations to these technologies and thus potential for a new material that could eliminate any fabrication and integration challenges while still demonstrating strong nonlinear properties with high frequency and high-speed capabilities.

#### 4.2 ZnTe Material Characterization

Zinc telluride (ZnTe) is a semiconductor material with exceptional nonlinear properties including considerable Pockels and Kerr coefficients as shown in Table 10. Due to its larger bandgap compared to Si and III-V materials, ZnTe has negligible TPA and consequently lower optical losses for high-power nonlinear applications. The large linear refractive index also ensures strong optical confinement to develop compact devices. Additionally, the nonlinear response time in ZnTe is not limited by the free carrier lifetime and can achieve high-speed modulation.

Table 10. Material parameters for common infrared nonlinear optical materials.

Materials	Bandgap (eV)	Refractive Index, n <sub>0</sub>	Pockels Coefficient, n <sub>1</sub> (pm/V)	Kerr Coefficient, n <sub>2</sub> (cm <sup>2</sup> /W)	d <sub>n0</sub> /dT (1/K)	$\beta$ (cm/GW) at NIR	Dielectric Constant, $\epsilon_1$
LiNbO <sub>3</sub>	3.7	2.21	30	3.8x10 <sup>-15</sup>	4.5x10 <sup>-5</sup>	0	4.8
GaAs	1.43	3.3	94	1x10 <sup>-13</sup>	23x10 <sup>-5</sup>	8 to 30	10
InP	1.34	3.17	26	1x10 <sup>-13</sup>	20x10 <sup>-5</sup>	15	10
Si	1.14	3.48	0	4.2x10 <sup>-14</sup>	20x10 <sup>-5</sup>	1 to 10	11.7
MgF <sub>2</sub>	10.8	1.38	-	2.4x10 <sup>-14</sup>	3x10 <sup>-5</sup>	0	1.9
SiN	5.0	2.05	-	*2.4x10 <sup>-15</sup>	**2.2x10 <sup>-5</sup>	0	10
ZnTe	2.26	2.86	4.3	8x10 <sup>-13</sup>	5x10 <sup>-5</sup>	0	7.5

ZnTe is also an attractive material for integrated nonlinear optics applications due to its cubic zincblende structure ( $\bar{4}3m$  space group). As a result of this zincblende crystal structure, the electro-optic coefficients in the tensor matrix are all of equal magnitude as shown in Figure 63a where  $r_{41} \sim 4.45 \text{ pm/V}$ . This is very beneficial as ZnTe consequently has no linear birefringence ( $n_x = n_y = n_z = n_0$ ) and demonstrates nonlinear effects of equal magnitude for several different crystal orientations, which would simplify future device fabrication and enable integration on a variety of substrates with different preferred crystallographic growth directions. In contrast, LiNbO<sub>3</sub> has a trigonal crystal structure (3m space group), where the electro-optic coefficients vary significantly throughout the matrix as shown in Figure 63b where  $r_{33} \sim 30 \text{ pm/V} \gg r_{13,22,51}$ . This leads to large linear birefringence and variations in the nonlinear properties of LiNbO<sub>3</sub> crystals along different crystallographic axes and requires precise growth and alignment techniques to successfully fabricate high performance devices.

Cubic ( $\bar{4}3m$ ):

$$\begin{bmatrix} 0 & 0 & 0 \\ 0 & 0 & 0 \\ 0 & 0 & 0 \\ r_{41} & 0 & 0 \\ 0 & r_{41} & 0 \\ 0 & 0 & r_{41} \end{bmatrix}$$

Trigonal (3m):

$$\begin{bmatrix} 0 & -r_{22} & r_{13} \\ 0 & r_{22} & r_{13} \\ 0 & 0 & r_{33} \\ 0 & r_{51} & 0 \\ r_{51} & 0 & 0 \\ 0 & 0 & 0 \end{bmatrix}$$

Figure 63. Tensor matrices for the electro-optic coefficients of materials with a) cubic and b) trigonal crystal structures.

Recent innovations have enabled epitaxial growth of ZnTe by atomic layer deposition (ALD) at low temperatures, which will facilitate the direct growth (monolithic integration) of ZnTe on CMOS circuitry and circumvent the current complexities of wafer bonding technique associated with InP and GaAs-based PICs [36-37]. This novel ALD method also enables the fabrication of conformal layers with very high aspect ratios when compared to other growth techniques such as sputtering and chemical vapor deposition (CVD) as shown in Figure 64a. As a result, this technique can be leveraged to produce unique structures and high efficiency electro-optic devices with CMOS-compatible back-end-of-line (BEOL) ZnTe films.

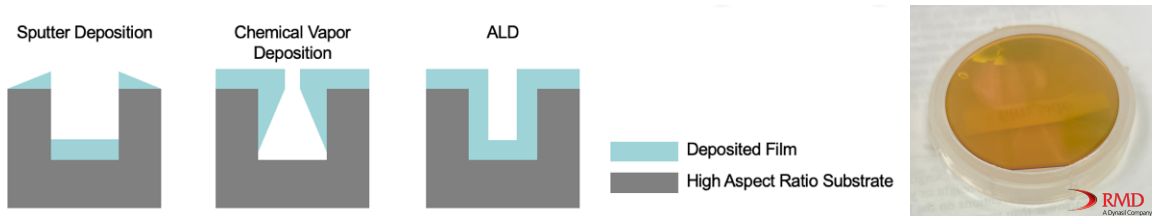


Figure 64. a) Comparison of thin film morphologies deposited on high aspect ratio substrates via sputtering, CVD, and ALD. b) Sample of 165 nm ALD-grown ZnTe film on  $\text{Al}_2\text{O}_3$  substrate.

Since nonlinear electro-optic devices are very sensitive to crystalline defects, x-ray diffraction (XRD) was performed for 165nm ZnTe ALD films on  $\text{Al}_2\text{O}_3$  and Si substrates to evaluate the crystallographic quality. Bulk ZnTe has a much larger lattice parameter of  $a_{\text{ZnTe}} = 6.101 \text{ \AA}$  compared to those of the  $\text{Al}_2\text{O}_3$  and Si substrates ( $a_{\text{Al}_2\text{O}_3} = 4.758 \text{ \AA}$  and  $a_{\text{Si}} = 5.4298 \text{ \AA}$ ), so this lattice mismatch could cause the formation of misfit dislocations at the interface to accommodate the strain energy within ZnTe films greater than the critical layer thickness ( $h_c$ ). As such, it is necessary to evaluate the crystallographic quality and ensure that the ZnTe film is under the critical layer thickness to prevent the formation of parasitic misfit dislocations that would introduce roughness and scattering centers at the interface and consequently reduce the electro-optic efficiency and increase the optical propagation losses.

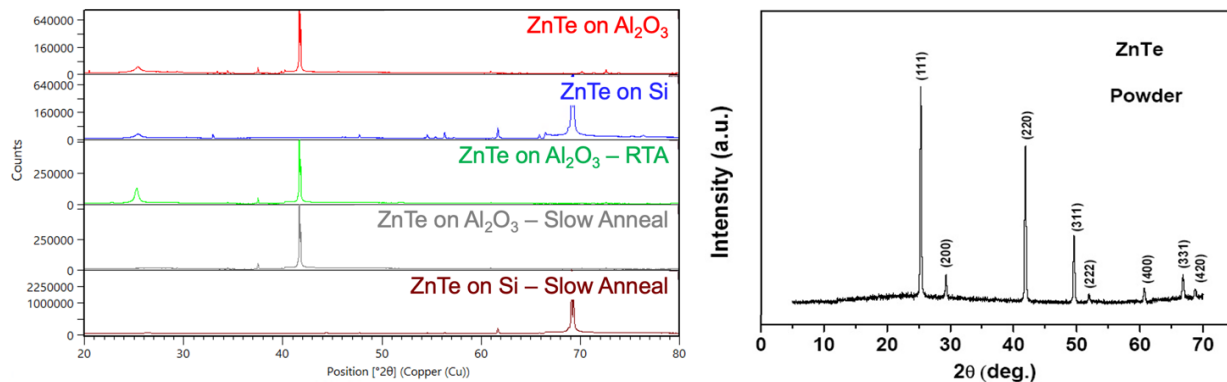


Figure 65. XRD spectra of 165 nm thick ALD-grown ZnTe on various substrates with different post-deposition processing compared to a representative ZnTe powder XRD scan.

Figures 65a and b illustrate the XRD measurement results for  $\text{Al}_2\text{O}_3$  and Si substrates, respectively, that indicate a change in the preferred crystallographic growth direction from (220) to (420) for the different substrates. The sharp peak shapes for both measurements indicate high crystallinity, and further analysis of

the peak positions reveals the unit cell lattice parameters of the thin films as shown in Table 11. According to Equation 17 where  $a_s$  and  $a_f$  are the substrate and film lattice parameters, respectively, the ZnTe films demonstrate compressive misfit strains of 22.3% on Al<sub>2</sub>O<sub>3</sub> and 10.5% on Si. As this film stress is fairly high, it is likely that there are some defects at the interface that could increase optical losses in future devices.

$$\varepsilon_{mf} = \frac{a_s - a_f}{a_f} \quad (17)$$

Table 11. Experimental lattice parameters, grain size, and misfit strains extracted from the XRD measurements of 165 nm thick ALD-grown ZnTe films on various substrates.

Substrate	Lattice Parameter (Å)	Grain Size (nm)	Experimental Misfit Strain (%)	AFM Roughness (nm)
Al <sub>2</sub> O <sub>3</sub>	6.124	154.28	-22.3085	
Al <sub>2</sub> O <sub>3</sub> - RTA	6.124	154.29	-22.3109	
Al <sub>2</sub> O <sub>3</sub> - Slow Anneal	6.124	154.29	-22.3110	
Si	6.066	322.28	-10.5813	
Si - Slow Anneal	6.072	322.81	-10.4809	

#### 4.3 ZnTe Hybrid Waveguide Design

This work leverages the novel ZnTe ALD technique to successfully design and fabricate two different hybrid ZnTe single-mode waveguides with i) a Si core (ZnTe-on-Si) and ii) a SiN core (ZnTe-on-SiN) demonstrating significant nonlinear properties in the near-infrared regime. To facilitate accurate design and fabrication of these hybrid waveguide systems for single-mode operation at a central wavelength ( $\lambda_0$ ) of 1565 nm, the optical properties of an ALD-grown ZnTe thin film on Si substrate were characterized via ellipsometry (Semilab SE-2000 Spectroscopic Ellipsometer). Figures 66a-b confirms a linear refractive index ( $n_0$ ) of 2.72 and a negligible extinction coefficient ( $k \sim 0$ ) at  $\lambda_0 = 1565$  nm.

Based on these experimental ellipsometry results of the linear refractive index, the hybrid ZnTe waveguide designs were simulated in Lumerical MODE, with a cross-sectional schematic of the waveguide shown in Figure 67a. In order to maximize the nonlinear contributions of the ZnTe coating, the optical mode confinement within the ZnTe layer was maximized as indicated by classical perturbation theory. As shown by Equation 18, the overall waveguide effective index modulation derived from classical perturbation theory is a sum of the contributions from each electro-optic (EO) material, where the numerator accounts

for the nonlinear effects on the electric field confined within the given EO material divided by the integration of the optical mode over the entire waveguide cross-section.

$$\Delta n_{\text{eff}} = \sum_{\text{EO}} \frac{n_{\text{EO}} c_0 \epsilon_0 \iint_{\text{EO}} \Delta n_{\text{EO}} |E|^2 dx dy}{\iint_{\text{EO}} \text{Re}(E \times H^*) \cdot \hat{z} \cdot dx dy} \quad (18)$$

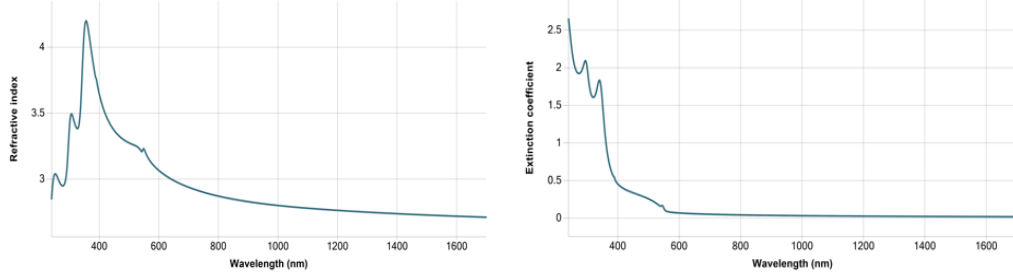


Figure 66. Ellipsometry results for the (a) linear refractive index and (b) extinction coefficient of a 165 nm thick ZnTe film on a silicon substrate.

Therefore, to increase the refractive index modulation and nonlinear contributions from the ZnTe coating for the propagating signals, the electric field confinement within the ZnTe was maximized by varying the Si and SiN waveguide core widths as well as the ZnTe coating thickness. The ZnTe-on-Si simulations utilized a standard 220 nm thick Si waveguide core, and the optimized Si core width was determined to be 200 nm to minimize the electric field confinement in the silicon material while still supporting single mode propagation. Figure 67b illustrates the simulated results of increasing electric field confinement within the ZnTe material for thicker layers varying between 25 to 200 nm. The final ZnTe layer thickness was chosen to be 165 nm to ensure a significant majority of approximately 64% electric field confinement within the ZnTe material while minimizing the thin film strain and deposition time of the resulting waveguide design. Similarly, the optimized ZnTe-on-SiN waveguide utilized a 375 nm thick and 200 nm wide SiN core with a 200 nm thick ZnTe coating to obtain 71% electric field confinement in the ZnTe layer.

Figure 67c illustrates the simulated mode profile of the optimized ZnTe-on-Si structure and demonstrates majority electric field confinement in the ZnTe coating layers. These hybrid waveguides were then fabricated using electron beam lithography and reactive ion etching (RIE) to define the Si and SiN core strip waveguides. The ALD growth of ZnTe for each waveguide material platform was then carried out in a home-built flow-type hot-wall ALD system equipped with a chemical series dry vacuum pump (nominal pumping speed = 21 cfm = 35 m<sup>3</sup>/h). The system was leak-checked at 10<sup>-7</sup> Torr with a base pressure of 10

mTorr when operated with the dry pump. The ZnTe coating was then deposited at 85 °C via ALD to achieve a high-quality, conformal layer along the entire waveguide with a precise thickness of 165 nm for the Si platform and 200 nm for the SiN platform.

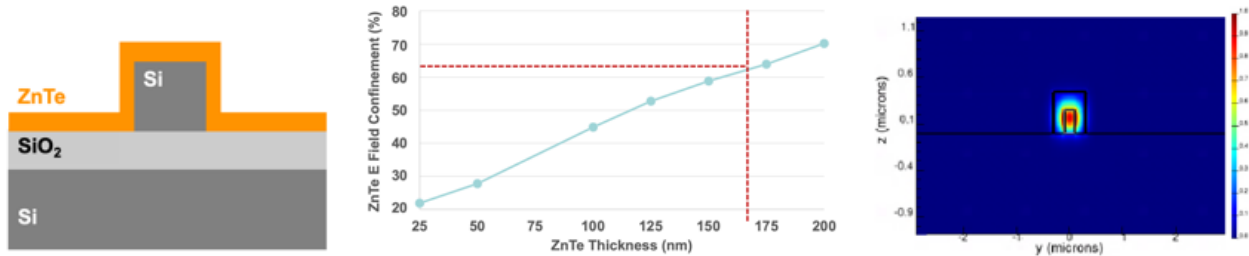


Figure 67. a) Cross-sectional schematic of the hybrid ZnTe-on-Si waveguide design with the conformal ALD ZnTe layer shown in orange. (b) Electric field confinement within the ZnTe material for a Si waveguide core of 220nm thick and 200nm wide increases with coating thickness and achieves 64% confinement for the chosen 165nm ZnTe thickness. (c) Simulated optical mode profile of Si core waveguide at a wavelength of 1565 nm.

#### 4.4 ZnTe $\chi^{(3)}$ Characterization

A top-hat bidirectional nonlinear transmission technique measured the real and imaginary parts of the third-order nonlinear susceptibility for each of the fabricated hybrid waveguide systems. An erbium laser (Menlo Systems ELMO; 80 fs pulse duration, 100 MHz repetition rate) generated optical pulses sent through a programmable optical filter (WaveShaper 500A) to obtain 10 nm linewidth rectangular spectra around the 1565 nm central wavelength with an adjustable dispersion coefficient that enabled elongation of the pulse duration up to several picoseconds. The resulting signal was routed through a 2 m long lens-tipped optical fiber and edge-coupled to the desired waveguide.

This setup illustrated in Figure 68a facilitates two counter-directional nonlinear waveguide transmission measurements by changing the input and output fiber connections. This bi-directional measurement ensures accurate characterization of the coupling efficiencies for each waveguide facet, which is essential to determine the injected power to the waveguide and consequently evaluate the nonlinear susceptibilities of the hybrid waveguide system. The incident average power  $P_{in}$  was measured at the first fiber output after propagating through the optical pulse shaper. The resulting output power spectrum was measured with an

optical spectrum analyzer (OSA Yokogawa AQ6375B) after transmission through the waveguide for varying injected powers  $P_{in}$ .

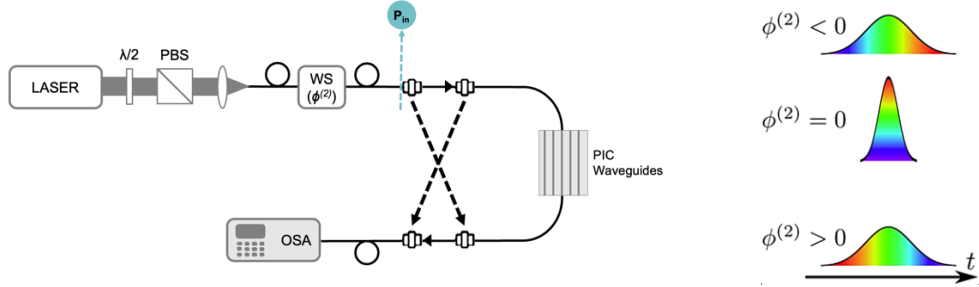


Figure 68. a) Bidirectional nonlinear transmission measurement setup that enables transmission from both input directions (1, 2) represented by the solid and dashed lines, respectively. b) Effect of varying dispersion on the incident pulse stretching and the resulting frequency distribution [44].

To further characterize the nonlinearities of the system and extract the effective Kerr coefficient, a complimentary D-scan method was employed to analyze the intensity-dependent phase shift by varying the beam size in the temporal domain with an adjustable dispersion coefficient ( $\phi^{(2)}$ ) introduced by the pulse shaper. Figure 68b illustrates the pulse stretching in the time domain when  $\phi^{(2)} \neq 0$  and demonstrates the expected optical frequency shifts of the chirped pulse after propagating through media with negative and positive dispersion coefficients, respectively. Following the D-scan measurements, the SPM-induced spectral broadening was quantified through the spectral root mean squared (r.m.s.) linewidth ( $2\sigma$ ) as a function of the dispersion for varying input average powers  $P_{in}$  to extract the effective Kerr coefficient of the hybrid waveguide system.

#### 4.4.1 Hybrid ZnTe-on-Si Waveguide $\chi^{(3)}$ Characterization

The output power spectrum was measured with an optical spectrum analyzer (OSA Yokogawa AQ6375B) after transmission through the waveguide as shown in Figure 69a below for varying injected powers  $P_{in}$  between 2.3 mW to 114 mW. The resulting output spectra measured at an effective zero dispersion demonstrate symmetric spectra with a clear increase in spectral broadening with  $P_{in}$  that confirms the existence of a Kerr-induced self-phase modulation (SPM) effect.

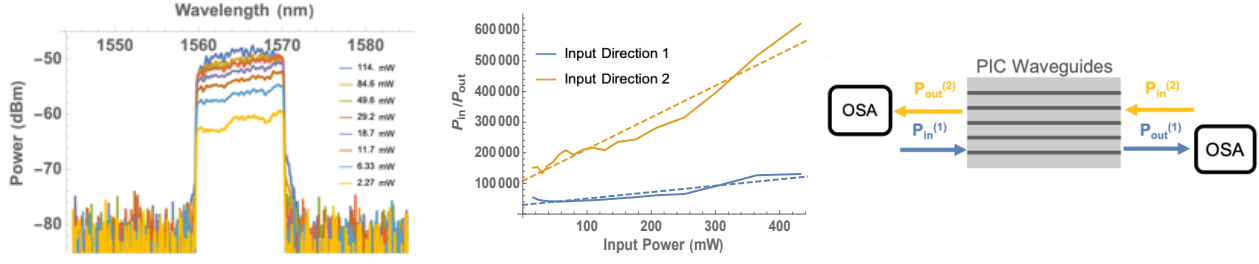


Figure 69. a) Output spectra for input direction 1 for varying  $P_{in}$  between 2.3 mW and 114 mW clearly demonstrate spectral broadening with increasing input power. b) Bidirectional  $P_{in}/P_{out}$  analysis for hybrid ZnTe-on-Si waveguide with the linear fits represented by the dashed lines. c) Experimental setup for bidirectional waveguide measurements.

To evaluate the extent of two-photon absorption, the total output power  $P_{out}$  was integrated for each spectrum to compare the  $P_{in}/P_{out}$  ratio for varying input powers  $P_{in}$  as in Figure 69b. This plot demonstrates a strong, positive linear relationship that consequently verifies the presence of a TPA effect as given by Equation 19, while the significant variation between the linear fit slopes for measurements from each input direction confirms unique coupling efficiencies for each facet. The linear fit coefficients,  $a^{(1,2)}$  and  $b^{(1,2)}$ , are thus related to the input and output coupling efficiencies  $\kappa_{in,out}^{(1,2)}$  of Equations 20 and 21, respectively, where  $S = n_g/n_0$  is the slow-down factor,  $L_{eff}$  is the effective length,  $\alpha$  is the linear propagation loss,  $\eta$  is the normalized temporal shape of the pulse, and  $A_{NL}$  is the nonlinear effective area [36]. By completing the same analysis for both input directions as in [42–43], the  $\beta_{TPA}$  of this hybrid ZnTe-on-Si waveguide system was evaluated according to Equation 22 equal to  $5.76 \times 10^{-13}$  m/W, which is in very good agreement with reported values for Si and ZnTe [37].

$$P_{in}/P_{out}^{(1,2)} = a^{(1,2)} + b^{(1,2)}P_{in} \quad (19)$$

$$a^{(1,2)} = 1/(\kappa_{in}^{(1,2)}\kappa_{out}^{(1,2)}e^{-\alpha L}) \quad (20)$$

$$b^{(1,2)} = (S^2\beta_{TPA}L_{eff}\eta)/(A_{NL}\kappa_{out}^{(1,2)}e^{-\alpha L}) \quad (21)$$

$$\beta_{TPA} = (A_{NL}b^{(1)})/(S^2a^{(1)}\kappa_{in}^{(1)}L_{eff}\eta) \quad (22)$$

The experimental output spectra for the D-scan are plotted in Figure 70a for a fixed input power of  $P_{in} = 40.9$  mW and a variable dispersion coefficient ranging between  $\pm 1.0$  ps/nm. As expected, the largest

spectral broadening occurs close to zero dispersion where the peak power of the incident pulse is maximized and consequently induces the greatest nonlinear effects. These results are further validated by analyzing the variation of the output average power  $P_{\text{out}}$  integrated for each dispersion spectrum as a function of the dispersion as shown in Figure 70b. The output power curve decreases symmetrically towards a minimum at a dispersion of +0.15 ps/nm. This indicates that +0.15 ps/nm is the effective “zero” dispersion point of the system where the pulse duration is minimized and the waveguide system has effectively compensated for the dispersion of the input pulse. Since the input power is constant for all of these dispersion measurements, this decrease in the  $P_{\text{out}}$  curve around the effective “zero” dispersion point clearly results from nonlinear phenomena and increased absorption due to larger TPA effects at high peak pulse intensities.

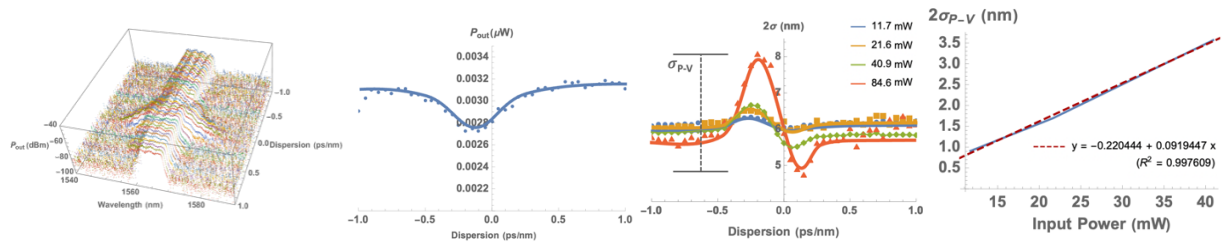


Figure 70. (a) Measured optical spectra for a fixed  $P_{\text{in}} = 40.9 \text{ mW}$  with varying dispersion between  $+/-1.0 \text{ ps/nm}$ . (b) Output average power  $P_{\text{out}}$  and (c) spectral r.m.s. linewidth (with an inset to show the peak-to-valley deviation) for varying dispersion coefficients for  $P_{\text{in}} = 200, 300, 400, \text{ and } 500 \text{ mW}$ . (d) Peak-to-valley linewidth difference as a function of  $P_{\text{in}}$ .

The r.m.s. curves in Figure 70c demonstrate a dispersive shape with large spectral broadening as the dispersion approaches zero. Since the maximum spectral broadening is observed for a positive dispersion, this confirms a positive sign of the second order nonlinear refractive index ( $n_2$ ) for the hybrid waveguide system. For larger absolute dispersion values, the r.m.s. curve flattens and asymptotically tends to the spectral linewidth of the incident pulse. This confirms that the spectral broadening vanishes for large dispersion values as the pulse duration increases and the peak pulse power becomes too low to efficiently generate SPM-induced spectral broadening and TPA effects. Further analysis of the r.m.s peak-to-valley deviation ( $\sigma_{\text{P-V}}$ ) shown in Figure 70d reveals a strong, positive linear relationship as a function  $P_{\text{in}}$ . Since this peak-to-valley deviation is directly correlated to the strength of SPM, this analysis quantitatively confirms a strong SPM effect and enables computational analysis to evaluate the nonlinear phase shift and corresponding effective Kerr coefficient of the system.

$$\phi_{NL} = 2\pi FOM_{TPA} \ln(1 + \beta_{TPA} I_0 L_{eff}) \quad (23)$$

$$\beta_{TPA} I_0 L_{eff} = (P_{in} b^{(1)}) / a^{(1)} \quad (24)$$

$$n_{2,eff} = \lambda_0 \beta_{TPA} FOM_{TPA} \quad (25)$$

$$n_{2-ZnTe} = \frac{1}{\Gamma_{ZnTe}} \left( \frac{n_{ZnTe}}{n_g} \right)^2 \left( \gamma_{eff} \left( \frac{c A_{tot}}{\omega} \right) - n_{2-Si} \left( \frac{n_g}{n_{Si}} \right)^2 \Gamma_{Si} \right) \quad (26)$$

Semi-analytical simulations were performed for varying nonlinear phase shifts ( $\Phi_{NL}$ ) and dispersion values over the same spectral range as shown below in Figure 71a for a fixed nonlinear phase shift of  $\Phi_{NL} = 0.25$  radians [41]. Through similar quantitative analysis as the previously demonstrated experimental results, the r.m.s. linewidth for varying nonlinear phase shifts and the r.m.s peak-to-valley deviation were plotted as shown below in Figures 71 b and c, respectively. By combining the calculated r.m.s. peak-to-valley deviation as a function of the nonlinear phase shift with the experimental measurements of the r.m.s. peak-to-valley deviation as a function of the input power, the experimental nonlinear phase shift was evaluated as a function of the input power as shown below in Figure 71d. Knowing that the nonlinear phase shift is related to the TPA figure of merit and input power through the relations given by Equations 23 and 24 where  $I_0 = (S^2 \eta \kappa_{in}^{(1)} P_{in}) / A_{NL}$ , the slope of the linear fit given by the dashed red line was evaluated to extract the  $FOM_{TPA}$  equal to  $0.78 \pm 0.006$ .

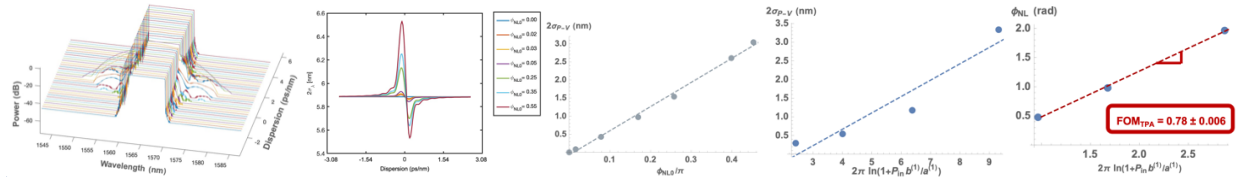


Figure 71. Semi-analytical simulations of the (a) hybrid ZnTe-on-Si waveguide transmission for a fixed  $\Phi_{NL} = 0.25$  rad with varying dispersion and (b) the resulting r.m.s. linewidth ( $\sigma$ ) and (c) r.m.s. peak-to-valley deviation ( $2\sigma_{p,V}$ ). (d)  $FOM_{TPA}$  measurement using a linear fit on the variation between  $\Phi_{NL}$  and

$$2\pi FOM_{TPA} \ln(1 + P_{in} b^{(1)} / a^{(1)}).$$

The effective third-order nonlinear refractive index ( $n_{2,eff}$ ) of the hybrid waveguide system was finally evaluated using Equation 25 with the experimental values to determine  $n_{2,eff} = 7.02 \pm 0.05 \times 10^{-18} \text{ m}^2/\text{W}$ . Since both the silicon waveguide core and the ZnTe coating layer contribute to the effective nonlinearity of

the hybrid waveguide system, the nonlinear refractive index for each of the materials can be computed by accounting for the electric field distribution of the mode at the desired angular frequency ( $\omega$ ). The nonlinear refractive index of the ZnTe coating material ( $n_{2-ZnTe}$ ) is given by Equation 26 where  $\gamma_{eff} = S^2/A_{NL}(k_0 n_{2,eff} + \beta_{TPA}/2)$  represents the effective Kerr coefficient and  $\Gamma_{Si/ZnTe}$  represents the electric field confinement factor in the silicon and ZnTe components [38-40].

Table 12. Summary of measured nonlinear optical properties for hybrid ZnTe-on-Si waveguides.

	ZnTe-on-Si	Si	ZnTe
$\beta_{TPA}$ (m/W)	$5.8 * 10^{-13}$	$8 to 10 * 10^{-13}$	--
FOM <sub>TPA</sub>	$0.78 \pm 0.006$	$0.48 \pm 0.05$	--
$n_2$ (m <sup>2</sup> /W)	$7.02 \pm 0.05 * 10^{-18}$	$6.8 \pm 2.2 * 10^{-18}$	$7.1 \pm 0.7 * 10^{-18}$

Table 12 summarizes the experimental results for all nonlinear coefficients of the hybrid ZnTe-on-Si waveguide system and demonstrates a nonlinear refractive index for the ZnTe material coating of  $n_{2,ZnTe} = 7.1 \pm 0.7 * 10^{-18}$  m<sup>2</sup>/W. This experimental  $n_{2,ZnTe}$  closely matched reported values of approximately  $7.8 * 10^{-18}$  m<sup>2</sup>/W, which further confirms the accuracy and validity of the experimental D-scan analysis of the hybrid waveguide system. Additionally, the ZnTe-on-Si waveguide system achieves a high FOM<sub>TPA</sub> compared to that of pure silicon due to a significantly reduced TPA coefficient with a comparable nonlinear coefficient. The results consequently demonstrate the suitability of ZnTe-on-Si waveguides for future low-loss, high-performance, and compact integrated nonlinear devices particularly when accounting for the additional second-order nonlinear Pockels effect contributions from the ZnTe coating layer.

#### 4.4.2 Hybrid ZnTe-on-SiN Waveguide $\chi^{(3)}$ Characterization

To further evaluate the  $\chi^{(3)}$  Kerr coefficient of the ALD ZnTe thin films, the same D-Scan experiment was performed for hybrid ZnTe-on-SiN waveguides. There are also several advantages to using SiN core waveguides compared to Si for analysis of the ZnTe thin films. Most importantly, SiN has a much lower linear refractive index compared to Si ( $n_{0,SiN} = 2.05$ ;  $n_{0,Si} = 3.48$ ), which leads to higher optical mode confinement in the ZnTe coating for the SiN core waveguides. SiN

also has a much lower nonlinear Kerr coefficient compared to Si ( $n_{2,\text{SiN}} = 2.4 * 10^{-15} \text{ cm}^2/\text{W}$ ;  $n_{2,\text{Si}} = 4.2 * 10^{-14} \text{ cm}^2/\text{W}$ ), which would reduce the contributions of the waveguide core material to the experimental nonlinearities and simplify extraction of the ZnTe Kerr coefficient from the resulting waveguide measurements. Finally, SiN has a much larger bandgap than Si which consequently eliminates any TPA effects at 1565nm and reduces the optical propagation losses.

To first demonstrate the presence of a Kerr-induced self-phase modulation (SPM) effect in these hybrid ZnTe-on-SiN waveguides, the output power spectrum was measured after transmission through the waveguide for varying injected powers  $P_{\text{in}}$  between 4.2 mW to 57 mW as shown in Figure 72. The resulting output spectra measured at an effective zero dispersion demonstrate symmetric spectra with a clear increase in spectral broadening with  $P_{\text{in}}$  as evidenced by the generation of additional frequencies at the edges of the incident top-hat pulse and experimentally confirm the third-order nonlinearities within the waveguide system. This incident power sweep was performed for both input directions to accurately extract the coupling coefficients for each waveguide facet.

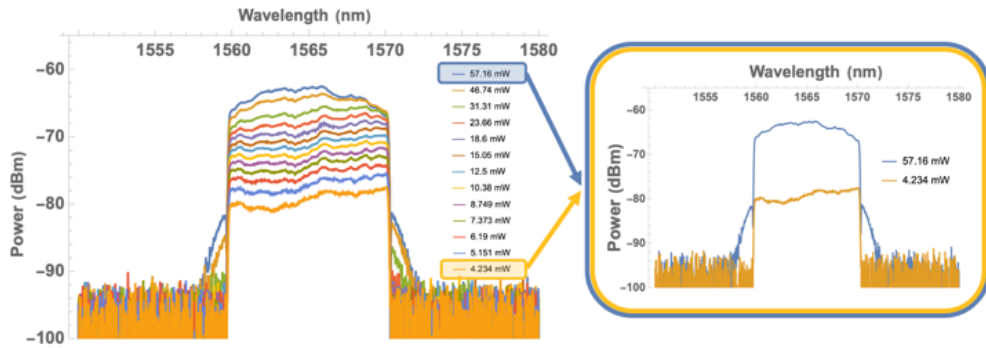


Figure 72. Output spectra for input direction 1 for varying  $P_{\text{in}}$  between 4.2 mW and 57 mW demonstrate significant spectral broadening with increasing input power.

The experimental output spectra for the D-scan are plotted in Figure 73a for a fixed input power of  $P_{\text{in}} = 57$  mW and a variable dispersion coefficient ranging between  $\pm 1.0 \text{ ps/nm}$ . As with the Si core waveguides, the largest spectral broadening occurs close to zero dispersion where the peak power of the incident pulse is maximized and consequently induces the greatest nonlinear effects. To verify the lack of TPA effects within these SiN core waveguides, the output average power  $P_{\text{out}}$  was integrated for each dispersion and plotted as a function of the dispersion as shown in Figure 73b. In contrast to the Si core waveguide measurements that demonstrated a decrease in the  $P_{\text{out}}$  curve around zero due to larger TPA effects at high

peak pulse intensities, the SiN core waveguide results demonstrate flat  $P_{\text{out}}$  spectra versus dispersion and confirm that there is no significant TPA within the ZnTe-on-SiN waveguides.

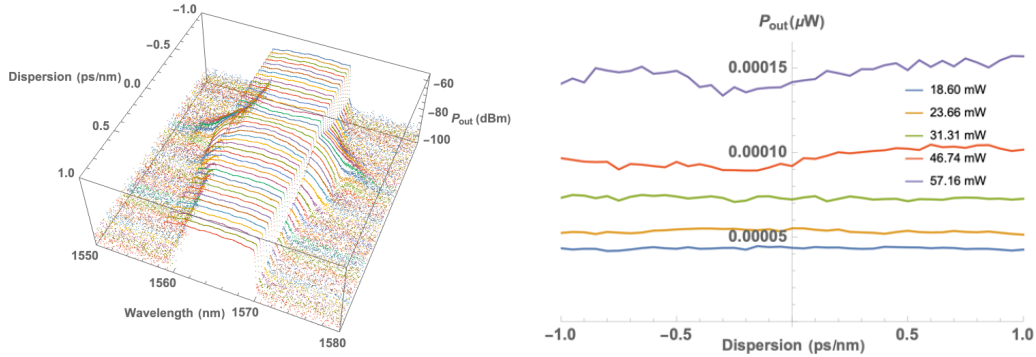


Figure 73. a) Measured optical spectra for a fixed  $P_{\text{in}} = 57$  mW with varying dispersion between  $+/-1.0$  ps/nm. (b) Flat integrated output average power  $P_{\text{out}}$  as a function of dispersion for various  $P_{\text{in}}$  confirms no TPA effects.

The D-scan measurements were further analyzed to extract the r.m.s. spectral linewidth ( $2\sigma$ ) as a function of dispersion as shown in Figure 74a. Similar to the Si core waveguides, the r.m.s. curves create a dispersive shape with the largest  $2\sigma$  observed near zero dispersion where the peak power of the incident pulse is the highest and achieves the largest nonlinear SPM effects. As the dispersion increases towards  $+/-1.0$  ps/nm, the SPM effects decrease and the r.m.s. spectral linewidth tends towards that of the incident top-hat spectral pulse. Additionally, the maximum  $2\sigma$  occurs for a negative dispersion to confirm a positive  $n_2$  coefficient of the hybrid waveguide system.

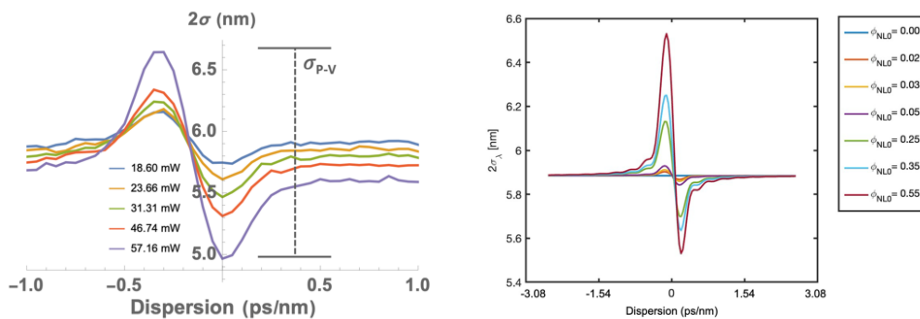


Figure 74. a) Experimental and b) simulated spectral r.m.s. linewidth (with an inset to show the peak-to-valley deviation in (a)) as a function of dispersion for various  $P_{\text{in}}$ .

Semi-analytical simulations were performed to estimate the induced nonlinear phase shift for the experimental dispersion spectra with different input powers. Figure 74b illustrates the simulated r.m.s. spectral linewidth curves that closely match the experimental results of Figure 74a. By extracting the  $2\sigma_{P-V}$  from each dispersion scan, it is clear there is a strong, positive linear relationship for the SPM effects with increasing input power and nonlinear phase shift as shown in Figure 75a-b for the experimental and simulation results, respectively. These results were then combined to evaluate the induced nonlinear phase shift of the incident optical pulse with varying input powers after propagating through the hybrid ZnTe-on-SiN waveguide. In accordance with Equation 27, the slope of the nonlinear phase shift as a function of  $P_{in}$  is proportional to the effective Kerr coefficient, which is determined to be  $n_{2,ZnTe-on-SiN} = 3.1 \pm 0.1 * 10^{-18} m^2/W$ . This effective hybrid waveguide Kerr coefficient is comparable to that of pure Si but benefits from complete elimination of any TPA effects that would significantly reduce the optical losses in high-power applications.

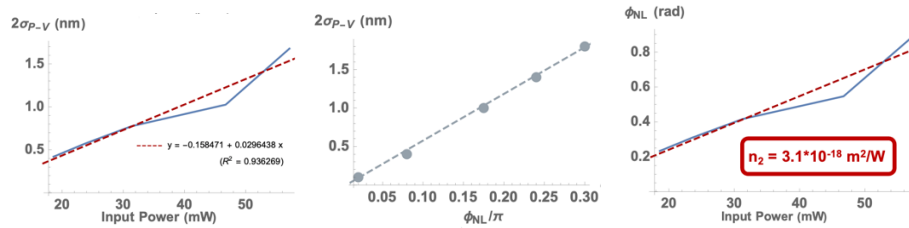


Figure 75. a) Experimental peak-to-valley linewidth deviation as a function of  $P_{in}$ . b) Simulated peak-to-valley linewidth deviation for varying nonlinear phase shifts c) combined with the experimental results to extract the nonlinear Kerr coefficient of the hybrid waveguide system.

$$\Phi_{NL}^{(1,2)} = \frac{S^2 \eta k_0 L_{eff} n_2}{A_{NL}} \kappa_{in}^{(1,2)} P_{in} \propto n_2 P_{in} \quad (27)$$

The nonlinear refractive indices for each of the SiN core and ZnTe coating components within this hybrid waveguide system were evaluated by accounting for the electric field distribution of the mode at the desired angular frequency ( $\omega$ ) as indicated by Equation 26 where  $\gamma_{eff} = S^2 / (A_{NL} k_0 n_{2,eff})$ . As a result, the Kerr coefficient of the ZnTe coating material is determined to be  $n_{2,ZnTe} = 6.1 \pm 0.1 * 10^{-18} m^2/W$  which closely matches the experimentally determined value from the previous ZnTe-on-Si waveguide experiments. Table 13 summarizes the results from both Si and SiN core waveguide experiments and

demonstrates consistent experimental coefficients between the Si and SiN core measurements (approximately 14% error) and in comparison with literature (less than 22% error).

Table 13. Experimental and literature values for the nonlinear coefficients of ZnTe and the hybrid waveguide designs.

	Material	$n_2$ ( $m^2/W$ )	% Error
Literature	Pure SiN	$2.4 \pm 0.7 * 10^{-19}$	--
	Pure Si	$5.0 \pm 0.8 * 10^{-18}$	--
	ZnTe	$8.0 \pm 0.7 * 10^{-18}$	--
Experimental	ZnTe-on-SiN	$3.1 \pm 0.1 * 10^{-18}$	--
	ZnTe (fom Hybrid SiN)	$6.1 \pm 0.1 * 10^{-18}$	$22.4 \pm 8$
	ZnTe-on-Si	$7.02 \pm 0.05 * 10^{-18}$	--
	ZnTe (fom Hybrid Si)	$7.1 \pm 0.7 * 10^{-18}$	$12.5 \pm 6$

In conclusion, comprehensive materials characterization was performed for novel ZnTe-on-Si and ZnTe-on-SiN material systems to evaluate the linear and nonlinear optical properties. Both of these material platforms are highly compatible with conventional fabrication techniques as the ALD of the ZnTe layer occurs via back-end-of-line procedures and does not require further processing. Ellipsometry confirmed the large linear refractive index and negligible extinction coefficient of ZnTe that consequently enable high optical confinement with minimal propagation loss in the C band. The combination of a bidirectional top-hat spectral broadening measurement and D-Scan experiment led to accurate measurement of  $\beta_{TPA}$  in the Si core waveguides and the optical Kerr coefficients ( $n_2$ ) of both Si- and SiN-based hybrid waveguide systems. The decreased TPA coefficient by an order of magnitude for the Si core waveguides compared to pure Si waveguides and complete elimination of TPA for the SiN core waveguides with comparable nonlinear Kerr coefficients result in a significant improvement in the nonlinear FOM for these systems. As such, these results demonstrate the promise of novel hybrid ZnTe-on-Si and SiN material platforms for future low-loss, compact, integrated nonlinear infrared devices.

## 4.6 Theoretical Device Design for ZnTe Electro-Optic Modulators

Having successfully demonstrated the strong nonlinear properties of ALD ZnTe, there are many potential applications to leverage these nonlinearities in integrated photonic devices. For example, nonlinear electro-optic materials enable precise and dynamic control of propagating optical signals as these materials demonstrate small changes in their refractive index when subjected to an applied electric field. Electro-optic modulators are consequently capable of modifying the phase, polarization state, and intensity of incoming signals and can be designed to produce a wide range of electrically controllable optical devices, such as variable focus lenses, beam scanning devices, optical phase modulators, wave retarders, and optical intensity modulators or optical switches.

Electro-optic modulators are essential components in modern telecommunication networks and microwave-photonic systems due to their ability to translate high-speed electronic signals into the optical domain. In addition, electro-optic modulators are of interest for several other applications such as quantum photonics and non-reciprocal optics [35]. All of these applications require integrated, chip-scale electro-optic modulators with large electro-optic bandwidths and very low optical losses that are also compatible with current CMOS technology. Many previous integrated modulator material platforms have intrinsic limitations, and alternative material platforms such as lithium niobate ( $\text{LiNbO}_3$ ) have not yet achieved simple on-chip integration due to fabrication limitations as well as limited bandwidth and high voltage requirements [35]. The following section describes the operating principles of electro-optic modulators and presents a compelling design for a ZnTe-based device that could improve upon the current leading technology.

### 4.6.1 Operating Principles of Electro-Optic Modulators

Electro-optic modulators rely on the application of the electro-optic effect, which describes how the refractive index of nonlinear materials is a function of an applied steady-state or slowly varying electric field. Since the refractive index only varies slightly with the application of an external electric field, it can be expanded in a Taylor series as shown below,

$$n(E) = n + a_1 E + \frac{1}{2} a_2 E^2 + \dots \quad (28)$$

where the expansion coefficients are  $n = n(0)$ ,  $a_1 = \left(\frac{dn}{dE}\right)|_{E=0}$ , and  $a_2 = \left(\frac{d^2n}{dE^2}\right)|_{E=0}$ . This equation can be re-written for convenience as

$$n(E) = n - \frac{1}{2}rn^3E - \frac{1}{2}s n^3 E^2 + \dots \quad (29)$$

where  $r = -2a_1/n^3$  and  $s = -a_2/n^3$  are the Pockels second- and Kerr third-order electro-optic coefficients, respectively. These higher order terms are generally many orders of magnitude smaller than the first-order refractive index ( $n$ ), but they are still capable of altering the properties of incident light waves when exposed to a sufficient electric field and propagation length through the nonlinear material [45].

#### 4.6.1.1 Pockels Effect

While the refractive index change demonstrated above in Equation 29 is dependent on both second- and third-order nonlinear coefficients, there are many materials in which the third-order term is negligible in comparison to that of the second-order [46]. These materials, referred to as Pockels media, consequently have a simplified refractive index relationship given by Equation 30.

$$n(E) \approx n - \frac{1}{2}rn^3E \quad (30)$$

This demonstrates a linear relationship between the applied electric field strength and the change in refractive index, which is illustrated in Figure 76a. Many common electro-optic modulator materials, such as Gallium Arsenide (GaAs), Indium Phosphide (InP), Lithium Niobate ( $\text{LiNbO}_3$ ), are primarily Pockels media, and their unique properties will be described in greater detail in Section 4.6.3.

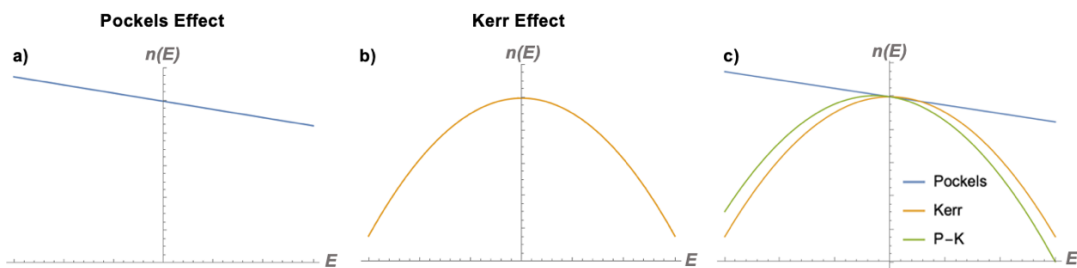


Figure 76. Refractive index versus applied electric field strength for a) Pockels, b) Kerr, and c) Pockels-Kerr (P-K) based nonlinear materials.

#### 4.6.1.2 Kerr Effect

---

In contrast to Pockels media, there are many materials in which the third-order Kerr coefficient dominates when compared to the Pockels coefficient. Furthermore, in centrosymmetric materials including gases, liquids, and some crystals, the Pockels coefficient vanishes completely so that the Kerr effect is solely responsible for any observable nonlinear properties [45]. This is due to the fact that  $n(E)$  must be an even, symmetric function for centrosymmetric materials in order to satisfy the invariance to the reversal of the electric field. As a result, the refractive index equation can be simplified and is given by

$$n(E) \approx n - \frac{1}{2} \epsilon n^3 E^2 \quad (31)$$

which demonstrates a quadratic dependence of the refractive index on the electric field, as illustrated by Figure 76b.

#### 4.6.1.3 Combined Pockels and Kerr Effects

---

While these simplifications can be applied to the vast majority of nonlinear materials to categorize between Pockels and Kerr media, there are some unique materials that demonstrate both Pockels and Kerr effects simultaneously [46 - 47]. As a result, the full expression given by Equation 29 must be considered for these materials in order to accurately model the nonlinear response and refractive index change when subjected to an electric field. Figure 76c illustrates the potential to achieve a larger refractive index change for Pockels-Kerr (P-K) media when compared to solely Pockels- or Kerr-based materials. Due to these unique relationships between the applied field strength and the change in refractive index for Pockels, Kerr, and P-K materials, electro-optic modulators can demonstrate different voltage dependencies based on the material selection.

### 4.6.2 Types of Electro-Optic Modulators and Device Designs

There are many different types of electro-optic modulators, including phase modulators, dynamic wave retarders or polarization modulators, and intensity modulators. Each of these modulators utilizes a unique device design to exploit the nonlinear properties of the given material and control the phase, polarization, or power of the incoming light wave. These devices typically contain one or two Pockels or Kerr cells that are sometimes combined with other optical elements such as

polarizers or interferometers. Each of these types of modulators and the corresponding device designs will be discussed in further detail in the following sections.

#### 4.6.2.1 Phase Modulators

---

Phase modulators are the simplest type of electro-optic modulators, which contain a single Pockels or Kerr cell. Electrodes are used to apply an electric field across the nonlinear material and consequently produce a phase change within the light beam traversing the length of the cell [4]. In order to maintain a constant polarization state for the incoming and output light beam in phase modulator devices, the polarization of the input beam is generally aligned with one of the optical axes of the crystal. For a Pockels cell of length L, the corresponding phase shift of the incoming signal is given by,

$$\varphi_{\text{Pockels}} = n(E)k_0L \approx \varphi_0 - \pi \frac{rn^3EL}{\lambda_0} \quad (32)$$

where  $\varphi_0 = 2\pi nL/\lambda_0$ , and  $E = V/d$  is the electric field strength for an applied voltage V across the two faces of the cell separated by distance d. This equation is often rewritten in terms of the Pockels half-wave voltage ( $V_{\pi,\text{Pockels}}$ ) as shown below,

$$\varphi_{\text{Pockels}} \approx \varphi_0 - \pi \frac{V}{V_{\pi,\text{Pockels}}} \quad (33)$$

where  $V_{\pi,\text{Pockels}} = d\lambda_0/Lrn^3$ . This equation demonstrates the linear relationship between the optical phase shift and the applied voltage, while the half-wave voltage parameter determines the applied voltage necessary to achieve a  $\pi$  phase shift of the output signal relative to the input wave. These results are further explained by Figure 77a below which illustrates this linear dependence of the phase shift on applied voltage for Pockels-based phase modulators.

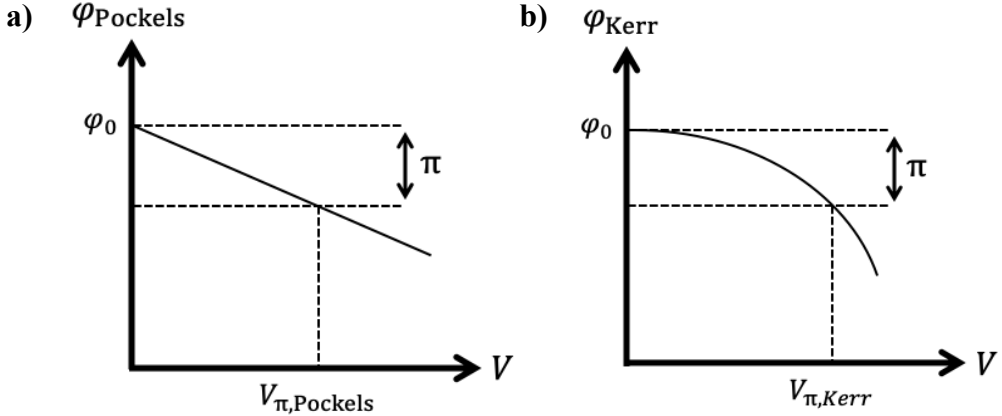


Figure 77. Phase shift versus applied voltage for a) Pockels and b) Kerr nonlinear materials.

In contrast to Pockels cell electro-optic phase modulators, centrosymmetric materials with vanishing Pockels coefficients rely on the Kerr effect to achieve the desired electro-optic phase modulation. As previously described in Section 4.6.1.2, the refractive index for Kerr media has a quadratic dependence on the applied electric field [47-49]. Therefore, the phase shift of the incident light through a Kerr phase modulator has a different relationship with the applied voltage when compared to that of a Pockels cells given by Equation 6. For a Kerr cell of length L, the corresponding phase shift of the incoming signal is given by,

$$\varphi_{\text{Kerr}} = n(E)k_0L \approx \varphi_0 - \pi \frac{s n^3 E^2 L}{\lambda_0} \quad (34)$$

where  $\varphi_0 = 2\pi nL/\lambda_0$ . In order to compare this equation to that of a Pockels cell, this relationship can be rewritten in terms of the Kerr half-wave voltage ( $V_{\pi,\text{Kerr}}$ ) as shown below,

$$\varphi_{\text{Kerr}} \approx \varphi_0 - \pi \left( \frac{V}{V_{\pi,\text{Kerr}}} \right)^2 \quad (35)$$

where  $V_{\pi,\text{Kerr}} = d\sqrt{\lambda_0/L s n^3}$ . This equation demonstrates the quadratic relationship between the optical phase shift and the applied voltage [50-51]. Similar to the Pockels equations above, the half-wave voltage parameter determines the applied voltage necessary to achieve a  $\pi$  phase shift. These results are further explained by Figure 77b above which illustrates this quadratic dependence of the phase shift on applied voltage for Kerr-based phase modulators.

For many materials, either the Kerr effect or the Pockels effect dominates based on the relative magnitude of the electro-optic coefficients, but there are some materials in which both the Pockels and Kerr effect contribute to electro-optic phase modulation. For these devices, which will be referred to as Pockels-Kerr (P-K) phase modulators, the phase shift of incident light is given by,

$$\varphi_{P-K} = n(E)k_0L \approx \varphi_0 - \pi \frac{rn^3EL}{\lambda_0} - \pi \frac{sn^3E^2L}{\lambda_0} \quad (36)$$

$$\varphi_{P-K} = \varphi_0 - \pi \frac{V}{V_{\pi,P-K}} - \pi \left( \frac{V}{V_{\pi,P-K}} \right)^2 \quad (37)$$

$$V_{\pi,P-K} = \frac{d}{2s} \left( -r + \sqrt{r^2 + 4s\lambda_0/Ln^3} \right) \quad (38)$$

where  $\varphi_0 = 2\pi nL/\lambda_0$ . In order to compare these P-K phase modulators to those composed of a Pockels or Kerr cell, the P-K modulator half-wave voltage ( $V_{\pi,P-K}$ ) can be evaluated by the expression shown above in Equation 11. For a material that demonstrates appreciable Pockels and Kerr effects, the relationship between  $\varphi_{P-K}$ ,  $\varphi_{Kerr}$ , and  $\varphi_{P-K}$  is illustrated by Figure 78 below to demonstrate the unique dependence of each of these phenomena on the applied voltage. While the relative magnitude of the effects depends on the material parameters ( $r$  and  $s$ ), this schematic demonstrates the potential for P-K materials to realize smaller  $V_{\pi}$  values when compared to materials that solely rely on either the Pockels or Kerr effect. Additionally, this illustration demonstrates that depending on the operating voltage regime, there are certain situations in which it may be advantageous to utilize a Kerr-based modulator for higher applied voltages or a Pockels-based modulator for lower operating voltages to achieve a steeper phase shift slope and thus a more sensitive device. Further quantitative analysis of these results for specific material systems will be discussed in Section 4.6.3 to evaluate the benefits of different materials, device designs, and operating methods.

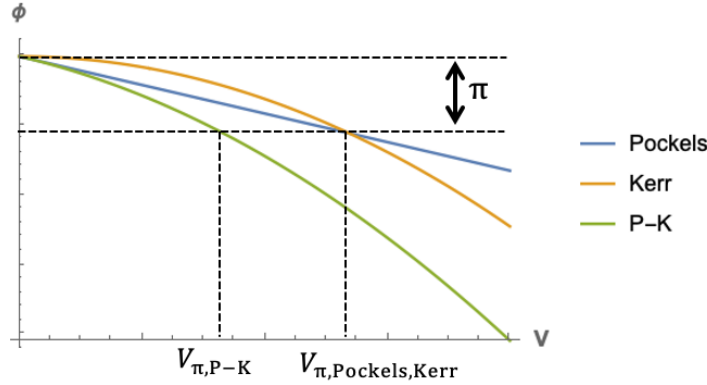


Figure 78. Representative electro-optic phase shift versus applied voltage for materials with only Pockels (blue), only Kerr (yellow), or both P-K (green) contributions to the observed nonlinearities.

For all of these devices (Pockels, Kerr, and P-K phase modulators), the half-wave voltage expressions demonstrate a strong dependence on both the material parameters, such as  $r$  and  $s$ , as well as the device design ( $d/L$ ). Since it is desirable to minimize  $V_\pi$  to obtain a large phase shift response with a low operating voltage, these expressions can be further examined to determine the material and design parameters that will optimize the device performance. For instance, since the  $V_{\pi,Pockels}$  and  $V_{\pi,Kerr}$  are inversely proportional to  $r$  and  $\sqrt{s}$ , respectively, highly efficient Pockels or Kerr phase modulators can be designed by selecting and properly orienting nonlinear materials such that light propagates along the crystallographic direction with the largest electro-optic coefficient.

In addition to this material parameter relationship, the half-wave voltage for phase modulators is also closely related to the device design dimensions, which is represented by the ratio of the electrode separation to the propagation length ( $d/L$ ). There are two common phase modulator designs, including longitudinal and transverse modulators [45]. In longitudinal modulator devices, the electrical contacts are placed on either end of the nonlinear cell parallel to the direction of propagation, as shown in Figure 79a. In this case, the electric field is applied parallel to the propagation direction, and the design is restricted such that  $d = L$ . On the other hand, transverse modulators are designed such that the electric field is applied perpendicular to the direction of propagation and the electrical contact separation distance  $d$  is independent of the propagation

length L as shown in Figure 79b. Since the half-wave voltage is proportional to  $d/L$  and  $d/\sqrt{L}$  for Pockels and Kerr phase modulators, respectively, transverse modulators can be designed to minimize the electrode separation distance with respect to the propagation length to decrease the  $d/L$  ratio and consequently minimize the applied voltage requirements. This design is commonly implemented for waveguide-integrated optical devices as shown in Figure 79c, where the electrode separation is much less than the propagation distance ( $d \ll L$ ). Due to this optimized design structure, the half-wave voltage for integrated transverse modulators can be as low as a few volts, compared to hundreds of volts for free-space transverse modulators and a few kilovolts for longitudinal modulators. Each of these design possibilities will be discussed in further detail in Section 4.6.3 to compare the achievable half-wave voltage values for different material systems.

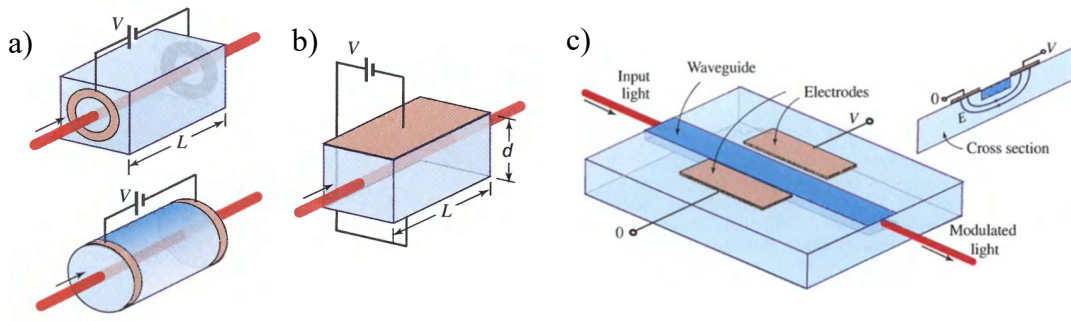


Figure 79. a) Longitudinal, b) transverse, and c) waveguide-integrated electro-optic phase modulator designs with differential electrode separation distances (d) and propagation lengths (L) [52].

#### 4.6.2.2 Dynamic Wave Retarders – Polarization Modulator

In addition to phase modulators, dynamic wave retarders are another type of electro-optic devices capable of converting incoming light waves with a specific form of polarization into another form of polarization. Dynamic wave retarders require the use of anisotropic nonlinear materials, such that the refractive indices and electro-optic Pockels and/or Kerr coefficients vary for the different principal axes of the crystal. Therefore, light propagating along one principal axis (such as the z-axis), can be linearly polarized with arbitrary orientation in the x-y plane and can consequently be decomposed and represented as the sum of two normal modes that are polarized in the x and y directions [45]. Since each of these axes has a unique refractive index and electro-optic coefficient

in anisotropic materials, each of these modes propagates with a different velocity given by  $v_1 = c_0/n_1$  and  $v_2 = c_0/n_2$ . After propagating through a distance  $d$ , the phase shift for each of these normal modes is  $\varphi_x = n_1 k_0 d$  and  $\varphi_y = n_2 k_0 d$ , which results in a relative phase retardation given by Equation 39 below.

$$\varphi = \varphi_y - \varphi_x = (n_2 - n_1)k_0 d \quad (39)$$

For a nonzero relative phase retardation between these two normal modes, this results in the transformation of the initially linearly polarized wave to an elliptically or circularly polarized output wave. While this behavior has limited applications on its own, this phenomenon can be dynamically controlled through the application of an electric field to induce additional electro-optic changes in the refractive indices.

As previously described in Section 4.6.1, the electro-optic effect demonstrates a change in the refractive index in the presence of an electric field that is governed by the Pockels and Kerr coefficients as shown in Equations 30 and 31, respectively. For anisotropic materials, the electro-optic coefficients vary for different crystallographic directions and can consequently control the relative phase retardation of incoming normal modes. Therefore, for a Pockels cell, the change in refractive index in the  $x$ -direction under an applied field is given by  $n_1(E) \approx n_1 - \frac{1}{2}r_1 n_1^3 E$ . Similar equations can be applied to the remaining crystallographic directions, where  $r_1$  and  $r_2$  are the Pockels coefficients for the corresponding polarization directions. After propagating a distance  $L$  through the material, Equation 32 can be modified to account for the relative phase retardation under an applied field as given by Equation 40 below.

$$\Gamma_{\text{Pockels}} = k_0 L [n_1(E) - n_2(E)] = k_0 L (n_1 - n_2) - \frac{1}{2} k_0 E L (r_1 n_1^3 - r_2 n_2^3) \quad (40)$$

Similar to the case of phase modulators described in the previous section, this relative phase retardation ( $\Gamma$ ) can be re-written in terms of the half-wave voltage ( $V_{\pi, \text{Pockels}}$ ) as shown below,

$$\Gamma_{\text{Pockels}} = \Gamma_0 - \pi \frac{V}{V_{\pi, \text{Pockels}}} \quad (41)$$

$$V_{\pi, \text{Pockels}} = \frac{d}{L} \frac{\lambda_0}{(r_1 n_1^3 - r_2 n_2^3)} \quad (42)$$

where  $\Gamma_0 = k_0 L(n_1 - n_2)$  is the same phase retardation given by Equation 39 in the absence of an electric field. Figure 80a illustrates this linear dependence of the modal phase retardation on the applied voltage, which can consequently be utilized to transform the polarization of incoming light waves from linear ( $\Gamma = 0, n\pi$ ) to elliptical or circular ( $\Gamma = \frac{\pi}{2} + n\pi$ ) as shown in Figure 80b.

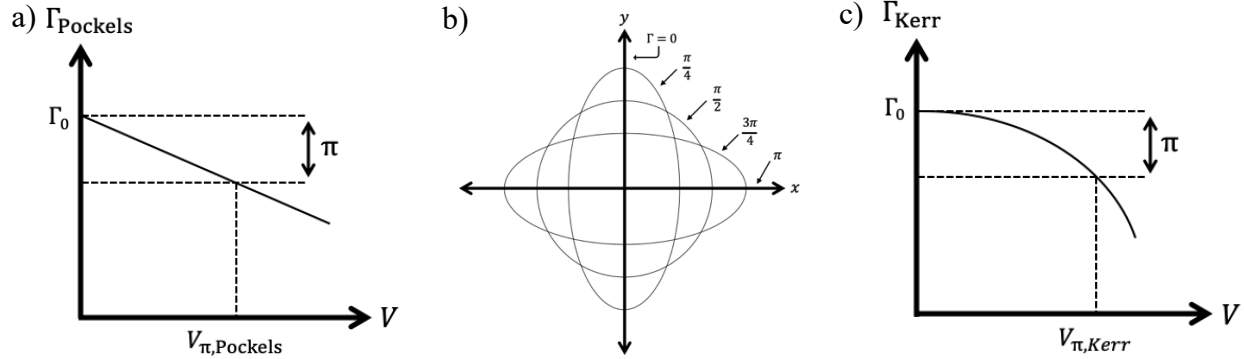


Figure 80. Phase retardation versus applied voltage for a) Pockels and c) Kerr materials, which result in polarization modulation to the corresponding polarization ellipses of b) [4].

While these equations demonstrate the operation of a dynamic wave retarder using a Pockels cell, similar relationships can be derived for Kerr media. In this case, Equation 34 can be modified such that the relative phase shift for a Kerr-based dynamic wave retarder is given by

$$\Gamma_{\text{Kerr}} = k_0 L[n_1(E) - n_2(E)] = k_0 L(n_1 - n_2) - \frac{1}{2} k_0 E^2 L(s_1 n_1^3 - s_2 n_2^3) \quad (43)$$

where  $s_1$  and  $s_2$  are the appropriate Kerr coefficients for the propagating normal modes. This equation can then be simplified in terms of the half-wave voltage to obtain the expressions below.

$$\Gamma_{\text{Kerr}} = \Gamma_0 - \pi \left( \frac{V}{V_{\pi, \text{Kerr}}} \right)^2 \quad (44)$$

$$V_{\pi, \text{Kerr}} = d \sqrt{\frac{\lambda_0}{L(s_1 n_1^3 - s_2 n_2^3)}} \quad (45)$$

This relationship is illustrated by Figure 80c, which demonstrates the quadratic dependence of the modal phase retardation on the applied voltage. Similar to Pockels wave retarders, these phase

retardations transform the incoming light polarization in accordance with the polarization ellipses shown in Figure 80b.

Many devices are classified as Pockels or Kerr media, but there are some materials in which both effects contribute to electro-optic modulation. For these P-K wave retarder devices, the overall phase retardation is a combination of those given by Equations 40 and 43 above. The phase retardation for these devices is thus given by Equation 46 below.

$$\Gamma_{P-K} = k_0 L [n_1(E) - n_2(E)] = k_0 L (n_1 - n_2) - \frac{1}{2} k_0 E L (r_1 n_1^3 - r_2 n_2^3) - \frac{1}{2} k_0 E^2 L (s_1 n_1^3 - s_2 n_2^3) \quad (46)$$

In order to compare these P-K wave retarders to those composed of a Pockels or Kerr cell, the P-K retarder half-wave voltage ( $V_{\pi,P-K}$ ) can be evaluated by the expressions shown below,

$$\Gamma_{P-K} = \Gamma_0 - \pi \frac{V}{V_{\pi,P-K}} - \pi \left( \frac{V}{V_{\pi,P-K}} \right)^2 \quad (47)$$

$$V_{\pi,P-K} = \frac{d}{2\Delta s} \left( -\Delta r + \sqrt{\Delta r^2 + 4\Delta s \lambda_0 / L} \right) \quad (48)$$

where  $\Delta r = (r_1 n_1^3 - r_2 n_2^3)$  and  $\Delta s = (s_1 n_1^3 - s_2 n_2^3)$ . This relationship is very similar to that of P-K phase modulators given by Equations 37 and 38, except that the anisotropic material effects have now been considered to account for additional phase retardation that occurs when the incoming light is not oriented along a particular optical axis.

#### 4.6.2.3 Intensity Modulators (Phase Modulator Inside Interferometer)

---

In addition to phase modulation devices, electro-optic modulators can also be applied to achieve intensity modulation of the incoming electromagnetic signal. One method to achieve intensity modulation is through the use of a phase modulator placed within an interferometer [45]. Figure 81 illustrates a typical integrated-optical intensity modulator design, in which an electro-optic phase modulator is implemented in one branch of the Mach-Zehnder interferometer. If the beam splitter divides the incident optical power ( $I$ ) evenly between the two branches of the interferometer, then the resulting intensity of the modulated and transmitted light through the output port is given by,

$$I_0 = \frac{1}{2} I_i + \frac{1}{2} I_i \cos \varphi = I_i \cos^2(\varphi/2) \quad (49)$$

where  $\varphi = \varphi_1 - \varphi_2$  is the phase shift difference between the two arms of the interferometer. This expression can then be normalized by the incident optical power to evaluated the total transmittance of the interferometer, which is given by  $T = I_0/I_i = \cos^2(\varphi/2)$ . If a phase modulator is placed in branch 1 of the interferometer, the phase shift of the light propagating through this pathway ( $\varphi_1$ ) is given by Equations 32, 34, and 36 for Pockels, Kerr and mixed nonlinear materials, respectively [45]. Therefore, the overall phase difference for a Pockels cell can be represented by the following equation,

$$\varphi_{\text{Pockels}} = \varphi_1 - \varphi_2 = \varphi_0 - \pi \frac{V}{V_{\pi, \text{Pockels}}} \quad (50)$$

where  $\varphi_0 = \varphi_{10} - \varphi_2 = 2\pi n \Delta L / \lambda$  is a constant that depends on the optical path length difference ( $\Delta L$ ) between the two arms of the Mach-Zehnder interferometer. If the phase difference constant is set to  $\varphi_0 = \pi/2$  by designing an interferometer with a  $\Delta L = \lambda/4n$  path length difference, then this device can be operated as an intensity modulator with approximately linear dependence of transmittance on the applied voltage as given by

$$T(V) = \cos^2 \left( \frac{\varphi_0}{2} - \frac{\pi}{2} \frac{V}{V_{\pi, \text{Pockels}}} \right) \quad (51)$$

This relationship is further illustrated by Figure 81b, where the small changes in the applied voltage around point B lead to an approximately linear change in transmittance. Furthermore, this function demonstrated the possibility to use these modulators as an optical switch that can achieve full transmission in the “on” state at point A or zero transmission in the “off” state at point C.

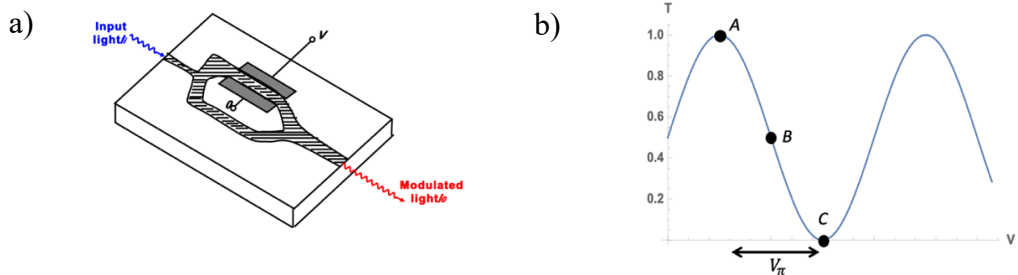


Figure 81. a) An integrated optical intensity modulator composed of a Mach-Zehnder interferometer with an electro-optic phase modulator in one branch of the device [45]. b)

Transmission spectrum versus applied voltage demonstrates a linear response around point B and/or optical switch capabilities when transitioning from points A to C.

While this example illustrates the operation of a Pockels cell intensity modulator, similar relationships can be derived to determine the dependence of transmittance on the applied voltage for both Kerr and Pockels-Kerr modulators. In order to develop a highly sensitive electro-optic intensity modulator, it is desirable to minimize the half-wave voltage for all of these devices such that the period of transmittance oscillation occurs over a smaller voltage range and the slope of the linear region around point B increases. For devices with smaller  $V_{\pi}$  parameters, this would result in larger intensity changes for the same change in voltage, which would consequently be easier to detect and control. This relationship is illustrated by Figure 82 below, in which  $V_{\pi,1}$  is less than  $V_{\pi,2}$  ( $V_{\pi,1} < V_{\pi,2}$ ). As a result, the same voltage change  $\Delta V$  for both of these devices has a larger effect on the transmittance for device 1 when compared to that of device 2 ( $\Delta T_1 > \Delta T_2$ ).

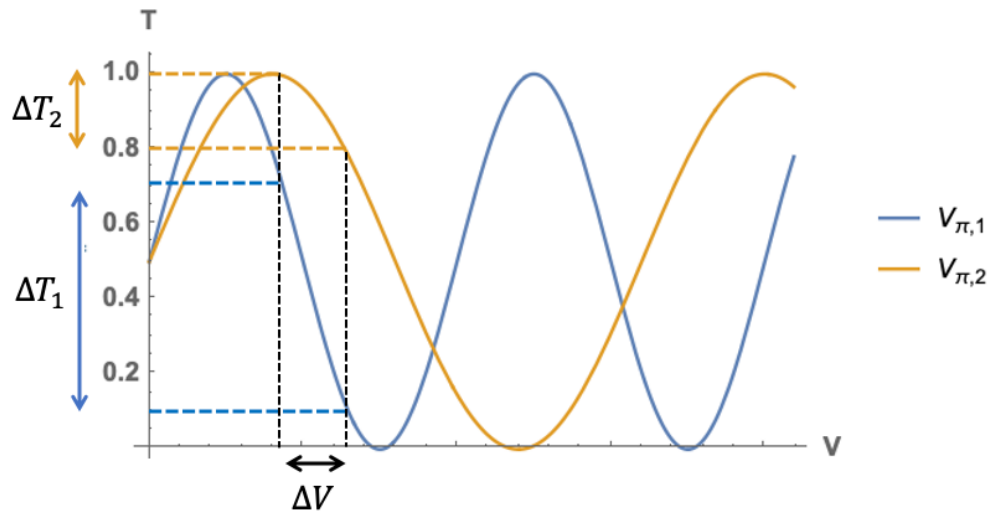


Figure 82. Transmission spectrum versus applied voltage for two devices with varying half-wave voltages ( $V_{\pi,1} < V_{\pi,2}$ ) demonstrates a larger change in transmission for device 1 ( $\Delta T_1 > \Delta T_2$ ) for the same change in voltage ( $\Delta V$ ).

#### 4.6.2.4 Intensity Modulators (Retarder Between Cross Polarizers)

One alternative method to obtain an electro-optic intensity modulator is through the use of a dynamic wave retarder placed between two crossed polarizers as shown in Figure 83a. As described in Section 4.6.2.2, dynamic wave retarders can be used to control the polarization state

of incoming light waves by changing the magnitude of the applied voltage [45]. Therefore, if a dynamic wave retarder is placed between two crossed polarizers whose axes are oriented at 45° with respect to the axes of the retarder, then the power or intensity transmittance of a Pockels cell system is given by

$$T(V) = \sin^2\left(\frac{\Gamma_{\text{Pockels}}(V)}{2}\right) = \sin^2\left(\frac{\Gamma_0}{2} - \frac{\pi}{2} \frac{V}{V_{\pi, \text{Pockels}}}\right) \quad (52)$$

where  $V_{\pi, \text{Pockels}}$  is represented by Equation 52. Figures 83b and 83c illustrate the overall transmittance of the Pockels-based wave retarder intensity modulator as a function of the phase retardation and applied voltage, respectively.

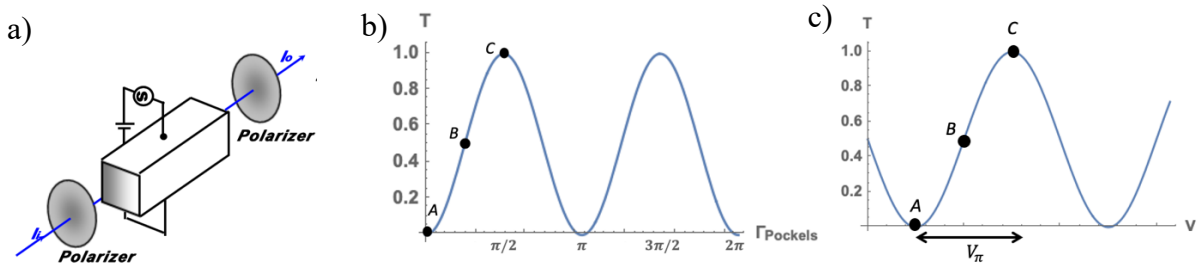


Figure 83. a) Wave retarder intensity modulator composed of a nonlinear cell placed between two crossed polarizers [45]. Transmission spectrum versus b) phase retardation and c) applied voltage demonstrates a linear response around point B and/or optical switch capabilities when transitioning from points A to C.

Similar to the interferometric intensity modulators above, it is desirable to minimize the half-wave voltage such that the period of transmittance oscillation occurs over a smaller voltage range and the slope of the linear region around point B increases to maximize the device sensitivity. Devices with smaller  $V_{\pi}$  parameters can achieve larger intensity changes for the same change in voltage, which improves the control of the device and the detection capabilities. This relationship is illustrated by Figure 84 below, in which  $V_{\pi,1}$  is less than  $V_{\pi,2}$  ( $V_{\pi,1} < V_{\pi,2}$ ). For the same voltage change  $\Delta V$  in each of these devices, device 1 demonstrates a larger change in transmittance when compared to that of device 2 ( $\Delta T_1 > \Delta T_2$ ).

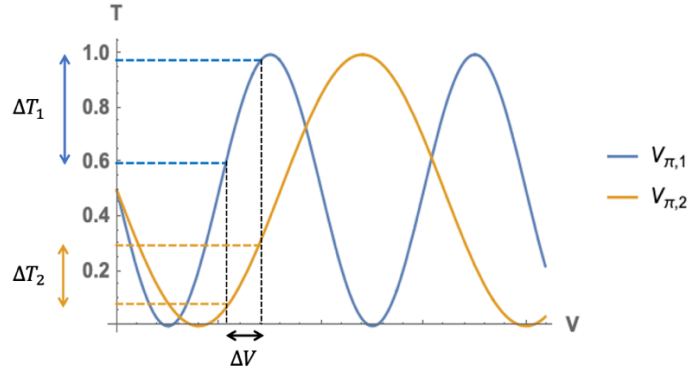


Figure 84. Transmission spectrum versus applied voltage for two wave retarder intensity modulators with varying half-wave voltages ( $V_{\pi,1} < V_{\pi,2}$ ) demonstrates a larger change in transmission for device 1 ( $\Delta T_1 > \Delta T_2$ ) for the same change in voltage ( $\Delta V$ ).

This example illustrates the operation of a Pockels cell intensity modulator, but similar relationships can be derived for both Kerr and Pockels-Kerr modulators by modifying Equation 52 accordingly. For a Kerr cell wave retarder intensity modulator, the transmittance is given by Equation 53 below which is further explained by Figure 85. Unlike the Pockels-based system, the transmittance period of oscillation decreases with increasing voltage for Kerr cell wave retarder intensity modulators. Therefore, unless the system is operating within a limited voltage range, these Kerr-based devices can be more difficult to predict and control when compared to equivalent Pockels cell devices.

$$T(V) = \sin^2 \left( \frac{\Gamma_{\text{Kerr}}(V)}{2} \right) = \sin^2 \left( \frac{\Gamma_0}{2} - \frac{\pi}{2} \left( \frac{V}{V_{\pi, \text{Kerr}}} \right)^2 \right) \quad (53)$$

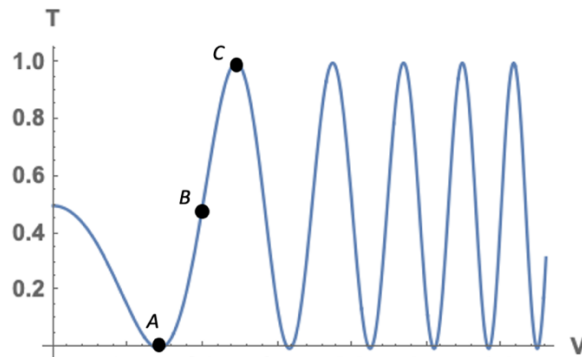


Figure 85. Transmission spectrum for a Kerr cell wave retarder intensity modulator versus applied voltage demonstrates a linear response around point B and/or optical switch capabilities when

transitioning from points A to C, with an oscillation period that decreases with increasing applied voltage.

While it is important to consider and minimize the operating voltage of electro-optic modulator devices, there are also other performance metrics such as the bandwidth, operating speed, extinction ratio, and fabrication costs or challenges that should be considered when designing these devices. The extinction ratio is the ratio between the maximum and minimum transmittance, which is always less than unity due to losses caused by reflection, absorption, and scattering, as well as misalignments of the directions of propagation and polarization with respect to the crystal axes and polarizer orientations. However, current devices have demonstrated extinction ratios greater than 30 dB with optimized designs that minimize each of these loss contributions.

#### 4.6.3 Nonlinear Materials Evaluation for Photonic Integrated Circuits

The previous sections of this paper have focused on the theory of electro-optic modulation and the most common types of electro-optic modulators that are currently used in optical devices. The unique electro-optic and non-linear properties of these materials dictate the ultimate performance of the resulting devices, such as the operating voltage, bandwidth, dynamic range, and operating speed. While there are several materials currently used for nonlinear devices including Gallium Arsenide (GaAs), Indium Phosphide (InP), Lithium Niobate ( $\text{LiNbO}_3$ ), and Magnesium Fluoride ( $\text{MgF}_2$ ), each with their own benefits, there are also many drawbacks that have prevented the widespread implementation of these materials for integrated nonlinear devices.

Lithium Niobate crystals are mainly used to make high-performance electro-optic modulators with high modulation bandwidth and good modulation linearity. However, the associated processing technology is complicated, which has prevented the practical application of  $\text{LiNbO}_3$  for large-scale photonic integrated circuits [53-54]. Gallium Arsenide materials can be used for active optoelectronic devices, but they are limited to operation in the 850 nm wavelength range because of its intrinsic bandgap. Therefore, active optical devices with GaAs materials are only applicable to local area networks and cannot be applied to the desirable 1310 and 1550nm long-range fiber-optic communication wavelengths [55]. Alternatively, Indium Phosphide can be used to simultaneously integrate active and passive optical devices at an operating wavelength around 1310 nm and 1550 nm, which is ideal for optical communications. However, despite these

desirable material properties, InP devices are not CMOS-compatible and consequently require dedicated fabrication that will never reach the versatility and economy of CMOS fabrication facilities. There are also numerous yield-related problems associated with the wafer-bonding approach that is currently used for InP layers grown via Molecular Beam Epitaxy (MBE), which limit its potential for large-scale integration. Furthermore, InP generally has higher loss values when compared to other materials, and its nonlinear optical properties are inadequate for several key applications [56]. Finally, Magnesium Fluoride has recently been introduced as a nonlinear material for RF/microwave photonics. The fundamental problem of monolithic integration using MgF<sub>2</sub> is that waveguides made of this material cannot guide light on a Si-CMOS platform due to its low refractive index of  $n_0 = 1.38$ , compared to the refractive indices of conventional Si-CMOS cladding materials, SiO<sub>2</sub> ( $n = 1.45$ ) or SiN ( $n = 2$ ). MgF<sub>2</sub> is also only available in crystal formats, which further complicates its scaling, fabrication, and integration with electronics.

As evidenced by the discussion above, each of these nonlinear materials suffers from some limitations with regards to fabrication, operating wavelength range, waveguide loss, efficiency, and more. ZnTe demonstrates exceptional non-linear properties and has the potential to satisfy the fabrication, bandwidth, and low voltage requirements of on-chip integrated devices. The ALD growth of ZnTe at low temperatures will circumvent the current complexities of fabrication with LiNbO<sub>3</sub>, as well as the challenges of wafer bonding techniques associated with InP and GaAs-based photonic integrated circuits [57-58]. Additionally, based on its superior electro-optic properties, it is anticipated that integrated ZnTe modulators can achieve large bandwidths of >35 GHz. In order to evaluate the potential of this new material system, the following section will compare the proposed design and performance of integrated ZnTe electro-optic phase modulators to that of the leading LiNbO<sub>3</sub> modulators.

As described in [Section 3.1](#), waveguide-integrated electro-optic modulators benefit from the ability to design devices that minimize the electrode separation distance ( $d$ ) with respect to the propagation length ( $L$ ), consequently decreasing the  $d/L$  ratio and minimizing the applied voltage requirements. Wang et al. (2018) recently demonstrated high-performance, integrated LiNbO<sub>3</sub> electro-optic modulators operating at very low, CMOS-compatible voltages. Figure 86a below illustrates the novel fabricated photonic chip of these LiNbO<sub>3</sub> modulators, consisting of three Mach-Zehnder electro-optic phase modulators with various device lengths. The inset in the bottom

right corner shows the cross-sectional schematic of the nanophotonic  $\text{LiNbO}_3$  (LN) modulator with the metal electrode contacts (labeled G and S for ground and signal, respectively) placed between the LN waveguides. The LN waveguides are approximately 600nm tall and 600nm wide, with an electrode separation distance ( $d$ ) of roughly 5.5um. This structure was tested for three different optical path lengths of 20, 10, and 5mm and successfully demonstrated low half-wave operating voltages of 1.4, 2.3, and 4.4 Volts, respectively. These results are shown in Figures 86b-d below, which plot the normalized transmission spectra versus the applied voltage.

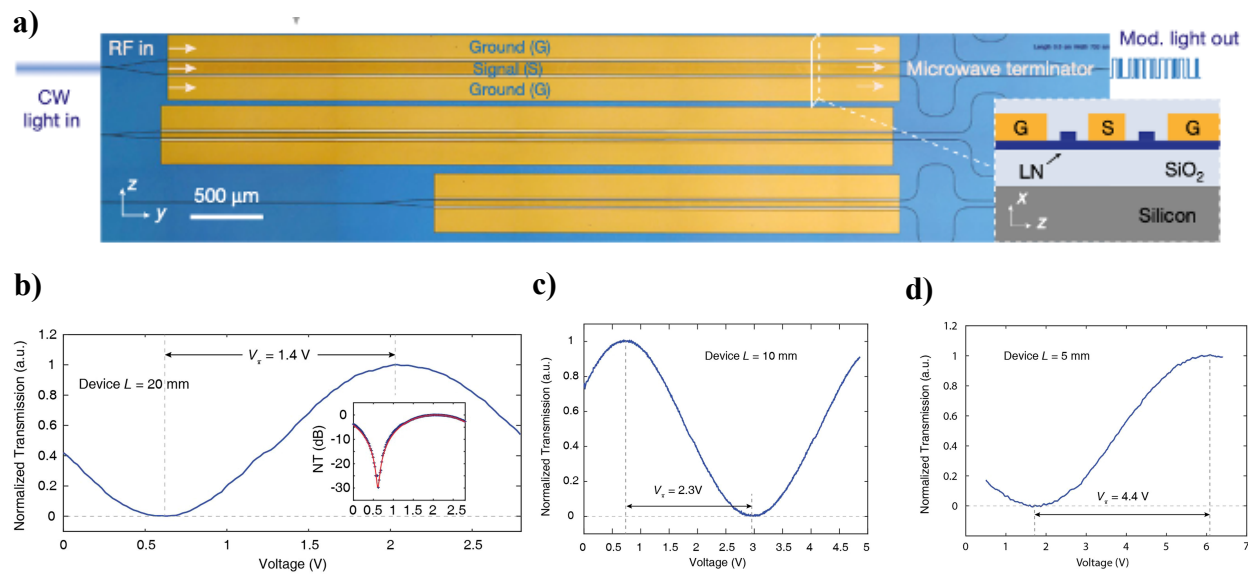


Figure 86. a) “Microscope image of the fabricated chip consisting of three Mach–Zehnder modulators with various microwave signal line widths and device lengths. The thin-film configuration allows for maximum field overlap and velocity matching between microwave and optics. Inset shows the cross-sectional schematic of the nanophotonic LN modulator” [59]. Normalized transmission versus applied voltage for integrated LN electro-optic modulators with b)  $L = 20\text{mm}$ , c)  $L = 10 \text{ mm}$ , and d)  $L = 5 \text{ mm}$ .

While this design has successfully demonstrated integrated electro-optic modulation within a low, CMOS-compatible voltage range, the fabrication of these devices still remains a challenge. These devices were fabricated by bonding a single-crystal  $\text{LiNbO}_3$  thin film onto a  $\text{SiO}_2$  substrate, and then etching this wafer to obtain the desired waveguide structure. Due to the high cost of single-crystal  $\text{LiNbO}_3$  thin films and the many challenges associated with wafer bonding techniques, these devices are not yet capable of large-scale production. Therefore, alternative solutions such

as ZnTe electro-optic phase modulators are still necessary to fulfill these requirements of integrated nonlinear devices.

To compare these experimental LiNbO<sub>3</sub> results to the proposed ZnTe electro-optic phase modulators, a numerical model was developed using the equations previously derived in Sections 3.1 and 3.3. The accuracy and validity of this model was first confirmed by inputting the device design and material parameters of the LiNbO<sub>3</sub> modulator above and then comparing the computational and experimental half-wave voltage values. Table 14 below demonstrates less than twenty percent error when comparing the experimentally-reported and computational V<sub>π</sub> values, which suggests that this model can be applied to different material systems with relative accuracy.

Table 14. Comparison of the experimentally-reported and computed V<sub>π</sub> values for three LiNbO<sub>3</sub> modulators.

Refractive Index of LiNbO <sub>3</sub>	LiNbO <sub>3</sub> Pockels Coefficient, r (pm/V)	LiNbO <sub>3</sub> Kerr Coefficient, s (cm <sup>2</sup> /W)	Electrode Separation, d (um)	Length, L (mm)	Experimentally Reported V <sub>π</sub> (V)	Computational V <sub>π</sub> (V)	Percent Error (%)
2.21	30	3.8x10 <sup>-15</sup>	5.5	20	1.4	1.312	6.286
2.21	30	3.8x10 <sup>-15</sup>	5.5	10	2.3	2.619	13.87
2.21	30	3.8x10 <sup>-15</sup>	5.5	5	4.4	5.203	18.25

In addition to the desirable nonlinear properties of ZnTe, this novel ALD method enables the fabrication of conformal layers with very high aspect ratios. As a result, this technique can be leveraged to produce structures that minimize the electrode separation distance (d), consequently decreasing the d/L ratio and the resulting half-wave voltage. Figure 87a below illustrates a cross-sectional schematic of the proposed ZnTe-filled Silicon Nitride (SiN) slot waveguide, which could be fabricated using the ALD technique. This waveguide structure consists of two parallel SiN waveguides (400 nm thick and 200 nm wide) with a 100 nm gap filled by the conformal ZnTe coating. The metal electrode contacts are deposited on top of the structure with 100 nm separation in order to maximize the magnitude of the applied electric field. Figure 87b illustrates a Lumerical model simulation of the electric field profile, which has revealed high optical confinement within

the ZnTe slot due to its high refractive index compared to that of SiN ( $n = 2.86$  and  $2.45$  for ZnTe and SiN, respectively).

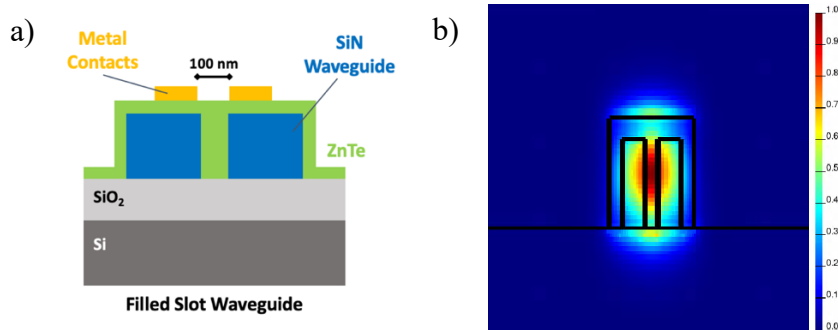


Figure 87. a) Cross-sectional schematic of the proposed ZnTe-filled Silicon Nitride (SiN) slot waveguide structure composed of two 400 nm tall x 200 nm wide SiN waveguides with a 100 nm Zn-Te filled gap. b) Lumerical simulation of the electric field profile demonstrates high confinement within the 100 nm thick ALD ZnTe slot layer.

Based on this integrated modulator design, the material parameters and corresponding dimensions can be applied to compute the expected half-wave voltage for the ZnTe-based electro-optic phase modulator. The material parameters, device dimensions, and resulting  $V_{\pi}$  are shown in Table 15 below for three different propagation lengths (20, 10, and 5 mm) as well as two different electrode separation distances of 100 nm and 5.5  $\mu\text{m}$  for comparison with the LiNbO<sub>3</sub> modulator. As demonstrated by these results, ZnTe-based modulators with 100 nm electrode separation distance have the potential to realize operating voltages nearly two orders of magnitude lower than that of the optimized LiNbO<sub>3</sub> modulator. Furthermore, ZnTe modulators still exhibit operating voltages nearly half as large as those of the optimized LiNbO<sub>3</sub> modulator for the same electrode separation distance of 5.5  $\mu\text{m}$ .

Table 15. Comparison of the computed  $V_{\pi}$  values for ZnTe and LiNbO<sub>3</sub> modulators with varying electrode separation and propagation lengths.

Refractive Index of ZnTe	ZnTe Pockels Coefficient, $r$ (pm/V)	ZnTe Kerr Coefficient, $s$ ( $\text{cm}^2/\text{W}$ )	Electrode Separation, $d$ (nm)	Length, $L$ (mm)	Experimentally Reported $V_{\pi}$ for LiNbO <sub>3</sub> (V)	Computational $V_{\pi}$ for ZnTe (V)
2.86	4.3	$8 \times 10^{-13}$	100	20	--	0.0178
2.86	4.3	$8 \times 10^{-13}$	100	10	--	0.0262

2.86	4.3	$8 \times 10^{-13}$	100	5	--	0.0381
2.86	4.3	$8 \times 10^{-13}$	5.5 um	20	1.4	0.9811
2.86	4.3	$8 \times 10^{-13}$	5.5 um	10	2.3	1.4419
2.86	4.3	$8 \times 10^{-13}$	5.5 um	5	4.4	2.0955

A more comprehensive analysis of these results is given by Figures 88a-c below, which plot the  $V_{\pi}$  values of these material systems for various propagation lengths. For the same electrode separation distance of 5.5 um for both LiNbO<sub>3</sub> (LNO) and ZnTe, Figure 88a reveals that the half-wave voltage of LNO is generally much larger than that of ZnTe for shorter propagation lengths (larger d/L). However, upon further inspection in Figure 88b at this fixed electrode separation of 5.5 um, it is evident that LNO achieves lower  $V_{\pi}$  values for propagation lengths greater than 39.9 mm. While this is a promising result for LNO-based modulators, increasing the propagation length can lead to higher loss values that ultimately limit the performance of these devices. Therefore, Figure 88c highlights the potential of ZnTe ALD modulators, which can be fabricated with a much smaller electrode separation of 100 nm (as represented by the yellow line). This unique design enables very low operating voltages with much shorter propagation lengths, which make this a very promising and competitive system for future CMOS-compatible integrated electro-optic modulators.

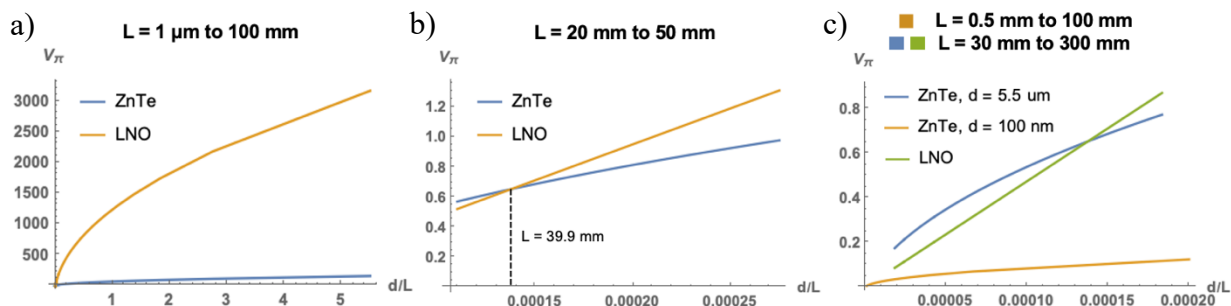


Figure 88. Half-wave voltage versus  $d/L$  ratio for ZnTe and LNO electro-optic phase modulators with a fixed electrode separation of  $d = 5.5$  um and varying propagation length between a) 1 um to 100 mm and b) 20 mm to 50mm. c) Half-wave voltage versus  $d/L$  ratio with a fixed electrode separation of  $d = 5.5$  um and varying propagation length between 30 mm to 300 mm for ZnTe (blue) and LNO (green) electro-optic phase modulators compared to that of a ZnTe phase

modulator with 100nm electrode separation and varying propagation length between 0.5 mm to 100 mm (yellow).

This superior performance of ZnTe devices is partially due to the fact that ZnTe benefits from both the Pockels and Kerr nonlinear effects, while LiNbO<sub>3</sub> is primarily a Pockels-based material with negligible third-order Kerr nonlinearities. Figures 89a-c illustrate the half-wave voltages for LiNbO<sub>3</sub> devices with 10 um electrode separation and varying propagation length between 50um up to 200 mm. Due to the relatively small Kerr coefficient, the resulting V<sub>π</sub> requirements for a LiNbO<sub>3</sub> device solely relying on the Kerr effect (yellow line) are much greater than that of a device primarily utilising the Pockes effect (blue line) as shown in Figure 89a. While this plot demonstrates that the Kerr effect can dominate at shorter propagation lengths (larger d/L), this is generally not observed in practical devices which employ longer propagation lengths to minimize the operating voltage requirements. Therefore, Figures 89b and c illustrate the same relationship over a restricted propagation length regime spanning 10 to 100 mm, where the Pockels effect clearly dominates to achieve much lower V<sub>π</sub> values than the Kerr effect. Furthermore, Figure 89c has removed the Kerr effect contribution to closely examine the relationship between the Pockels and P-K V<sub>π</sub> values computed using Equations 33 and 38, respectively. As expected, these two components are nearly indistinguishable, which confirms that LiNbO<sub>3</sub> modulators can be modeled as solely Pockels-based materials with negligible contributions from third-order Kerr nonlinearities in the relevant operating regime.

In contrast to LiNbO<sub>3</sub>, ZnTe has moderate Pockels and Kerr coefficients which both contribute to the observable nonlinearities in electro-optic modulator devices. Figures 89d-f above illustrate the half-wave voltages for ZnTe devices with 10 um electrode separation and varying propagation length between 50um up to 200 mm. Unlike the LiNbO<sub>3</sub> devices, the Kerr effect dominates across this operating regime, resulting in lower V<sub>π</sub> requirements for a ZnTe device solely relying on the Kerr effect (yellow line) compared that of a device primarily utilizing the Pockes effect (blue line) as shown in Figure 89d. Figures 89e and f illustrate the same relationship over a restricted propagation length regime spanning 10 to 100 mm, while Figure 89e has removed the Pockels effect contribution to closely examine the relationship between the Kerr and P-K V<sub>π</sub> values computed using Equations 35 and 38, respectively. This final result reveals a nearly 0.5V difference between the Kerr and P-K V<sub>π</sub> values, which confirms that ZnTe modulators benefit from

both Pockels second-order and Kerr third-order nonlinearities in the relevant operating regime to achieve low voltage requirements when compared to other nonlinear materials.

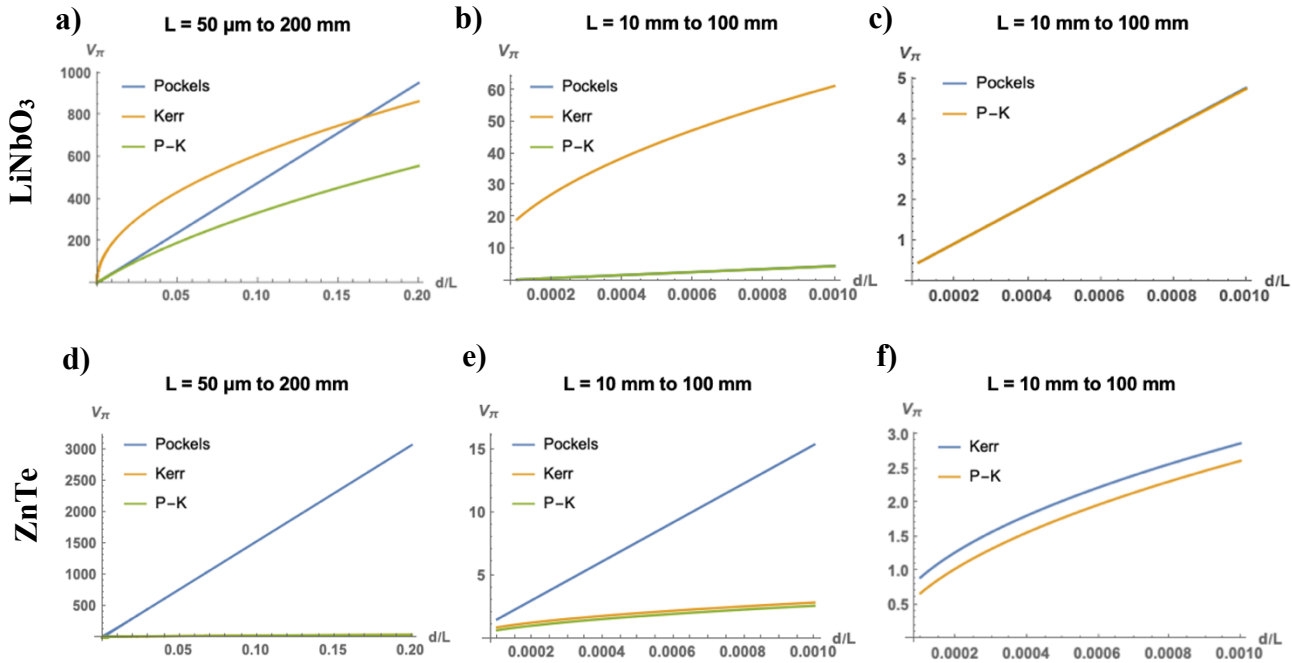


Figure 89. Half-wave voltage versus  $d/L$  ratio for LNO electro-optic phase modulators with a fixed electrode separation of  $d = 10 \mu\text{m}$  and varying propagation length between a) 50  $\mu\text{m}$  to 200  $\mu\text{m}$ , and b), c) 10 mm to 100mm. Half-wave voltage versus  $d/L$  ratio for ZnTe electro-optic phase modulators with a fixed electrode separation of  $d = 10 \mu\text{m}$  and varying propagation length between d) 50  $\mu\text{m}$  to 200  $\mu\text{m}$ , and e), f) 10 mm to 100mm.

#### 4.6.4 Conclusion

Electro-optic modulators are essential components in modern telecommunication networks and microwave-photonic systems due to their ability to translate high-speed electronic signals into the optical domain. These essential applications require integrated, chip-scale electro-optic modulators with low voltage requirements, low losses, and simple fabrication techniques that are compatible with current CMOS technology. Previous integrated modulator material platforms such as silicon, indium phosphide, and polymers limited intrinsic nonlinear properties, while alternative material systems such as lithium niobate ( $\text{LiNbO}_3$ ) require complex fabrication techniques to accomplish on-chip integration [59].

Zinc Telluride (ZnTe) demonstrates considerable non-linear properties (large Pockels and Kerr coefficients) compared to the traditional nonlinear materials such as LiNbO<sub>3</sub>, GaAs and InP. Since ZnTe benefits from both second-order Pockels or third-order Kerr effects, it is capable of achieving a strong nonlinear response with very low operating voltages. Recent Atomic Layer Deposition (ALD) fabrication innovations have enabled epitaxial growth of ZnTe at low temperatures, which enable direct growth and monolithic integration of ZnTe on current CMOS circuitry. Furthermore, this novel ALD method can fabricate very high aspect ratio, conformal coatings, which can be used to produce optimized device designs with minimal the electrode separation distances and thus very low operating voltages for integrated ZnTe electro-optic modulators. Based on these properties, ZnTe devices present a very promising and competitive system for future CMOS-compatible integrated electro-optic modulators. Future work will demonstrate these devices experimentally and provide an opportunity to characterize and optimize the operating bandwidth, speed, and extinction ratios of these devices.

## 5 Ge Waveguides for MIR PICs

Three different germanium-based waveguiding systems, including germanium-on-silicon, germanium-on-silicon nitride, and germanium-on-silicon nitride with a nitride capping layer, are demonstrated and characterized for midinfrared wavelengths between 2.3  $\mu\text{m}$  and 3.2  $\mu\text{m}$ . Several different waveguide widths were designed and fabricated to compare propagation losses for both TE and TM modes across all material platforms. Simulations were performed in conjunction with the experimental measurements to optimize the optical mode properties and confirm the propagation loss results for the various material platforms. At the mid-infrared wavelength of 2.3  $\mu\text{m}$ , the germanium-on-silicon nitride with nitride capping layer achieved the lowest propagation losses, as low as 1.66 dB/cm for a 2.5  $\mu\text{m}$  wide waveguide. These germanium-on-silicon nitride waveguides with a nitride cap also achieved the highest transmission compared to the other material platforms at longer wavelengths up to 3.2  $\mu\text{m}$ . These platforms are promising candidates for integrated mid-infrared sensors, enabling diverse applications in chemistry, biology and health sciences.

## 5.1 Introduction

The mid-infrared (MIR) region of the electromagnetic spectrum (2 to 20  $\mu\text{m}$ ) has garnered immense interest for use in spectroscopic systems such as sensing and forensic analysis. The absorption peaks of many chemicals, resulting from the excitation of rotational and vibrational energy levels of these target molecules, are present in this wavelength range [60-62]. The Silicon-on-Insulator (SOI) material platform has dominated near-infrared (near-IR) integrated photonics due to its high transparency and refractive index contrast that enables low loss propagation with high mode confinement and tight bends. However, recent integrated photonics research has focused on extending the operating region of conventional SOI devices to the MIR for sensing applications [63-65]. One of the key challenges for MIR photonics using standard SOI structures is that the underlying oxide layer suffers from high absorption loss in the MIR region ranging from 2.6 to 2.9  $\mu\text{m}$  and beyond [66]. One current alternative is to utilize Silicon-on-Nitride (SON) waveguides where the buried silicon dioxide layer is replaced with a silicon nitride layer to achieve lower losses and low chromatic dispersion in the MIR region from 2.43 to 6.63  $\mu\text{m}$  [67].

In addition to these Si-based waveguiding platforms, germanium (Ge) is a promising group IV material for MIR photonics [68]. Ge-on-Si (GOS) waveguides have previously been fabricated and have demonstrated low propagation losses of 2.5 dB/cm at 5.8  $\mu\text{m}$  wavelength [69]. Nedeljkovic, et al. also characterized GOS waveguides with a minimum propagation loss of 2.5 dB/cm at 7.57  $\mu\text{m}$  wavelength [70]. Kah-Wee Ang and his group measured Ge-on-SOI waveguides at 3.68  $\mu\text{m}$  wavelength and reported a minimum propagation loss of 8 dB/cm for 0.85  $\mu\text{m}$  thick by 6.5  $\mu\text{m}$  wide waveguides [71]. K. Gallacher, et al. reported propagation losses of 5 dB/cm for both transverse electric (TE) and transverse magnetic (TM) polarizations for GOS waveguides in the MIR region with wavelengths ranging from 7.5 to 11  $\mu\text{m}$  [72].

These initial results demonstrate GOS as a promising waveguiding platform for MIR photonic devices due to its wider transparency range from 2 to 15  $\mu\text{m}$  compared to traditional SOI with similar, low propagation losses (down to a minimum of 0.6 dB/cm at 3.8  $\mu\text{m}$  wavelength) [73-75]. However, while GOS offers many advantages in extending the wavelength range of these devices, the minimum waveguide bend radius of GOS waveguides is higher than that of SOI. This is due to the lower refractive index ( $n$ ) contrast between the waveguide core and substrate for GOS

$(\Delta n_{GOS} = 0.63)$  compared to SOI ( $\Delta n_{SOI} = 2.01$ ) [76]. To achieve wide range MIR transparency with low loss and compact devices using smaller waveguide bending radii, Germanium on Silicon Nitride (also called Ge on SiN or Ge-on-Nitride (GON)) is a viable material platform due to its higher refractive index contrast ( $\Delta n_{GON} = 1.5$ ). C. S. Tan and his group reported GON waveguides with a propagation loss of  $3.35 \text{ dB/cm}$  and a bending loss of  $0.41 \text{ dB/bend}$  for TE modes at  $3.8 \mu\text{m}$  wavelength [77]. Reducing the bending radius and loss is essential to fabricate compact, efficient, and high-performance MIR sensing devices which often rely on structures like ring resonators and spiral waveguides with several bends as shown in Figure 90.

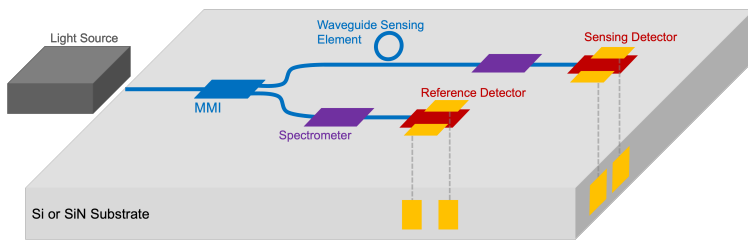


Figure 90. Schematic diagram of a ratiometric MIR sensing device integrated with underlying readout electronic circuitry.

This work demonstrates a comparative study between three different material platforms including: (i) Ge on Si (GOS) where Floatzone Si is used to minimize typical oxide absorption losses that come from standard Czochralski Si, (ii) Ge on SiN (GON), and (iii) Ge on SiN with a  $10 \text{ nm}$  thick SiN cap (GONN). The propagation losses of each material platform were measured for various waveguide widths for wavelengths ranging from  $2.36$  to  $3.16 \mu\text{m}$ . Across all wavelengths and waveguide widths, the GONN waveguides consistently yielded the lowest propagation losses, with a minimum of  $1.66 \text{ dB/cm}$  for a  $2.5 \mu\text{m}$  wide waveguide measured at  $2.3 \mu\text{m}$  wavelength.

## 5.2 Sample Design and Experimental Setup

A systematic study of propagation loss in the MIR region has been performed for GOS, GON and GONN platforms, with varying waveguide widths ranging from  $1.0$  to  $2.5 \mu\text{m}$ . The GOS material platform utilized a  $1.3 \mu\text{m}$  thick Ge core waveguide on a Si substrate, while the GON devices used the same  $1.3 \mu\text{m}$  Ge core on a  $2.0 \mu\text{m}$  thick SiN layer separated from the underlying Si wafer by a  $50 \text{ nm}$  thick SiO<sub>2</sub> layer. The GONN waveguides adopted the same substrate configuration as the GON devices with a thicker  $2.1 \mu\text{m}$  Ge core and a  $10\text{nm}$  SiN capping layer surrounding the final

waveguides. All of these Ge waveguides were fabricated at CEA-Leti as described in a previous work to create several sets of waveguide paperclips with fixed width and 6 different lengths. Figure 91a-c shows cross-sectional Scanning Electron Microscopy (SEM) images of the fabricated waveguides with the corresponding thicknesses [78]. For each platform, the waveguide design consists of several sets of 6 paperclips with a fixed width and increasing relative propagation lengths (compared to paperclip 1) of 157  $\mu\text{m}$ , 614  $\mu\text{m}$ , 1614  $\mu\text{m}$ , 2614  $\mu\text{m}$ , 5114  $\mu\text{m}$ , and 7114  $\mu\text{m}$  as shown in Figure 91d. Each of these paperclips contains the same number of bends ( $R = 50 \mu\text{m}$ ) to normalize the comparative measurement results within each waveguide set of constant width. Additionally, these paperclip bends eliminate any higher order waveguide modes and introduce a constant 200  $\mu\text{m}$  offset between the waveguide input and output to improve the measurement accuracy by reducing the collection of any stray light from the laser source.

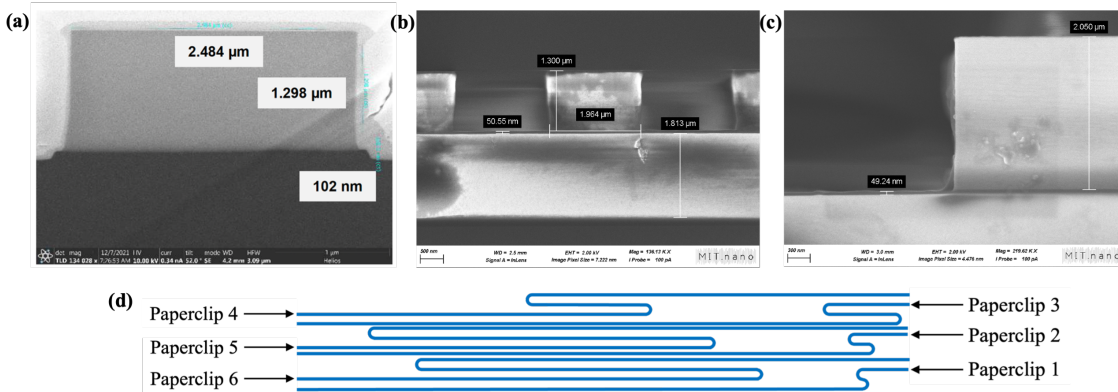


Figure 91. Cross-sectional SEM images of the a) GOS, b) GON, and c) GONN waveguides. d) Waveguide design with 6 paperclips of increasing relative lengths from 157  $\mu\text{m}$  to 7114  $\mu\text{m}$ . The relative transmission of all paperclips was measured with respect to the shortest paperclip 1 to extract the propagation loss for different platforms and waveguide dimensions. The GONN platform exhibited the lowest propagation loss of 1.66 dB/cm for the largest 2.5  $\mu\text{m}$  wide waveguide.

The waveguide propagation loss measurements were performed on an optical bench using a tunable MIR laser (Firefly M-Squared Laser; wavelength tunable from 2.3 – 3.8  $\mu\text{m}$  with 5 nm linewidth) modulated with a chopper at 1 kHz and edge-coupled into the input waveguide via an aspheric lens. Waveguide alignment was achieved by coupling the output waveguide signal through a CaF<sub>2</sub> lens to a cryogenically-cooled InSb focal plane array MIR camera to visualize the

optical mode. A MIR HgCdTe photodetector (VIGO Photonics PVMI-4TE) was then aligned to the waveguide output and the resulting voltage signal was passed to a lock-in amplifier (Stanford Research Systems SR810) synchronized with the modulation frequency of the chopper as shown in Figure 92. These measurements were repeated for each of the 6 paperclips in a given fixed waveguide width set to determine the propagation losses for each system.

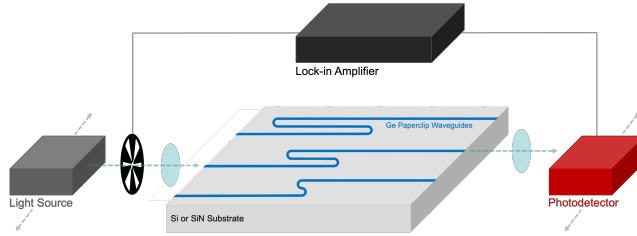


Figure 92. Schematic of the experimental setup for MIR propagation loss measurements with the incoming light from the laser source passing through a mechanical chopper and aspheric lens before coupling into the Ge paperclip waveguides. The output signal is focused through a  $\text{CaF}_2$  lens onto the photodetector and routed to a lock-in amplifier synchronized with the chopper frequency for electronic readout. After each measurement, the chip is moved on a translation stage to realign to the next paperclip.

In addition to this initial study of the waveguide propagation losses as a function of waveguide width for different platforms, the transmission loss was also evaluated as a function of wavelength. For these measurements, the laser input was aligned to the shortest paperclip starting at a wavelength of  $2.36 \mu\text{m}$ . While maintaining this optimized alignment to the shortest paperclip waveguide, the wavelength of the input laser source was then varied between  $2.36 \mu\text{m}$  to  $3.16 \mu\text{m}$ .

### 5.3 Results and Discussion

After measuring the optical output for each of the paperclip waveguides for a given material platform, the relative transmission (RT) was calculated according to Equation 54, where  $V_n$  and  $V_1$  are the measured photodetector voltages of the  $n^{\text{th}}$  paperclip and paperclip 1, respectively (for  $n = 1$  to 6). These measurements were repeated for 5 different waveguide widths of 1.0, 1.1, 2.3, 2.4, and  $2.5 \mu\text{m}$  at a fixed laser wavelength of  $2.36 \mu\text{m}$  for each platform to evaluate the effect of varying waveguide width on the overall propagation losses.

$$RT(\text{dB}) = 20\log[V_n/V_1] \quad (54)$$

As expected, the RT decreases with paperclip length since the overall power loss is directly proportional to the length of the waveguide times the linear propagation loss. The bending losses remain constant for all measurements within each waveguide set as each paperclip contains the same number of bends and bending radii to enable extraction of the linear propagation loss alone. By applying a linear fit to these measurements, the propagation loss ( $\alpha$ ) was extracted from the slope and consistently decreased with increasing waveguide width for all platforms ( $\alpha_{1.0} > \alpha_{1.1} > \alpha_{2.3} > \alpha_{2.4} > \alpha_{2.5}$ ) as shown in Table 16. The standard error was evaluated from three repeated measurements of each waveguide to improve the accuracy of these results. These experimental results confirm the expected behavior as losses due to sidewall scattering increase in narrower waveguides when the optical mode is less confined and the evanescent field interaction with the waveguide sidewalls increases [79-80]. This expectation of reduced scattering loss from sidewall roughness can be inferred from the Ansys Lumerical MODE simulations in Figure 93 that demonstrate decreasing evanescent field with increasing waveguide width.

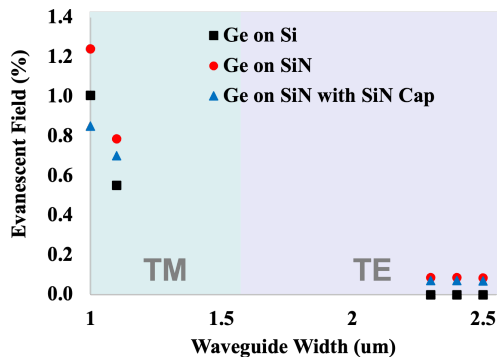


Figure 93. Simulation results of the evanescent field for each material platform as a function of waveguide width demonstrate decreasing evanescent field with increasing width. As a result, the experimental propagation loss also decreases for wider waveguides for all material platforms due to reduced sidewall scattering.

In addition, a comparative study of propagation losses for the three platforms is shown in Figure 94a. For the narrower waveguide widths of 1.0 and 1.1  $\mu\text{m}$ , the losses are dominated by interactions with the sidewall and scattering due to roughness. Since the GON waveguides demonstrate the highest evanescent field in the mode simulations shown in Figure 94d, it follows that the GON

waveguides exhibit the highest experimental propagation loss for the narrower waveguides due to lower waveguide mode confinement and increased sidewall interactions.

Table 16. Propagation loss (dB/cm) with standard errors for varying waveguide widths across three different material platforms (GOS, GON, and GONN) at 2.36  $\mu\text{m}$  wavelength.

Waveguide Width ( $\mu\text{m}$ )	2.5	2.4	2.3	1.1	1.0
GOS	$5.76 \pm 0.1$	$6.82 \pm 0.14$	$9.11 \pm 0.03$	$10.7 \pm 0.26$	$16.2 \pm 0.8$
GON	$4.4 \pm 0.3$	$6.05 \pm 0.23$	$12.7 \pm 0.5$	$16.1 \pm 1.52$	$17.3 \pm 1.02$
GONN	$1.66 \pm 0.66$	$4.81 \pm 0.06$	$5.78 \pm 0.7$	$10.5 \pm 0.33$	$16.9 \pm 1.71$

On the other hand, for the waveguides with 2.3, 2.4, and 2.5  $\mu\text{m}$  widths, the evanescent field is very low for all platforms (< 0.5%) leading to minimal sidewall interactions and scattering from roughness. Therefore, the losses for these waveguide dimensions are dominated by radiative bending losses. For all three of these wider waveguide dimensions, GOS demonstrated the highest losses due to the lowest refractive index contrast between the Ge waveguiding material ( $n_{\text{Ge}} = 4.03$  at 2.36  $\mu\text{m}$  wavelength) and the Si substrate ( $n_{\text{Si}} = 3.44$  at 2.36  $\mu\text{m}$  wavelength) compared to GON and GONN material platforms. As a result of this lower refractive index contrast, the optical mode propagates through both the waveguide core and substrate for the GOS platform. Figure 94b-c illustrates the simulated mode profiles for GOS and GONN waveguides of the same 2.3  $\mu\text{m}$  width and clearly illustrates increased mode propagation in the substrate for the GOS waveguides compared to GONN. These simulation results are further summarized in Figures 94d-e and confirm that GOS waveguides have the lowest mode confinement in the Ge core material and the largest substrate propagation of approximately 1.7%. This co-propagation consequently results in the highest propagation losses for GOS compared to GON and GONN waveguides with higher index contrasts.

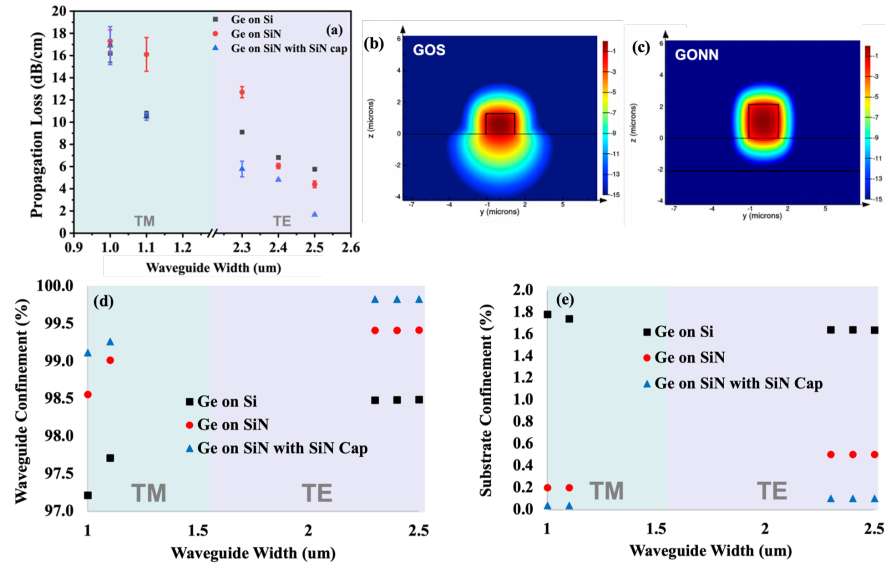


Figure 94. a) Comparative study of the propagation losses as a function of the waveguide width for GOS, GON, and GONN platforms. The error bars were obtained from the standard errors of three repeated measurements as shown in Table 16. Simulation of the fundamental TE mode at 2.36  $\mu\text{m}$  wavelength for a 2.3  $\mu\text{m}$  wide waveguide on a logarithmic scale for the b) GOS and c) GONN platforms. d) Simulation results of the waveguide confinement and e) substrate confinement of the fundamental optical mode as a function of waveguide width. Propagation losses decrease as waveguide width increases due to higher waveguide mode confinement that reduces scattering losses from sidewall interactions. For all graphs, the blue and purple shaded regions indicate fundamental TM and TE modes, respectively.

Finally, for these wider waveguides, the GONN waveguides achieve the lowest propagation losses with a minimum of 1.66 dB/cm for the 2.5  $\mu\text{m}$  waveguide width. The GONN waveguides demonstrate the lowest propagation losses for all of these wider dimensions due to the higher refractive index contrast ( $\Delta_{\text{GON}} = 1.5$ ) compared to GOS combined with the thicker Ge core layer and 10 nm SiN capping layer that further increase the mode confinement. As shown in the simulation results of Figure 5d-e, this waveguide design achieves the highest mode confinement in the Ge core material of 99.8% which therefore reduced sidewall scattering interactions and the lowest amount of light in the Si substrate ( 0.1%), minimizing any radiative losses. In addition, since the GONN waveguides have the thickest Ge waveguide core of 2.1  $\mu\text{m}$  compared to the 1.3

$\mu\text{m}$  thick Ge waveguides of GOS and GON, the GONN waveguide modes are more TM-like which further contributes to a reduction of sidewall interactions.

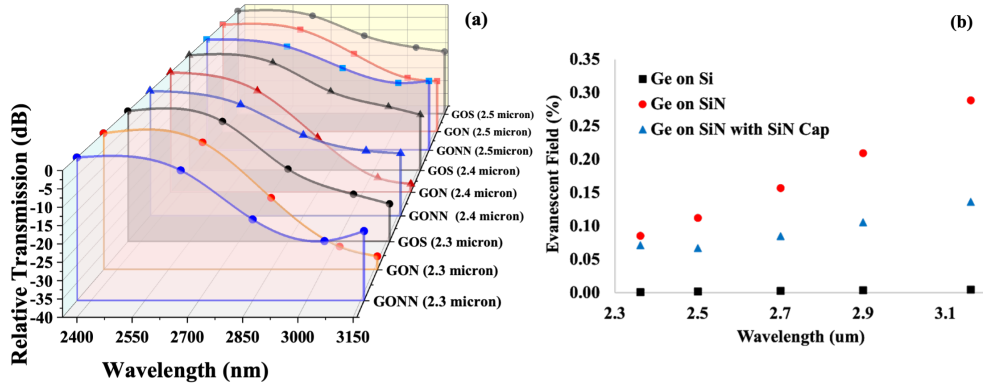


Figure 95. a) Relative transmission as a function of wavelength for GOS, GON and GONN platforms for varying waveguide widths of 2.3, 2.4, and 2.5  $\mu\text{m}$ . b) Simulation results of the waveguide evanescent field as a function of wavelength for a fixed waveguide width of 2.3  $\mu\text{m}$ . Transmission losses increase with wavelength due to increased evanescent field which enhances sidewall scattering interactions and radiative bending losses. GONN exhibits the lowest transmission losses compared to GOS and GON due to the thicker Ge core layer and 10 nm SiN cap which increase the waveguide mode confinement (Figure 94d) and minimize mode co-propagation in the substrate (Figure 94e).

A second study of these waveguides evaluated the transmission loss for each platform as a function of wavelength. The relative power transmission for a given waveguide with different laser wavelengths was calculated according to Equation 54, where  $V_1$  represents the measured photodetector voltage for the shortest wavelength of 2.36  $\mu\text{m}$ , and  $V_n$  denotes the voltages for nth wavelength. Figure 95a illustrates the RT as a function of the input wavelength and clearly indicates an increase in the waveguide transmission loss with increasing wavelength. These higher transmission losses with longer wavelengths likely result from increased sidewall scattering and radiative bending losses due to a reduction in the optical mode confinement. These results are supported by the simulation results shown in Figure 95b which demonstrate an increase in the evanescent field corresponding to a decrease in optical mode confinement with increasing wavelength. The GON waveguides suffer from the highest losses at longer wavelengths, in line with simulation results that demonstrate the sharpest increase in evanescent field for this platform

with increasing wavelength. Furthermore, all platforms demonstrate lower transmission losses at the longer wavelengths for wider waveguides. This is likely due to the increased mode confinement for these larger cross-sectional geometries that consequently minimize sidewall scattering and radiative bending losses. GONN delivered the lowest transmission losses compared to the other material platforms due to the thicker Ge core layer and presence of a 10 nm thick SiN cap which further increased the waveguide mode confinement.

#### 5.4 Conclusion

In summary, a systematic study was performed to evaluate three different Ge waveguide platforms in the MIR wavelength regime. First, five sets of paperclip waveguides with various widths from 1.0 to 2.5  $\mu\text{m}$  were evaluated to determine the propagation losses of TE and TM modes at 2.36  $\mu\text{m}$  wavelength. Across all material platforms, the propagation losses decrease with increasing waveguide width, as expected from simulations, due to increased mode confinement that reduces sidewall interactions and minimizes scattering due to roughness. For the narrower TM mode waveguides, the GON material platform with a 1.3  $\mu\text{m}$  thick Ge core demonstrated the highest propagation losses, which were dominated by sidewall scattering due to the large evanescent field of these waveguide modes. For the wider TE mode waveguides, propagation losses were dominated by radiative bending losses. As a result, the GOS material platform exhibited the highest propagation losses since the low refractive index contrast between the Ge core and Si substrate led to lower confinement in the core material and higher radiative bending losses due to a parasitic co-propagation of the waveguide mode in the Si substrate. Finally, the wider TE mode GONN waveguides exhibited the lowest propagation losses, as low as 1.66 dB/cm for the 2.5  $\mu\text{m}$  wide waveguide, due to the thicker 2.1  $\mu\text{m}$  Ge core and 10 nm SiN capping layer that maximize the mode confinement in the waveguide core, reducing losses due to sidewall scattering or radiative bending losses. In addition to this high performance with low propagation losses, these GONN waveguides would be particularly advantageous for sensing applications as the 10 nm thick SiN capping layer would protect the Ge waveguide core from any undesirable chemical reactions when exposed to the analyte for detection. As a result, these GONN waveguides would enable high quality chemical and biological sensing with long-term durability due to strong resistance to degradation from repeated analyte exposure.

Another study evaluated the waveguide performance as a function of wavelength ranging from 2.36  $\mu\text{m}$  to 3.16  $\mu\text{m}$ . Transmission losses increased with wavelength, in line with simulation results showing reduced mode confinement and consequently increased sidewall scattering interactions and radiative bending losses. GONN exhibited the lowest transmission losses compared to GOS and GON for longer wavelengths due to its larger waveguide core and SiN capping layer that improved mode confinement. This experimental characterization of several Ge-based waveguiding platforms demonstrates their strong potential for integrated mid-infrared sensors for a wide variety of chemical and biological applications.

## References

- [1] A. Vasiliev, M. Muneeb, J. Allaert, J. Van Campenhout, R. Baets, and G. Roelkens, “Integrated silicon-on-insulator spectrometer with single pixel readout for mid-infrared spectroscopy,” *IEEE Journal of Selected Topics in Quantum Electronics*, vol. 24, no. 6, pp. 1–7, 2018.
- [2] L. Tombez, E. J. Zhang, J. S. Orcutt, S. Kamlapurkar, and W. M. J. Green, “Methane absorption spectroscopy on a silicon photonic chip,” *Optica*, vol. 4, no. 11, pp. 1322–1325, 2017.
- [3] P.Su, Z.Han, D.Kita, P.Becla, H.Lin, S.Deckoff-Jones, K.Richardson, L. C. Kimerling, J. Hu, and A. Agarwal, “Monolithic on-chip mid-IR methane gas sensor with waveguide-integrated detector,” *Applied Physics Letters*, vol. 114, no. 5, p. 051103, 2019.
- [4] L. Hong and K. Sengupta, “Fully integrated optical spectrometer in visible and near-IR in CMOS,” *IEEE transactions on biomedical circuits and systems*, vol. 11, no. 6, pp.1176–1191,2017.
- [5] J.H.Correia,G.DeGraaf,M.Bartek, and R.F.Wolffenbuttel, “ACMOS optical microspectrometer with light-to-frequency converter, bus interface, and stray-light compensation,” *IEEE Transactions on Instrumentation and Measurement*, vol. 50, no. 6, pp. 1530–1537, 2001.
- [6] A. Bafeekry, C. Stampfl, and F. M. Peeters, “The electronic, optical, and thermoelectric properties of monolayer PbTe and the tunability of the electronic structure by external fields and defects,” *Physica Status Solidi (b)*, vol. 257, no. 6, p. 2000182, 2020.
- [7] E. Guglielmi, P. Su, F. Zanetto, K. Stoll, S. Serna, G. Ferrari, M. Sampietro, K. Wada, L. C. Kimerling, and A. Agarwal, “1/f noise characteristics of waveguide-integrated PbTe MIR detectors and impact on limit of detection,” *Journal of Lightwave Technology*, vol. 39, no. 22, pp. 7326– 7333, 2021.
- [8] F. Zanetto, E. Guglielmi, F. Toso, R. Gaudiano, F. Caruso, M. Sampietro, and G. Ferrari, “Wide dynamic range multichannel lock-in amplifier for contactless optical sensors with sub-pS resolution,” *IEEE Solid-State Circuits Letters*, vol. 3, pp. 246–249, 2020.
- [9] G. Ferrari, F. Gozzini, A. Molari, and M. Sampietro, “Transimpedance amplifier for high sensitivity current measurements on nanodevices,” *IEEE Journal of Solid-State Circuits*, vol. 44, no. 5, pp. 1609–1616, 2009.

- [10] Hu, J. (2009). Planar chalcogenide glass materials and devices. [Doctoral thesis, Massachusetts Institute of Technology]. MIT DSpace Repository. <https://dspace.mit.edu/handle/1721.1/54562>
- [11] Su, P. (2020). Lead Chalcogenide Thin Film Materials and Processing for Infrared Optical Devices. [Doctoral thesis, Massachusetts Institute of Technology]. MIT DSpace Repository. <https://dspace.mit.edu/handle/1721.1/54562>
- [12] Q. Du et al., “Low-loss photonic device in Ge–Sb–S chalcogenide glass,” Opt. Lett., vol. 41, no. 13, p. 3090, 2016.
- [13] J. Hu et al., “Optical loss reduction in high-index-contrast chalcogenide glass waveguides via thermal reflow,” Opt. Express, vol. 18, no. 2, p. 1469, 2010.
- [14] K. Richardson et al., “Progress on the Fabrication of on-Chip, Integrated Chalcogenide Glass (ChG)-Based Sensors,” J. Nonlinear Opt. Phys. Mater., vol. 19, no. 01, pp. 75–99,128, 2010.
- [15] D. Ahn et al., “High performance, waveguide integrated Ge photodetectors,” Opt. Express, vol. 15, no. 7, p. 3916, 2007. 127
- [16] Z. Han et al., “On-chip chalcogenide glass waveguide-integrated mid-infrared PbTe detectors,” Appl. Phys. Lett., vol. 109, no. 7, p. 071111, 2016.
- [17] V. Singh et al., “Evanescently coupled mid-infrared photodetector for integrated sensing applications: Theory and design,” Sensors Actuators, B Chem., vol. 185, pp. 195–200, 2013.
- [18] Zanetto, F., Stoll, K., Serna, S., Agarwal, A., Sampietro, M., & Ferrari, G. (2023). 6- Channel CMOS-Based Electronic Readout for Optical Absorption Spectroscopy. IEEE Transactions on Biomedical Circuits and Systems.
- [19] Bogaerts, W. (2010) Silicon-on-insulator spectral filters fabricated with CMOS technology. IEEE Journal on Selected Topics in Quantum Electronics, 33.
- [20] Borselli, G. (2005) Beyond the Rayleigh scattering limit in high-Q silicon microdisks: theory and experiment. Optics Express, 1515.
- [21] Gan, X. (2012) A high-resolution spectrometer based on a compact planar two dimensional photonic crystal cavity array. Applied Physics Letters.
- [22] Kita, D. M.; Miranda, B.; Favela, D.; Bono, D.; Michon, J.; Lin, H.; Gu, T.; Hu, J. (2018) High-performance and scalable on-chip digital Fourier transform spectroscopy. Nature Communications, 4405.

- [23] Shaw, R. A., Kotowich, S., Mantsch, H. H. & Leroux, M., “Quantitation of protein, creatinine, and urea in urine by near-infrared spectroscopy,” Clinical Biochemistry 29, 11-19, doi:[https://doi.org/10.1016/0009-9120\(95\)02011-X](https://doi.org/10.1016/0009-9120(95)02011-X) (1996).
- [24] Chrostowski, L., & Hochberg, M. (2015). Silicon Photonics Design: From Devices to Systems. Cambridge: Cambridge University Press.
- [25] Lin, J. (2005). Optical Waveguide Loss induced by metal cladding. Journal of Vacuum Science & Technology B: Microelectronics and Nanometer Structures Processing, Measurement, and Phenomena, 1361.
- [26] Frey, B. J., Leviton, D. B., & Madison, T. J. (2006). Temperature-dependent refractive index of silicon and germanium. Proceedings of SPIE.
- [27] Harris, Nicholas C.; Ma, Yangjin; Mower, Jacob; Baehr-Jones, Tom; Englund, Dirk; Hochberg, Michael; Galland, Christophe. (2014) Efficient, compact and low loss thermo-optic phase shifter in silicon. Optics Express, 10487.
- [28] Soldano, L. B., & Pennings, E. (1995). Optical multi-mode interference devices based on self-imaging: Principles and applications. Journal of Lightwave Technology, 4.
- [29] Vanguard Automation. (n.d.). Photonic Wire Bonding: Additive 3D nanofabrication for photonic integration.
- [30] M.I. Abd El-Ati. (1997) Electrical conductivity of PbTe thin films. Phys. Solid State 39 (1), 68.
- [31] L. Kungumadevi and R. Sathyamoorthy. (2012). Structural, Electrical, and Optical Properties of PbTe Thin Films Prepared by Simple Flash Evaporation Method. Advances in Condensed Matter Physics, 5.
- [32] Pecunia, V., Zhao, J., Kim, C., Tuttle, B. R., Mei, J., Li, F., Peng, Y., Huq, T. N., Hoye, R. L. Z., Kelly, N. D., Dutton, S. E., Xia, K., MacManus-Driscoll, J. L., & Sirringhaus, H. (2021). Assessing the Impact of Defects on Lead-Free Perovskite-Inspired Photovoltaics via Photoinduced Current Transient Spectroscopy. Advanced Energy Materials, 11(17), 2003968.
- [33] H. Lynden. (1964) Temperature Dependence of the Effective Masses in PbTe. Physical Review, Vol. 135 No. 2A, A514.
- [34] Katiyi, A., & Karabchevsky, A. (2023). Photonic Materials. In Encyclopedia of Materials: Electronics. Elsevier. <https://www.sciencedirect.com/topics/materials-science/lithium-niobate>

[35] S. Deckoff-Jones, Y. Wang, H. Lin, W. Wu, And J. Hu, “Tellurene: A Multifunctional Material for Midinfrared Optoelectronics,” ACS Photonics, Jun. 2019.

[36] D. Kita, et al., “On-Chip Infrared Spectroscopic Sensing: Redefining the Benefits of Scaling,” IEEE J. Sel. Top. Quantum Electron, Vol. 23, 2017.

[37] EO Mod Paper

[38] GVD Paper

[39] Colman, P. “Field renormalization in photonic crystal waveguides”. Phys. Rev. A. 92, 013827 (2015).

[40] Santagiustina, Someda, C. G., Vadalà, G., Combrié, S. & Rossi, A. De. “Theory of slow light enhanced four-wave mixing in photonic crystal waveguides”. Opt. Express 18, 21024–21029 (2010).

[41] S. Serna, and N. Dubreuil, “Bi-directional top-hat D-Scan: single beam accurate characterization of nonlinear waveguides,” Optics Letters, Vol. 42, Aug. 2017.

[42] S. Serna, et al., “Nonlinear Properties of Ge-rich Si<sub>1-x</sub>Gex Materials with Different Ge Concentrations,” Nature Scientific Reports, Vol. 7, Nov. 2017.

[43] S. Serna, et al., “Nonlinear optical properties of integrated GeSbS chalcogenide waveguides,” Photonics Research, Vol. 6, May 2018.

[44] Samuel Felipe Serna Otálvaro. Design and characterization of Silicon Photonic structures for third order nonlinear effects. Optics [physics.optics]. Université Paris Saclay (COmUE), 2016. English.

[45] Saleh, B., and M. Teich. Fundamentals of Photonics. 2nd ed., John Wiley & Sons, Inc., 2007.

---

[46] Magalhães, Regina, et al. “Towards Distributed Measurements of Electric Fields Using Optical Fibers: Proposal and Proof-Of-Concept Experiment.” MDPI, Multidisciplinary Digital Publishing Institute, 10 Aug. 2020.

[47] Melnichuk, M., and Wood, L.T., “Direct Kerr electro-optic effect in noncentrosymmetric materials.” Physical Review 82, 1, 2010.

[48] R. H. Stolen and A. Ashkin, “Optical Kerr effect in glass waveguide”, Appl. Phys. Lett. 22, 294 (1973).

[49] V. Loriot et al., “Measurement of high order Kerr refractive index of major air components”, Opt. Express 17 (16), 13429 (2009).

- [50] C. Brée, A. Demircan and G. Steinmeyer, “Saturation of the all-optical Kerr effect”, Phys. Rev. Lett. 106 (18), 183902 (2011)
- [51] Holshouser, D.F., Von Foerster, H., and Clark, G.L., “Microwave Modulation of Light Using the Kerr Effect.” Journal of the Optical Society of America 51, 12 (1961): 1360-1365.
- [52] R. Amin, M. Zhizhen, M. Tahersima, Rishi Maiti, Mario Miscuglio, Hamed Dalir, and Volker J. Sorger, “A Guide for Material and Design Choices of Electro-Optic Modulators.” Optical Fiber Communication Conference (OFC) 2019.
- [53] Wang, Jianfei; Hu, Juejun; Becla, Piotr; Agarwal, Anuradha M; Kimerling, Lionel C, “Resonant-cavity-enhanced mid-infrared photodetector on a silicon platform,” Optics Express, 18, 12, 12890-12896, 2010
- [54] Singh, Vivek et. al, “Mid-infrared materials and devices on a Si platform for optical sensing,” Science and Technology of Advanced Materials (STAM), 15, 1, 14603, 2014
- [55] Bowers, John. "Trends, Possibilities and Limitations of Silicon Photonic Integrated Circuits and Devices." Proceedings of the IEEE 2013 Custom Integrated Circuits Conference. IEEE, 2013.
- [56] Smit, Meint, Kevin Williams, and Jos Van Der Tol. "Past, present, and future of InP-based photonic integration." APL Photonics 4.5 (2019): 050901.
- [57] Gösele, U., et al. "Fundamental issues in wafer bonding." Journal of Vacuum Science & Technology A: Vacuum, Surfaces, and Films 17.4 (1999): 1145-1152.
- [58] Liang, D., and J. E. Bowers. "Photonic integration: Si or InP substrates?." Electronics Letters 45.12 (2009): 578-581.
- [59] Wang, C. et al. “Integrated lithium niobate electro-optic modulators operating at CMO-compatible voltages.” Nature 562, (2018): 101-104.
- [60] M. Butt, N. Kazanskiy, S. Khonina, G. Voronkov, E. Grakhova, and R. Kutluyarov, Biosensors 13, 568 (2023).
- [61] H. Mukundan, A. Anderson, W. K. Grace, K. Grace, N. Hartman, J. Martinez, and B. Swanson, Sensors 9, 5783 (2009).
- [62] P. Wang and B. Miller, “Waveguide-enhanced Raman spectroscopy (WERS): An emerging chip-based tool for chemical and biological sensing,” Sensors 22, 9058 (2022).
- [63] Y. Chang, V. Paeder, L. Hvozdada, J. Hartmann, and H. Herzog, “Low-loss germanium strip waveguides on silicon for the mid-infrared,” Opt. Lett. 37, 2883 (2012).

- [64] X. Liu, R. Osgood, Y. Vlasov, and W. Green, “Mid-infrared optical parametric amplifier using silicon nanophotonic waveguides,” *Nat. Photon.* 4, 557 (2010).
- [65] S. Zlatanovic, J. Park, S. Moro, J. Boggio, I. Divlansky, N. Alic, S. Mookherjea, and S. Radic, “Mid-infrared wavelength conversion in silicon waveguides using ultracompact telecom-band-derived pump source,” *Nat. Photon.* 4, 561 (2010).
- [66] R. Soref, S. Emelett, and W. Buchwald, “Silicon waveguided components for the long-wave infrared region,” *J. Opt. A, Pure Appl. Opt.* 8, 840 (2006).
- [67] Y. Yue, L. Zhang, H. Huang, R. Beausoleil, and A. Willner, “Silicon-on-nitride waveguide with ultralow dispersion over an octave-spanning midinfrared wavelength range,” *IEEE Photon. J.* 4, 126 (2012).
- [68] U. Griškevičiutė, R. Millar, K. Gallacher, J. Valente, and D. Paul, “Ge-on-Si waveguides for sensing in the molecular fingerprint regime,” *Opt. Exp.* 28, 5794 (2020).
- [69] Y. Chang, V. Paeder, L. Hvozdada, J. Hartmann, and H. Herzig, “Low-loss germanium strip waveguides on silicon for the mid-infrared,” *Opt. Lett.* 37, 2883 (2012).
- [70] M. Nedeljkovic, J. Penades, V. Mittal, G. Murugan, A. Khokhar, C. Littlejohns, L. Carpenter, C. Gawith, J. Wilkinson, and G. Mashanovich, “Germanium-on-silicon waveguides operating at mid-infrared wavelengths up to 8.5  $\mu\text{m}$ ,” *Opt. Exp.* 25, 27431 (2017).
- [71] U. Younis, S. Vanga, A. E.-J. Lim, P. G.-Q. Lo, A. Bettoli, and K. Ang, “Germanium-on-SOI waveguides for mid-infrared wavelengths,” *Opt. Exp.* 24, 11987 (2016).
- [72] K. Gallacher, R. Millar, U. Griskeviciute, L. Baldassarre, M. Sorel, M. Ortolani, and D. Paul, “Low loss Ge-on-Si waveguides operating in the 8–14  $\mu\text{m}$  atmospheric transmission window,” *Opt. Exp.* 26, 25667 (2018).
- [73] M. Nedeljkovic, J. Penad.s, C. Mitchell, A. Khokhar, S. Stankovic, T. D. Bucio, C. Littlejohns, F. Gardes, and G. Mashanovich, “Surface-grating coupled low-loss Ge-on-Si rib waveguides and multimode interferometers,” *IEEE Phot. Tech. Lett.* 27, 1040 (2015).
- [74] J.-M. Fedeli and S. Nicoletti, “Mid-infrared (mid-IR) silicon-based photonics,” *Proceedings of the IEEE* 106, 2302–2312 (2018).
- [75] D. Marris-Morini, V. Vakarin, J. M. Ramirez, Q. Liu, A. Ballabio, J. Frigerio, M. Montesinos, C. Alonso-Ramos, X. L. Roux, S. Serna, D. Benedikovic, D. Chrastina, L. Vivien, and G. Isella, “Germanium-based integrated photonics from near- to mid-infrared applications,” *Nanophotonics* 7, 1781–1793 (2018).

- [76] H. Icenogle, B. Platt, and W. Wolfe, “Refractive indexes and temperature coefficients of germanium and silicon,” *Applied Opt.* 15, 2348 (1967).
- [77] W. Li, P. Anantha, S. Bao, K. Lee, X. Guo, T. Hu, L. Zhang, H. Wang, R. Soref, and C. Tan, “Germanium-on-silicon nitride waveguides for midinfrared integrated photonics,” *App. Phys. Lett.* 109, 241101 (2016).
- [78] V. Reboud, J. Hartman, S. Serna, K. Stoll, C. Monat, and C. Grillet, “Photonic Ge-based platforms for mid-infrared applications,” *Photoniques* 125, 50–57 (2024).
- [79] K. Lee, Transmission and routing of optical signals in on-chip waveguides for silicon microphotonics, PhD dissertation, MIT, Department of Materials Science and Engineering (2001).
- [80] K. Lee, D. Lira, H. Luan, A. Agarwal, J. Foresi, and L. Kimerling, “The experimental and theoretical study of scattering losses in Si/SiO<sub>2</sub> waveguides,” *Int. Phot. Res.* 45 (2000).